2015

Studies of Inelastic Collisions of NaK and NaCs Molecules with Atomic Perturbers

Joshua A. Jones
Lehigh University

Studies of Inelastic Collisions of NaK and NaCs Molecules with Atomic Perturbers

by

Joshua A. Jones

A Dissertation
Presented to the Graduate Committee
of Lehigh University
in Candidacy for the Degree of
Doctor of Philosophy
in
Physics

Lehigh University
January 2015

Approved and recommended for acceptance as a dissertation in partial fulfillment of the requirements for the degree of Doctor of Philosophy.

Joshua A. Jones
Inelastic Collisions of NaK and NaCs Molecules with Atomic Pertubers

---

Date

John Huennekens, Dissertation Director, Chair

Accepted Date

Committee Members

A. Peet Hickman

Gary Deleo

Volkmar Dierolf

Gregory S. Ferguson

Acknowledgements

I owe my biggest thank you to my wife Holly for her patience and support through out graduate school. Her love and support have not gone unnoticed or unappreciated. Who else would have dinner with me in the conference room on late night data runs, proofread my papers and dissertation, listen to me complain about how the lasers were broken (again), or offer words of encouragement and tell me to punch the day in the face? I look forward to the next step in our journey together as it takes us to a short stop in Hamilton, New York at Colgate University as we grow our family with baby Maggie joining us.

Whether he was teaching me the ropes of Jackson's Electricity and Magnetism text or his "quick" chalk board lessons outside the lab he has always been a patient, helpful, and respectful teacher and mentor. Professor Huennekens, despite all the red marks on my dissertation drafts, was always encouraging and has taught me how to become a scientist. The Psi Stars truly miss him on the softball field.

Lehigh has many great professors and Professor Deleo is another shining example. I appreciate his enthusiasm and his encouragement through the years on my research and guidance developing as an educator. Even after Quantum II was over, he was still a fixture in my day to day experience in Lewis Lab.

I would like to thank my committee members Professor Hickman, Professor Dierolf, and Professor Ferguson for their help and encouragement through the research process. I am grateful towards Professor Hickman for his help and input on all things NaK+He theory.

Outside of Lehigh, I wish to thank Drs. Amanda Ross, Patrick Crozet, and Heather Harker at Université Lyon 1 for the wonderful experience of working with them in Lyon, France. More locally, I wish to thank our collaborators at Temple University in Philadelphia, Prof. Marjaata Lyyra and Dr. Ergin Ahmed, who have always been welcoming and providing enlightening discussions.

I wish to thank my family for their support. My parents, Tammy and Bill, I appreciate all they've done for me, even when they didn't understand what I was saying when they asked me to explain my research. It doesn't go unappreciated when Matt calls me up to say that he's proud of me, even when it comes from a younger brother.

To my in-laws, Mark and Sandra, who have been supportive of my endeavors as I've dragged their daughter (and grand-daughter) away from them seemingly wherever I went. They have always been welcoming to me in their family and home and I am grateful to have them in my life.

I also wish to thank my fellow AMO group members. Carl Faust, for when we spent many long days in the lab trying not to lose it. We worked well as a team over the years tackling lab and laser problems. Dave Kashinski for always sharing a laugh and interesting stories. Seth Ashman for providing subtle one line zingers and showing me the ropes of the lab. Chris Wolfe for scholarly discussions on inane internet nonsense, answering select questions from my emails, and teaching me how to tackle the "laser of doom". Kara Richter for foodie discussions and recreating a collision experiment during softball. Ruthie Malenda for being our resident "let me Google that for you" expert and working together on NaK+He collisions. Teri Price for continuing the NaK+He journey after Ruthie graduated.

I am very fortunate to have met some great graduate students while at Lehigh. Many thanks to the my fellow grad students in my incoming year, Ling Cai, Brian Knorr, and Massooma Pirbhai. Ling, thanks for the trips to McGrady's after work for wings and a pint and to Massooma for coming to pick us up when pint became pitcher. Brian, thanks for help with the softball team and for encouraging productivity in the office. Massooma, thanks for planning group lunches and making sure we've all stayed in touch through the years. I also wish to thank those not in my year, Phil Weiser and Laura McMillan for taking the roles of co-coach for the softball team and being the new recipients of the softball emails. Adam Hansell for helping to save Princess Toadstool from the clutches of Bowser on a Sunday

afternoon. Vinnie Zoutenbier for helping to name the “Pretentious Painting Party” and for being so punny. Ben Sofka for engaging in random and interesting conversations, and appreciating all things Celtic. And, thank you to all the other graduate students with whom I have shared the experience of graduate school in the Lehigh Physics Department.

Contents

List of Tables

List of Figures

Abstract

We have investigated collisions of NaK molecules in the first excited state $[2(A)^1\Sigma^+]$, with Ar and He collision partners using laser-induced fluorescence spectroscopy (LIF) and polarization-labeling (PL) spectroscopy in a two-step excitation scheme. Additionally, we have investigated collisions of NaCs molecules in the first excited state $[2(A)^1\Sigma^+]$ with Ar and He perturbers using the LIF technique. We use a pump-probe, two step excitation process. The pump laser prepares the molecule in a particular ro-vibrational $(v,\ J)$ level in the A state. The probe laser frequency is scanned over transitions to the $3^1\Pi$ in NaK or to the $5^3\Pi$ in NaCs. In addition to observing strong direct lines, we also see weak collisional satellite lines that arise from collisions in the intermediate state that take the molecule from the prepared level $(v,\ J)$ to level $(v,\ J + \Delta J)$. The ratios of the intensity of the collisional line to the intensity of the direct line in LIF and PL yield information about population and orientation transfer. Our results show a propensity for ΔJ=even collisions of NaK with Ar and an even stronger propensity for collisions with He. Collisions of NaCs with Ar do not show any such ΔJ=even propensity. Preliminary investigations of collisions of NaCs with He seem to indicate a slight ΔJ=even propensity. In addition, we observe that rotationally inelastic collisions of excited NaK molecules with potassium atoms destroy almost all of the orientation, while collisions with argon destroy about one third to two thirds and collisions with helium destroy only about zero to one third of the initial orientation.

Chapter 1

Introduction

1.1 Overview

Alkali atoms and molecules have proven to be ideal systems for testing some of the most fundamental ideas of quantum mechanics. Alkali atoms are effectively one electron systems to first approximation. Diatomic alkali molecules are, therefore, two electron systems to first approximation, and they serve to test our understanding of molecules. Experimental results serve as benchmarks for theorists who develop models to describe the molecular physics.

In this regard, we build upon earlier experimental studies that have investigated the electronic structure of the diatomic molecules NaK and NaCs. A working knowledge of the electronic structure of these molecules allows us to investigate atom-molecule collisions, which are the subject of this dissertation. In our work, we utilize the optical-optical double resonance experimental technique to study collisions by means of laser-induced fluorescence (LIF) and polarization labeling (PL) spectroscopy. As part of this work, we use these techniques to study collisions of alkali molecules with atomic perturbers.

In this work, I discuss the effects of collisional processes between the molecules

sodium-potassium (NaK) or sodium-cesium (NaCs) and atoms such as helium or argon (inert gas atoms differing in size and polarizability) or alkalis. We use a two-step excitation scheme. We first prepare the diatomic alkali molecule in a specific quantum mechanical energy state using a pump laser, and then we probe the molecule after it has (possibly) undergone an inelastic collision. In this chapter, I first discuss the relevant previous work on electronic states of NaK and NaCs (Sec. 1.2). In Sec. 1.3, I discuss previous studies of molecule-atom collisions that provide important background for the current work. Finally, in Sec. 1.4, I discuss motivation for the current research.

1.2 Optical-Optical Double Resonance

The primary experimental technique used in this work, called optical-optical double resonance (OODR), is a two-step excitation method. A narrow-bandwidth, highly stable laser (the pump laser) is used to prepare the molecule of interest in a particular rotational and vibrational (ro-vibrational[1]) level of a higher electronic state (the intermediate state) by tuning the laser to the transition resonance frequency. A second (probe) laser is used to excite the molecule to another higher electronic state (the upper state) by scanning the frequency of the laser to induce transitions to certain ro-vibrational levels of the upper electronic state (see Sec. 5.3.1). Typically in these experiments, each excitation associated with a transition is monitored by observing the downward fluorescence (laser-induced fluorescence spectroscopy). This method allows the ro-vibrational levels of high lying electronic states to be measured and catalogued. An early use of the OODR method was carried out by Woerdman [1] to study high lying $^1\Sigma_g^+$ electronic states of the Na_2 molecule using two-step Doppler-free excitations.

Due to the dipole selection rule that the spin character cannot change during an electronic transition and the fact that the ground states of all alkali molecules

[1]Rotational combined with vibrational is contracted to ro-vibrational in the jargon of the field.

are spin singlet, it is not generally possible to excite higher triplet states with this method. However, Li and Field [2] developed a modified form of OODR, called perturbation facilitated optical-optical double resonance (PFOODR) which took advantage of localized coupling between specific singlet and triplet levels of the $1(A)^1\Sigma_u^+$ and $1(b)^3\Pi_u$ states of the Na_2 molecule. In the PFOODR method the molecule is first excited from the singlet ground state to a particular level of the intermediate state which has mixed singlet-triplet spin character. The molecule is then further excited to a higher triplet state. In this way, the PFOODR technique allows access to high-lying triplet electronic states of the diatomic alkali molecules from the singlet ground state.

The OODR technique has been applied to both homonuclear and heteronuclear diatomic alkali molecules. Specifically for NaK, our group has used the OODR technique to map out the $3^1\Pi$ [3], $3^3\Pi$ [4], $1^3\Delta$ [5, 6], $4^3\Pi$ [7], and $4^3\Sigma^+$ [8] electronic states. We have also started mapping higher electronic states of the NaCs molecule. NaCs is noteworthy due to its large permanent electric dipole moment and due to the fact that the spin-orbit interactions are very large, making it an interesting contrast to NaK for collision experiments. Ashman *et al.* [9] in our lab mapped out the high lying $5^3\Pi_0$ electronic state. This state is used as the upper state for the collisional studies in the current work using the PFOODR method.

The methods of OODR and PFOODR are important for our collisional studies because we use these spectroscopic techniques to selectively prepare and probe the NaK or NaCs molecule, respectively, to study the collisional processes. We also make use of previous work to map the ground and intermediate electronic states. Of particular interest for the current work are data that have been gathered on many rotational and vibrational levels of the electronic ground state $[1(X)^1\Sigma^+]$ and first excited singlet $[2(A)^1\Sigma^+]$ state of NaK by Russier-Antoine *et al.* [10] and Ross *et al.* [11] using Fourier transform spectroscopy. These authors used their data to produce accurate potential energy curves and determine spectroscopic constants, which can, in turn, be used to predict rotational and vibrational level energies of these electronic states. For NaCs, we are again interested in the ro-vibrational level energies

of the ground state and the $2(A)^1\Sigma^+$state. The levels of the ground electronic state ($X^1\Sigma^+$) of NaCs were mapped out by Docenko *et al.* [12] using Fourier transform spectroscopy. Zaharova *et al.* [13] mapped the $2(A)^1\Sigma^+$state of NaCs and, due to the large coupling between levels of the $2(A)^1\Sigma^+$and $b^3\Pi_\Omega$ states, carried out a depertubation analysis of the levels of these electronic states.

We use the OODR technique to determine collisional population transfer and the associated rate coefficients by observing fluorescence using LIF spectroscopy. However, we also observe collisions using PL spectroscopy to determine information about collisional orientation transfer (both are discussed in more detail in Chapter 3). Utilizing the OODR technique with polarization spectroscopy is yet another way to study upper electronic states of diatomic alkali molecules. In NaK, this technique has been used to study various electronic states [14, 15, 16, 17, 18]. In these studies of high-lying electronic states, it is advantageous to utilize the collisional lines for mapping the ro-vibrational levels of the states. This approach allows one to assign far more transitions than can be done using direct pump and probe OODR lines alone.

1.3 Collisional Studies

Studies of ro-vibrationally inelastic collision studies have been carried out by many research groups in the molecular physics community. In these collision studies, propensities for certain types of transitions have sometimes been observed. For example, Ottinger *et al.* [19] studied collisions of the Li_2 $1(B)^1\Pi_u$ with argon atoms and observed a propensity for either $\Delta J > 0$ or $\Delta J < 0$ depending on the initial Λ doubling component excited. Pritchard and coworkers [20, 21, 22] observed a propensity for collisions that obeyed $\Delta J = -4\Delta v$ in studies of ro-vibrationally inelastic collisions of Li_2 $[1(A)^1\Sigma_u^+]$ with xenon, argon, and neon. This propensity was attributed to an approximate energy resonance (i.e., the vibrational energy gap was approximately equal to the gap between rotational levels separated by four units).

In addition to observing general propensities associated with certain types of collisions, we can also determine collisional rate coefficients for specific channels. In most cases, these rate coefficients have been determined by observing the fluorescence from molecules in the directly populated level and comparing that to the fluorescence from the adjacent collisionally populated rotational or vibrational levels. Bergmann and Demtröder [23] examined ro-vibrational collision cross-sections of excited Na_2 molecules in the $1(B)^1\Pi_u$ state with helium as the collisional partner. In the collisional studies of Pritchard and coworkers [20, 21, 22], rate coefficients for the rotationally and vibrationally inelastic collisions of Li_2 with various atomic perturbers were determined. These studies were expanded by Gao and Stewart [24] and Gao *et al.* [25] to determine vibrationally inelastic collision rate coefficients in the $1(A)^1\Sigma_u^+$ state of Li_2 with neon atom perturbers.

Polarization spectroscopy provides further insight into inelastic collisions. Early observations of inelastic collisions using polarization spectroscopy were made by Teets *et al.* [26]. Much of the motivation for our current work stems from the study performed by Salami *et al.* [27] investigating the Rb_2 molecule. This study highlighted the fact that rotationally inelastic collisions can preserve some fraction of the angular momentum orientation (see Sec. 5.4). Salami *et al.* [27] observed collisions resulting in changes of the rotational quantum number by $|\Delta J| \leq 58$ using the polarization labeling technique in a V-type pump-probe scheme as shown in Fig. 1.1.

Both experimentalists and theorists have worked to understand collisions involving diatomic molecules. The experimental results serve as a benchmark for the theoretical calculations, and likewise, the calculations serve as a guide for experimentalists. McCaffery [28] gave a kinematic interpretation to the Li_2 $1(A)^1\Sigma_u^+$ vibrationally inelastic collisions. The *ab initio* calculations performed by Alexander and Werner [29] for J-changing collisions of Li_2 $1(A)^1\Sigma_u^+$ molecules with neon perturbers agree well with the experimental results of Scott *et al.* [20].

In recent work carried out at Lehigh University, Wolfe *et al.* [30] observed a

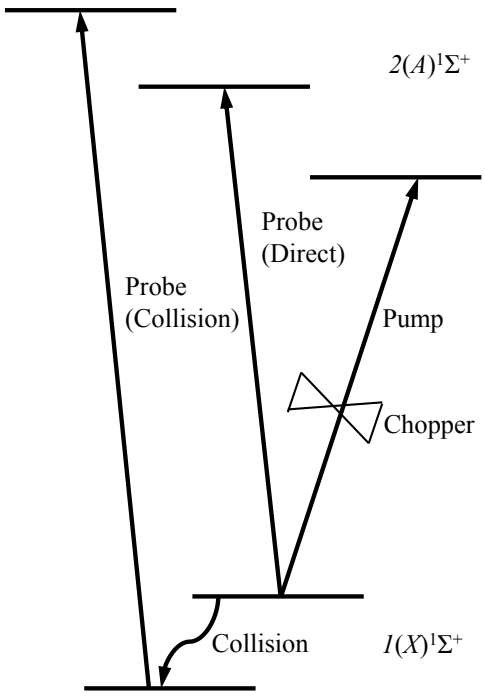

Figure 1.1: A schematic diagram of a V-type excitation scheme used in polarization spectroscopy. The lower ro-vibrational level is "tagged" by the mechanical chopper placed in the beam path of the pump beam. The chopped pump laser beam modulates the population in the lower level and a lock-in amplifier filters out any signal not at the chopper frequency. In this example, collisions occur in the lower state where either v or J may change. The fraction of the population in a collisional level created by collisional transfer is also modulated, and hence, can be detected using the lock-in amplifier.

propensity for ΔJ = even collisions of NaK $2(A)^1\Sigma^+$molecules with argon atoms. Wolfe and coworkers also determined collision rate coefficients for rotationally inelastic collisions of NaK in the $2(A)^1\Sigma^+$state with argon and potassium for $\Delta J = \pm 1, \pm 2, \pm 3, \pm 4$. The experiments of Wolfe *et al.* used the techniques of laser-induced

fluorescence spectroscopy and polarization labeling spectroscopy to make quantitative measurements of the transfer of population and orientation during inelastic collisions of NaK molecules with alkali atom and argon atom pertubers.

1.4 Overview of Research

These previous works have provided us with the framework for investigating rotationally and vibrationally inelastic collisions using the OODR technique and incorporating Fourier transform spectroscopic data. We do this with two contrasting heteronuclear alkali diatomic molecules, NaK and NaCs, both prepared in an excited state. The combination of fluorescence and polarization spectroscopy are used together to determine population and orientation transfer during inelastic collisions.

In this work, I studied the inelastic collisions of NaK and NaCs molecules with atomic perturbers. Our first goal was to explore, compare and contrast the effects of different inert gas perturbers in collisions with NaK molecules. To do this, we used the same initial ro-vibrational level of NaK $[2(A)^1\Sigma^+(v = 16, J = 30)]$ as used by Wolfe *et al.* We incorporated the data of Wolfe *et al.* with our new data to compare the effects of argon versus helium. A major motivation for this comparative study was the fact that Malenda and Hickman [31] had begun theoretical investigations of rotationally inelastic NaK-He collisions. Due to limitations on computer resources, they chose to study collisions with He perturbers because the electronic structure of He is much simpler than that of Ar.

In addition, the calculations were carried out for lower rotational levels, $J \leq 20$ and for $v = 0$ of the NaK $2(A)^1\Sigma^+$state, whereas the Wolfe *et al.* experimental studies were carried out for $v = 16, J = 30$. As a result of their calculations, Malenda and Hickman found a significant dependence of the rate coefficients on initial J level. These calculations encouraged us to look at the effects of experimentally varying the initial rotational level of the $2(A)^1\Sigma^+$state as well as the initial vibrational level, so that our current results can be directly compared to the most recent

theoretical work. In addition, we have collaborated with Drs. Amanda Ross and Patrick Crozet of Université Lyon 1 to use a different experimental setup (FTS see Sec. 4.5.3) as a test of our previous measurement techniques and to address additional initial rotational and vibrational levels. Specifically, this work provides much of our data on NaK $2(A)^1\Sigma^+(v = 0)$ collisions as well as new data on v-changing collisions.

Finally, we have also studied collisions involving the NaCs molecule. We have collected fluorescence data using both argon and helium as the perturber to study population transfer. NaCs is much heavier than NaK and the two atoms making up the NaCs molecule are more dissimilar. Therefore, we carried out these NaCs studies to explore whether the $\Delta J =$ even propensity would still be observed in this molecule.

Chapter 2

Background: Molecular Physics

2.1 Overview

In this chapter, I provide a brief summary of the quantum mechanical treatment of a diatomic molecule, beginning with the non-relativistic, time-independent Schrödinger equation. The discussion will lead to general expressions for the electronic, vibrational, and rotational energies and an understanding of angular momentum coupling in a diatomic molecule. In Sec. 2.2, I first discuss the separation of the full molecular Schrödinger equation into electronic and nuclear parts. I then introduce the Born-Oppenheimer approximation that provides an important simplification, allowing a straight forward solution for the motion of the electrons and nuclei within a diatomic molecule. In Sec. 2.3, I discuss different aspects of the nuclear motion including vibration and rotation (Sec. 2.3.1). Terms beyond the first-order approximations are laid out in Sec. 2.3.2, and the Dunham expansion is presented.

Section 2.4 provides a discussion of how the various angular momentum vectors associated with electron and nuclear motion can couple in the diatomic molecule. The different coupling schemes important for this work are described by three Hund's cases: (a) is presented in Sec. 2.4.1, (b) in Sec. 2.4.2, and (c) in Sec. 2.4.3. The chapter will conclude with a discussion on electronic transitions and selection rules

in Sec. 2.5.

2.2 The Born-Oppenheimer Approximation

Even though diatomic molecules are the simplest type of molecule, their quantum mechanical description is much more complicated than that of atoms. Specifically, there are two nuclei located in different places, which breaks the spherical symmetry, and there are many more interactions that need to be taken into account. Following Bransden and Joachain [32], we begin by considering the time-independent Schrödinger equation for the entire molecule. Within the Hamiltonian, we incorporate the various terms due to the electron kinetic energy, nuclear kinetic energy, and the Coulomb interaction potential energy terms of the system,

$$\hat{H}\Psi = E\Psi, \tag{2.1}$$

which can be expanded to read

$$\left[\hat{T}_{el} + \hat{T}_{nuc} + V\right] \Psi(\mathbf{R}; \mathbf{r_1}, \mathbf{r_2}, ...\mathbf{r}_i) = E\Psi(\mathbf{R}; \mathbf{r_1}, \mathbf{r_2}, ...\mathbf{r}_i). \tag{2.2}$$

The wavefunction, Ψ, is written as a function of the positions of the nuclei and the electrons with respect to the center of mass. As shown in Fig. 2.1, $\mathbf{R_A}$ and $\mathbf{R_B}$ describe the locations of nuclei A and B with respect to the center-of-mass and we can define an internuclear separation vector $\mathbf{R} = \mathbf{R_B} - \mathbf{R_A}$. The positions of the electrons are also given in reference to the center of mass, $\mathbf{r_1}, \mathbf{r_2}, ...\mathbf{r}_i$.

After transforming to the center of mass frame of reference, the nuclear kinetic energy term of the Hamiltonian is

$$\hat{T}_{nuc} = -\frac{\hbar}{2\mu}\nabla_R^2 \,. \tag{2.3}$$

This term describes the motion of the two nuclei about the center of mass and μ is the reduced mass of the nuclei $\left(\frac{M_1 M_2}{M_1 + M_2}\right)$. The total kinetic energy of the electrons, each of mass m_e, in the system must also be included in the Hamiltonian,

$$\hat{T}_{el} = \sum_{i=1}^{N} \left(-\frac{\hbar}{2m_e}\nabla_{r_i}^2\right) \,. \tag{2.4}$$

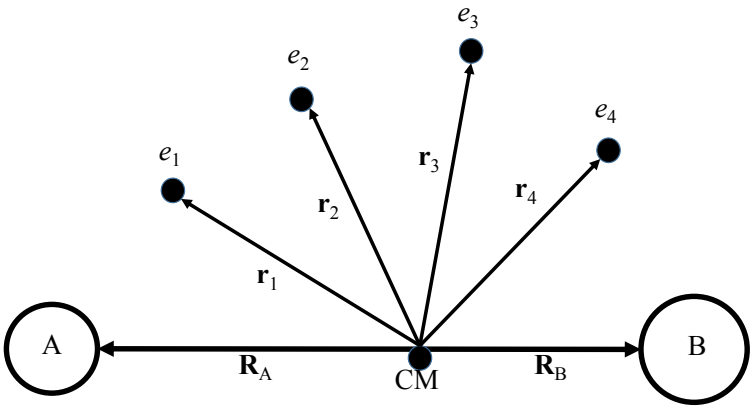

Figure 2.1: The coordinate system for a diatomic molecule.

Because the electrons and nuclei are charged particles, the potential energy, V, includes numerous Coulomb interactions. There is the Coulomb repulsion between the two positively charged nuclei,

$$V_{nuc-nuc} = \frac{Z_A Z_B e^2}{4\pi\epsilon_0 R}, \tag{2.5}$$

where Z_A and Z_B are the atomic numbers of the two atoms and e is the fundamental electric charge. Likewise, the Coulomb electron-electron repulsion terms are given by

$$V_{el-el} = \sum_{i,j=1;i>j}^{N} \frac{e^2}{4\pi\epsilon_0 |\mathbf{r}_i - \mathbf{r}_j|}\,. \tag{2.6}$$

The restriction $i > j$ in the summation assures that we don't double count any of the electron-electron interactions. Lastly, there is the attractive Coulomb interaction between each electron and each nucleus,

$$V_{nuc-el} = -\sum_{i=1}^{N} \frac{Z_A e^2}{4\pi\epsilon_0 |\mathbf{r}_i - \mathbf{R}_\mathrm{A}|} - \sum_{i=1}^{N} \frac{Z_B e^2}{4\pi\epsilon_0 |\mathbf{r}_i - \mathbf{R}_\mathrm{B}|}\,. \tag{2.7}$$

Solving the time-independent Schrödinger equation with all of these kinetic and potential energy terms is generally quite complicated. However, due to the fact that the mass of an electron is small compared to that of a nucleus, the electrons move much faster than the nuclei. Hence, the electrons tend to rapidly readjust to any change of nuclear positions. This fact can be exploited by solving the electronic part of the Schrödinger equation with the nuclear positions fixed in place at a certain internuclear separation, R:

$$\left[\hat{T}_{el} + V(\mathbf{R}; \mathbf{r_1}, \mathbf{r_2}, ...\mathbf{r}_i)\right] \Phi_q(\mathbf{R}; \mathbf{r_1}, \mathbf{r_2}, ...\mathbf{r}_i) = E_q(R)\Phi_q(\mathbf{R}; \mathbf{r_1}, \mathbf{r_2}, ...\mathbf{r}_i)\,. \tag{2.8}$$

In general, quantum chemistry computer codes are used to solve this equation for a large number of fixed internuclear separations. The various energy eigenvalues $E_q(R)$ represent the possible electronic states of the molecule. When plotted as a function of R, these electronic eigenvalues are called "electronic potential curves" for reasons that will become clear below. A plot of theoretical potential curves compiled from Ref. [33] is shown in Fig. 2.2 for the molecule NaK. Similar calculations have also been carried out for the NaCs molecule [34]. Both of these sets of calculations are important for the present work.

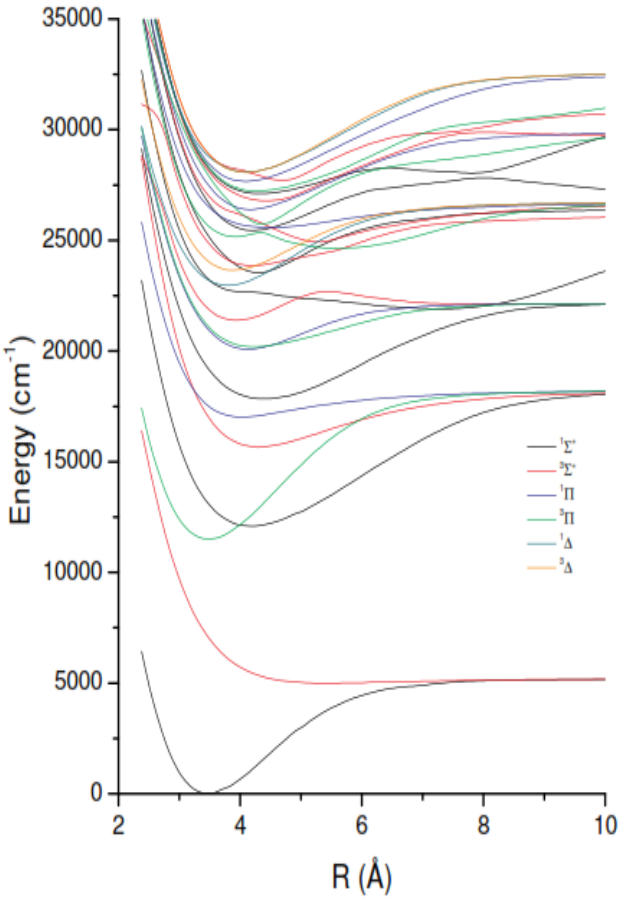

Figure 2.2: A set of NaK theoretical electronic potential curves from Magnier *et al.* [33]. The curves are colored by the spin multiplicity ($2S+1$) and Λ components describing the electronic state (see Sec. 2.4.1 for a discussion of electronic state labeling).

The total wavefunction of the molecule can be written as an expansion in terms of electronic wavefunctions, which form a complete set of functions over the electronic coordinates:

$$\Psi(\mathbf{R};\mathbf{r_1},\mathbf{r_2},...\mathbf{r}_i) = \sum_q \mathscr{F}_q(\mathbf{R})\Phi_q(\mathbf{R};\mathbf{r_1},\mathbf{r_2},...\mathbf{r}_i). \tag{2.9}$$

The $\Phi_q(\mathbf{R};\mathbf{r_1},\mathbf{r_2},...\mathbf{r}_i)$ functions are orthonormal and, therefore, obey the relation

$$\int d^3\mathbf{r}_1 d^3\mathbf{r}_2 ... d^3\mathbf{r}_i \Phi_s^\star(\mathbf{R};\mathbf{r_1},\mathbf{r_2},...\mathbf{r}_i)\Phi_q(\mathbf{R};\mathbf{r_1},\mathbf{r_2},...\mathbf{r}_i) = \delta_{qs}\,. \tag{2.10}$$

Using the expansion (2.9) in Eq. (2.2) gives

$$\left[\hat{T}_{el} + \hat{T}_{nuc} + V - E\right] \sum_q \mathscr{F}_q(\mathbf{R})\Phi_q(\mathbf{R};\mathbf{r_1},\mathbf{r_2},...\mathbf{r}_i) = 0\,. \tag{2.11}$$

We can then use

$$\left[\hat{T}_{el} + V\right] \sum_q \mathscr{F}_q(\mathbf{R})\Phi_q(\mathbf{R};\mathbf{r_1},\mathbf{r_2},...\mathbf{r}_i) = \sum_q E_q \mathscr{F}_q(\mathbf{R})\Phi_q(\mathbf{R};\mathbf{r_1},\mathbf{r_2},...\mathbf{r}_i)\,, \tag{2.12}$$

multiply Eq. (2.11), on the left by $\Phi_s^*(\mathbf{R};\mathbf{r_1},\mathbf{r_2},...\mathbf{r}_i)$ and integrate over electron coordinates to yield

$$\begin{aligned} &\int \Phi_s^*(\mathbf{R};\mathbf{r_1},\mathbf{r_2},...\mathbf{r}_i)\hat{T}_{nuc} \sum_q \mathscr{F}_q(\mathbf{R})\Phi_q(\mathbf{R};\mathbf{r_1},\mathbf{r_2},...\mathbf{r}_i) d^3\mathbf{r}_1 d^3\mathbf{r}_2 ... d^3\mathbf{r}_i \\ &= \left[E - E_s(R)\right]\mathscr{F}_s(\mathbf{R})\,. \end{aligned} \tag{2.13}$$

However, because both $\mathscr{F}_q(\mathbf{R})$ and the electronic wavefunctions depend on $\mathbf{R}$, the nuclear kinetic energy term is fairly complicated. If we use the identity

$$\nabla^2(fg) = f\nabla^2 g + 2\nabla f\cdot\nabla g + g\nabla^2 f\,, \tag{2.14}$$

we find

$$\begin{aligned} \hat{T}_{nuc}\sum_q \mathscr{F}_q\Phi_q &= -\frac{\hbar}{2\mu}\nabla_R^2\left(\sum_q \mathscr{F}_q\Phi_q\right) \\ &= -\frac{\hbar^2}{2\mu}\sum_q\left[\mathscr{F}_q\nabla_R^2\Phi_q + 2\nabla_R\mathscr{F}_q\cdot\nabla_R\Phi_q + \Phi_q\nabla_R^2\mathscr{F}_q\right]\,. \end{aligned} \tag{2.15}$$

At this point, in order to proceed, it is customary to invoke the Born-Oppenheimer approximation, which assumes that the electronic wavefunction only depends weakly on the internuclear separation. This is due to the fact that electrons are small and fast compared to the size and speed of the nuclei. With the Born-Oppenheimer approximation we assume,

$$|\nabla_R \mathscr{F}_q| >> |\nabla_R \Phi_q| \,. \tag{2.16}$$

This approach allows us to neglect the first two terms on the right hand side of Eq. (2.15). In the case where the effects of these neglected terms must be considered, they are usually addressed using perturbation theory.

With the Born-Oppenheimer approximation, the term on the left hand side of Eq. (2.13) becomes

$$\sum_q \int d^3\mathbf{r}_1 d^3\mathbf{r}_2 ... d^3\mathbf{r}_i \Phi_s^\star \left[-\frac{\hbar^2}{2\mu} \nabla_R^2 \mathscr{F}_q \right] \Phi_q = -\frac{\hbar^2}{2\mu} \nabla_R^2 \mathscr{F}_s \,, \tag{2.17}$$

and the Schrödinger equation reduces to

$$-\frac{\hbar^2}{2\mu} \nabla_R^2 \mathscr{F}_s(\mathbf{R}) + [E_s(R) - E]\, \mathscr{F}_s(\mathbf{R}) = 0 \,. \tag{2.18}$$

In the next section (Sec. 2.3), I will describe a further separation of $\mathscr{F}_q(\mathbf{R})$ into angular and radial terms. After doing so, we will see that $E_s(R)$ plays the role of a potential energy term in a one-dimensional nuclear Schrödinger equation.

2.3 Motion of the Nuclei

2.3.1 Vibration and Rotation

The diatomic molecule not only has various electronic states, but there are additional degrees of freedom in the motion of the molecule; it can vibrate and rotate.

For each stable bound electronic potential energy state, there are many possible vibrational and rotational levels that a molecule can populate.

As mentioned in the previous section (Sec. 2.2), we can use the method of separation of variables to write the total nuclear wavefunction as a product of a radial (vibrational) wavefunction and an angular (rotational) wavefunction,

$$\mathscr{F}_q(R) = \frac{1}{R}\chi_v(R)\psi_r(\theta,\phi)\,. \tag{2.19}$$

The subscripts v and r denote the vibration and rotation wavefunctions, respectively. We can expand the nuclear kinetic energy operator of Eq. (2.18) using spherical coordinates as follows,

$$\begin{aligned}\nabla_R^2\left[\frac{\chi_v(R)}{R}\psi_r(\theta,\phi)\right] &= \frac{\psi_r(\theta,\phi)}{R}\frac{d^2\chi_v(R)}{dR^2} \\ &+ \frac{\chi_v(R)}{R^3}\left[\frac{1}{\sin\theta}\frac{\partial}{\partial\theta}\left(\sin\theta\frac{\partial\psi_r(\theta,\phi)}{\partial\theta}\right) + \frac{1}{\sin^2\theta}\frac{\partial^2\psi_r(\theta,\phi)}{\partial\phi^2}\right]\,.\end{aligned} \tag{2.20}$$

We consider the diatomic molecule to be a rigid rotor, i.e., that the two nuclei have a fixed separation and rotate about the center of mass, such that $\psi_r = \psi(\theta,\phi)$ only. Because of the rigid rotor approximation, the angular function, ψ_r, obeys the eigenvalue equation,

$$\left[\frac{1}{\sin\theta}\frac{\partial}{\partial\theta}\left(\sin\theta\frac{\partial}{\partial\theta}\right) + \frac{1}{\sin^2\theta}\frac{\partial^2}{\partial\phi^2}\right]\psi_r(\theta,\phi) = -J(J+1)\psi_r(\theta,\phi)\,. \tag{2.21}$$

For a quantum mechanical rigid rotor, the Schrödinger equation can be solved exactly for the rotational level energies, E_r. The eigenfunction solutions are spherical harmonics and the rotational energies are given by

$$E_r = \frac{\hbar^2}{2I}J(J+1) \;= B_e J(J+1)\,, \tag{2.22}$$

where $I = \mu R^2$ is the moment of inertia of the rigid rotor, B_e is the rotational constant, and J is the rotational quantum number ($J = 0, 1, 2...$).

Substituting Eqs. (2.20) and (2.21) into Eq. (2.18), we find that $\chi_v(R)$ obeys the one-dimensional equation,

$$-\frac{\hbar^2}{2\mu}\frac{d^2\chi_v(R)}{dR^2} + \left[E_s(R) + \frac{\hbar^2 J(J+1)}{2\mu R^2} - E\right]\chi_v(R) = 0\,. \tag{2.23}$$

This result has the form of a one-dimensional Schrödinger equation, with an effective potential, $E_s(R) + \frac{\hbar^2 J(J+1)}{2\mu R^2}$. The first term, $E_s(R)$, is the "rotationless potential" and J is the rotational angular momentum quantum number. Use of the Born-Oppenheimer approximation effectively uncouples the nuclear and electronic motion. Once the electronic wavefunctions have been calculated for numerous points along the internuclear separation by solving the electronic Schrödinger Eq. (2.8), the nuclear motion can be determined by numerical solution of the nuclear Schrödinger equation with the electronic energies acting as the potential energy function.

Near its minimum, a bound electronic potential energy curve can be expanded in a Taylor series about the equilibrium separation R_0:

$$V(R) = V(R_0) + (R - R_0)\frac{dV(R)}{dR}\bigg|_{R=R_0} + \frac{1}{2}(R - R_0)^2\frac{d^2V(R)}{dR^2}\bigg|_{R=R_0} + \ldots\,. \tag{2.24}$$

The first derivative term is zero because it is evaluated at the minimum of the potential well, and $V(R_0)$ is just a constant energy offset. Ignoring terms beyond the second derivative,

$$V(R) \approx V(R_0) + \frac{1}{2}k(R - R_0)^2 \tag{2.25}$$

where $k = \frac{d^2V(R)}{dR^2}\big|_{R=R_0}$ is the value of the effective spring constant of the molecule. Equation (2.25) is the potential energy of a harmonic oscillator, and therefore, to lowest order, the vibrational energy levels are given by,

$$E_v = V(R_0) + \hbar\omega\left(v + \frac{1}{2}\right)\,, \tag{2.26}$$

where each vibrational level energy is characterized by a quantum number, $v = 0, 1, 2...$, and the frequency of oscillation is $\omega = \sqrt{\frac{k}{\mu}}$.

2.3.2 Higher-Order Effects of Vibration and Rotation

The rigid rotor and harmonic oscillator are good first approximations, but they doesn't fully describe the true motion of the nuclei. An improvement on the rigid rotor approximation is to assume that the nuclei are connected by a massless spring. This approach allows the molecule to "stretch" as it gains rotational energy. For higher energies above the minimum, the potential looks more and more anharmonic. Additional terms beyond the quadratic term in the Taylor expansion, Eq. (2.24), are needed to accurately predict level energies. The Morse potential (shown in Fig. 2.3) is a better approximation to a real potential than the harmonic oscillator potential and is given by [35],

$$V(R) = D\left[1 - e^{-a(R-R_0)}\right]^2 . \tag{2.27}$$

The value of D represents the well depth, $D = E_s(\infty) - E_s(R_0)$. The value of a is dependent on the molecule. The Morse potential provides us with a start to describing the anharmonicity of an electronic state potential. A comparison of the Morse potential and the harmonic oscillator is shown in Fig. 2.3. Vibrational energies of the Morse potential are given by

$$G_v = \omega_e(v + \frac{1}{2}) - \omega_e x_e(v + \frac{1}{2})^2 \tag{2.28}$$

where $\omega_e x_e$ is the anharmonicity constant. The constants a and D in Eq. (2.27) are related to ω_e and $\omega_e x_e$ by

$$D = \frac{\omega_e^2}{4\omega_e x_e} \tag{2.29}$$

and

$$a = \sqrt{\frac{2\pi^2 c\mu}{hD}}\omega_e \, . \tag{2.30}$$

Most bound states can be fairly well approximated by a Morse potential, however additional terms may be needed to reproduce level energies to spectroscopic accuracy. Therefore, vibrational level energies of the true anharmonic potential can more accurately be described by an expansion that includes higher order terms [35],

$$G_v = \omega_e(v + \frac{1}{2}) - \omega_e x_e(v + \frac{1}{2})^2 + \omega_e y_e(v + \frac{1}{2})^3 + \ldots , \tag{2.31}$$

where $\omega_e x_e$ and $\omega_e y_e$ are anharmonicity constants such that

$$\omega_e >> \omega_e x_e >> \omega_e y_e \, . \tag{2.32}$$

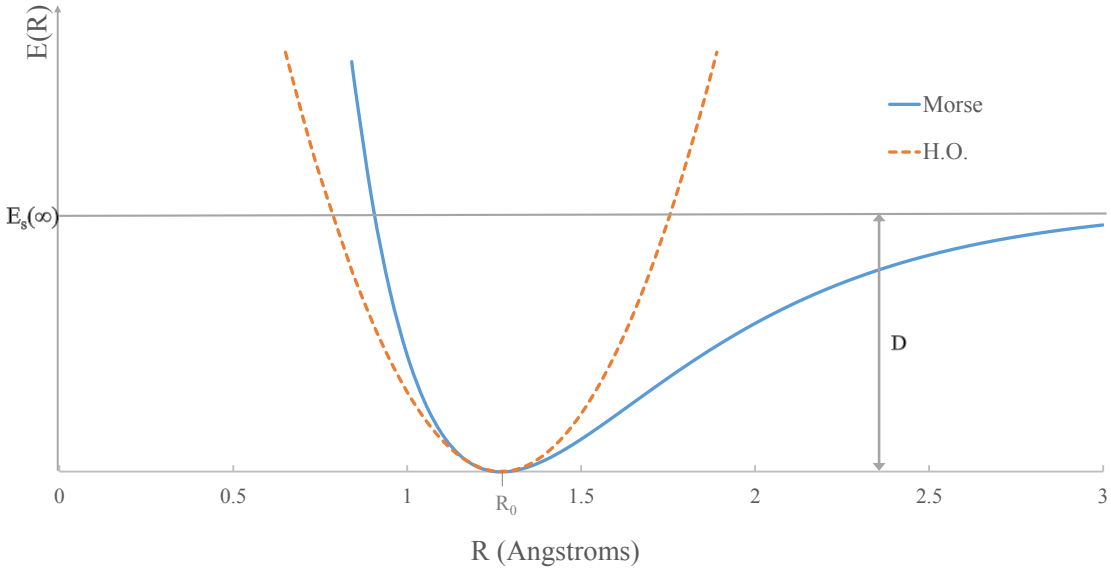

Figure 2.3: A comparison of models of a molecular potential; the first approximation of a quantum mechanical harmonic oscillator versus a Morse potential. The harmonic oscillator is only a good representation near the bottom of the well.

In addition, as the molecule rotates faster, it stretches due to the centrifugal force. Thus a correction term must be added to the rotational energy of the molecule,

$$E_r = B_e J(J+1) - D_e \left[J(J+1)\right]^2 \, . \tag{2.33}$$

This new term represents centrifugal distortion, and D_e is called the centrifugal distortion constant. The inclusion of this term causes a decrease in the spacing of the

rotational level energies of the molecule as J increases.

Up to this point, rotational and vibrational motion has been dealt with separately. A more realistic model is the vibrating rotor where the rotational and vibrational motions are coupled. As the molecule rotates, the internuclear separation changes due to the molecular vibration. This causes the moment of inertia to change, affecting the B_e value of the molecule. The rotational constant is now dependent on the vibrational state:

$$B_v = B_e - \alpha\left(v+\frac{1}{2}\right) + \gamma_{e1}\left(v+\frac{1}{2}\right)^2 + \gamma_{e2}\left(v+\frac{1}{2}\right)^3 + \dots . \tag{2.34}$$

The leading correction term is usually taken to be negative because the mean internuclear separation $\langle R_v \rangle$ tends to increase with v. In a similar way, the vibrational motion also affects the centrifugal distortion, resulting in a vibration dependent centrifugal distortion constant, D_v:

$$D_v = D_e + \beta_{e1}\left(v+\frac{1}{2}\right) + \beta_{e2}\left(v+\frac{1}{2}\right)^2 + \beta_{e3}\left(v+\frac{1}{2}\right)^3 + \dots . \tag{2.35}$$

The values of the parameters in Eqs. (2.34) and (2.35) are determined spectroscopically, and more terms can be included to reproduce level energies to within spectroscopic accuracy.

The total energy of a ro-vibrational level in an electronic state can now be found as a sum of electronic, vibrational, and rotational energies:

$$E(v, J) = E_{el} + E_v + E_r \, . \tag{2.36}$$

Here, the terms are written from left to right in order of the largest to smallest energy contribution. Equation (2.36) can be rewritten using Eqs. (2.31), (2.34), and (2.35) as

$$E(v, J) = T_e + G_v + B_v J(J+1) - D_v \left[J(J+1)\right]^2 \, , \tag{2.37}$$

where $T_e = E_{el}$ is the value of the minimum of the electronic potential energy. Equation (2.37) can be succinctly written in a form of a double series expansion

developed by Dunham [36]:

$$E(v,J) = \sum_{k,l} Y_{k,l}(v+\frac{1}{2})^k \left[J(J+1) - \Omega^2\right]^l \ . \tag{2.38}$$

The term involving Ω^2 is explained in Sec. 2.4 and accounts for the electronic

$(Y_{k,l})$ k/l	0	1	2
0	T_e	B_e	$-D_e$
1	ω_e	$-\alpha_e$	$-\beta_{e1}$
2	$-\omega_e x_e$	γ_{e1}	$-\beta_{e2}$
3	$\omega_e y_e$	γ_{e2}	$-\beta_{e3}$

Table 2.1: The spectroscopic constants that pertain to the Dunham coefficients $Y_{k,l}$ [36]. These correspondences are approximate and their accuracy depends on the value of the quantum number Ω.

contribution to the total angular momentum. This issue will be addressed as part of a discussion of the Hund's coupling cases. Each value of k and l in the Dunham expansion corresponds to a term from Eq. (2.37) and the relationships between the Dunham and spectroscopic coefficients are given in Table 2.1. As stated previously, the anharmonic (Morse) potential does not always accurately reproduce ro-vibrational level energies and it is often the case that many terms (~ 50) are used in the Dunham expansion fit in order to reproduce the ro-vibrational level energies to spectroscopic accuracy. However, when so many terms are retained in the Dunham expansion, the physical interpretation of individual terms becomes lost.

2.4 Hund's Cases

Hund's coupling cases were derived as the result of investigations of how the various angular momentum vectors can couple within the molecule [35]. Excluding nuclear spin, the total angular momentum of the system is denoted by the vector

J, the corresponding quantum number is J. The total angular momentum has contributions from the motion of the electrons and the nuclei. Electron orbital angular momentum and spin angular momentum are described by **L** and **S**, respectively. Nuclei exhibit rotational angular momentum, **N**. Each angular momentum vector couples with every other angular momentum vector due to magnetic interactions. These different coupling schemes arise depending on the relative strengths of the various interactions. The most common Hund's cases, (a), (b), and (c), will be discussed here. Other cases, (d) and (e), also exist. This discussion will follow that of Refs. [32], [35], and [37] which provide additional information about the Hund's cases.

2.4.1 Hund's Case (a)

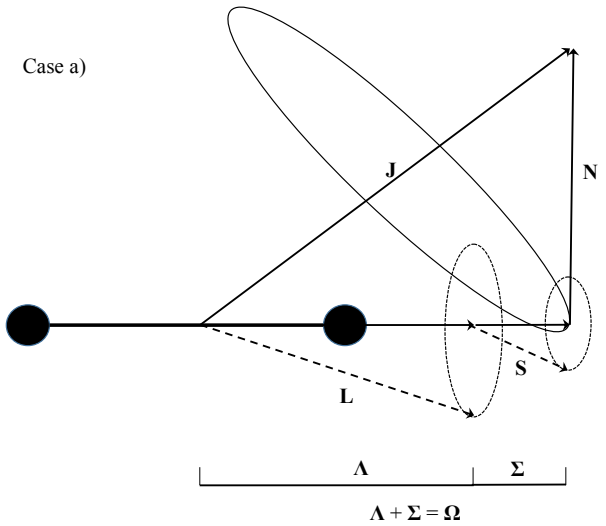

Figure 2.4: Vector diagram for Hund's case (a) using the notation in [35]. Each ellipse demonstrates the precession of the corresponding vector.

In Hund's case (a), the main feature is that the electron orbital angular momentum and the electron spin both couple strongly to the internuclear axis and relatively weakly to the nuclear angular momentum. This case typically applies to molecules in levels characterized by small internuclear separations and low rotational quantum numbers. A vector diagram, shown in Fig. 2.4, illustrates the coupling of the angular momenta in case (a). The total electron orbital angular momentum, $\mathbf{L}$, precesses rapidly about the internuclear axis, so only its component along the internuclear axis, Λ, survives on average. Likewise, the total electron spin also precesses rapidly about the internuclear axis, due to its coupling to the surviving component Λ of $\mathbf{L}$ caused by the spin-orbit interaction. The surviving component of $\mathbf{S}$ about the internuclear axis is called Σ. The spin and orbital angular momentum projections combine to give the value $\Omega = |\Lambda + \Sigma|$ which can range from $|\Lambda - S|$ to $\Lambda + S$. Each of these projections, Λ, Σ, and Ω has a well defined value and is considered a good quantum number in case (a). The combination of the electron angular momentum, Ω, with the nuclear rotation, $\mathbf{N}$, gives the total angular momentum, $\mathbf{J}$.

Ro-vibrational levels of electronic states in Hund's case (a) are labeled using the notation $n^{2S+1}\Lambda_\Omega(v, J)$. The value of n corresponds to the ordering in energy, from lowest to highest, of electronic states of the same symmetry. For example, the upper state of NaK used in this work is the $3^1\Pi_1$ state, meaning it is the third lowest lying $^1\Pi_1$ electronic state. Traditionally, these molecular states have been labeled with letters instead of numbers, and this older notation will be used in conjunction with the numbering scheme in this work. For historical reasons, the ground state is often labeled as the X state. The superscript $2S + 1$ gives the spin multiplicity. In the neutral diatomic alkali molecules, the spin multiplicity must be either one ($S = 0$) or three ($S = 1$) due to the two valence electrons, each of spin $\frac{1}{2}$, that can pair in a parallel or anti-parallel fashion. The corresponding states are referred to as "singlet" and "triplet" states, respectively. The Λ value, which refers to the component of orbital angular momentum along the nuclear axis, is labeled according to the scheme listed in Table 2.2. Each state is further divided into the various Ω components and are labeled by a subscript. Finally, the v and J quantum numbers are the vibrational and rotational quantum numbers discussed above. Additionally,

the Σ electronic states are designated by a plus or minus superscript (Σ^+ and Σ^- states). The plus or minus denotes whether the wavefunction changes sign or not, respectively, when electron coordinates are reflected in a plane containing the two nuclei. For example, the electronic ground state $1(X)^1\Sigma^+$ wavefunction is unchanged under this reflection operation.

Λ	State
0	Σ
1	Π
2	Δ
3	Φ

Table 2.2: Labels for molecular states with certain Λ values. The molecular labeling scheme is analogous to the atomic labeling scheme: S, P, D, F..., corresponding to $L = 0, 1, 2, 3....$

2.4.2 Hund's Case (b)

In Hund's case (b), the spin of the electrons is either not coupled to the internuclear axis or is only very weakly coupled. As a result, Σ and Ω are no longer valid quantum numbers. As shown in Fig. 2.5, the electronic orbital angular momentum still couples strongly to the internuclear axis resulting in the projection, Λ, being a good quantum number. However, when $\Lambda = 0$ and $S \neq 0$, the spin vector is not coupled to the internuclear axis (no spin-orbit interaction) and in the case of light molecules with $\Lambda \neq 0$, the spin vector may only very weakly couple to the internuclear axis (very weak spin-orbit coupling). Instead, the electron orbital angular momentum component Λ couples with the nuclear rotational angular momentum to form a new vector, $\mathbf{K}$. The spin vector then adds to $\mathbf{K}$, resulting in the total angular momentum, $\mathbf{J} = \mathbf{S} + \mathbf{K}$. Thus, $\mathbf{S}$ and $\mathbf{K}$ precess about each other (or alternatively about their resultant $\mathbf{J}$). The value of the quantum number J can range from $|K - S|$ to $(K + S)$ and is a half integer or integer value depending on the total spin. Case (b) molecules are labeled similarly to case (a), however, true

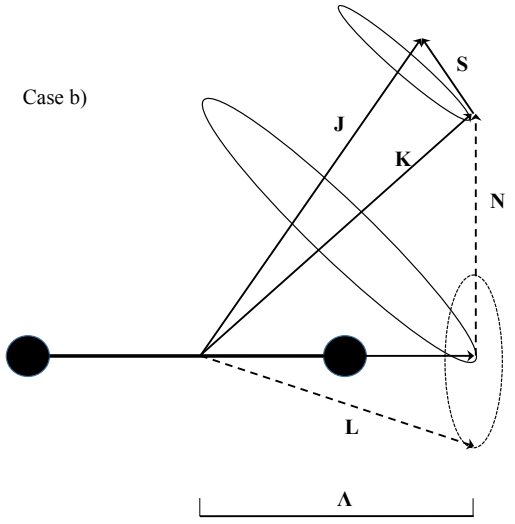

Figure 2.5: Vector diagram for Hund's case (b) using the notation in [35]. Each ellipse demonstrates the precession of the corresponding vector.

case (b) molecules have no well-defined Ω value. As Ω is not a valid quantum number, the term in brackets in the Dunham expansion (2.38) becomes $[K(K+1) - \Lambda^2]$.

2.4.3 Hund's Case (c)

In Hund's case (c), the spin-orbit (L-S) coupling is very large. Unlike the situation in case (a), **L** and **S** couple more strongly to each other than to the internuclear axis. In this case, the Σ and Λ values are no longer valid quantum numbers. This type of spin-orbit interaction typically occurs in heavy molecules such as NaCs. As shown in Fig. 2.6, the orbital angular momentum vector and the spin angular momentum vector couple to form the vector $\mathbf{J_a}$. $\mathbf{J_a}$ couples to the internuclear axis with a constant component $\mathbf{\Omega}$. Therefore, Ω is still a good quantum number in case (c). As in case (a), the total angular momentum vector **J** results from the combination of the nuclear rotation **N** and $\mathbf{\Omega}$.

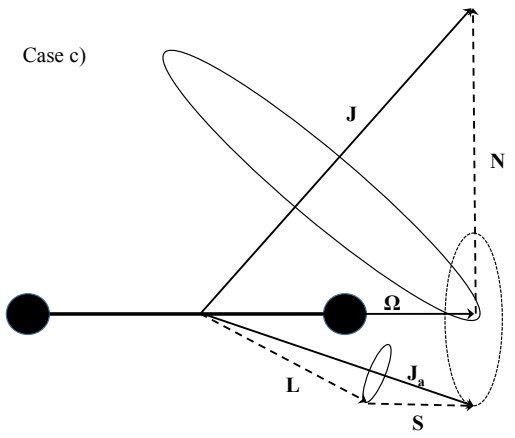

Figure 2.6: Vector diagram for Hund's case (c) using the notation in [35]. Each ellipse demonstrates the precession of the corresponding vector.

It is common when referring to electronic states of alkali diatomic molecules to use the Hund's case (a) notation even in situations where case (c) is a better approximation. This approach allows comparison to the better known light molecules and therefore doesn't always provide an accurate description of the molecular states. It is also true that Hund's cases are ideal situations, and the real molecular state might actually be an intermediate case. For NaCs, it is more accurate to use a Hund's case (c) notation because it is a heavy molecule with large spin-orbit coupling. The labeling used in this situation is $n(\Omega^{(+/-)})$. Again, the n value denotes the ordering of electronic states and Ω is the quantum number associated with the projection of $\mathbf{J_a}$ onto the internuclear axis. The plus-minus symmetry of the wavefunction upon reflection about a plane containing the nuclei is also included. For example, we label the upper state in our collisional study of NaCs as the $11(0^+)$ electronic state. We also colloquially refer to this state as the $5^3\Pi_0$ electronic state. A more detailed discussion about this state can be found in Ref. [9]. Interactions of the $11(0^+)$

electronic state with the $12(0^+)$ electronic state (also labeled $7^1\Sigma^+$) are described in Ref. [38].

2.5 Electronic Transitions

A molecule in the presence of an electromagnetic wave has a probability of absorbing a photon and making a transition to a higher electronic state. Such a transition occurs only when the energy of the photon matches the energy difference between specific ro-vibrational levels of the upper and lower electronic states; i.e., where $\nu = (\Delta E)/h$. Likewise, the excited molecule can also emit a photon and simultaneously make a transition from a particular ro-vibrational levels of an upper electronic state to a level of a lower electronic state. Following Refs. [35], [37], and [39], the Einstein coefficients of spontaneous emission and absorption are

$$A_{nm} = \frac{8\pi^2 \nu_{nm}^3}{3\epsilon_0 c^3 \hbar} \frac{|\mu_{nm}|^2}{2J_n + 1} \tag{2.39}$$

and

$$B_{mn}^{\rho} = \frac{1}{6\epsilon_0 \hbar^2} \frac{|\mu_{nm}|^2}{2J_m + 1} g(\nu - \nu_{nm}) \tag{2.40}$$

where $g(\nu - \nu_{nm})$ is the normalized lineshape function ($\int g(\nu - \nu_{nm}) d\nu = 1$), ν is the photon frequency, and ν_{nm} is the line center frequency corresponding to the transition energy. The absorption rate is given by $B_{mn}^{\rho}\rho(\nu)$, where $\rho(\nu)$ is the radiation energy density at frequency ν (energy/m^3) in the incident (collimated) beam. For our work, we are more interested in absorption of photons from a laser, and so we write the B coefficient in terms of $I(\nu)$, which is the incident intensity at frequency ν (energy/s-m^2):

$$B_{mn}^{I} I(\nu) = B_{mn}^{\rho} \rho(\nu)\,. \tag{2.41}$$

And as $I(\nu) = c\rho(\nu)$,

$$B_{mn}^{I} = \frac{B_{mn}^{\rho}}{c} = \frac{1}{6\epsilon_0 \hbar^2 c} \frac{|\mu_{nm}|^2}{(2J_m + 1)} g(\nu - \nu_{nm}). \tag{2.42}$$

In these expressions, μ_{nm} is the transition electric dipole matrix element defined by

$$\mu_{nm} = \int\int \Psi_n^* \hat{\mu} \Psi_m d\tau_{el} d\tau_{nuc} \tag{2.43}$$

where $\hat{\mu}$ is the electric dipole operator of the molecule:

$$\hat{\mu} = Z_A e \mathbf{R}_A + Z_B e \mathbf{R}_B - e \sum_i \mathbf{r}_i \,. \tag{2.44}$$

Here the first two terms are the contributions to the dipole moment from the two nuclei weighted by the vector location of each nucleus (measured from the the center of mass to the nucleus). The last term is the contribution due to the various electrons. If $n = m$, Eq. (2.43) gives the permanent dipole moment of the molecule in state n, which is only non-zero for heteronuclear molecules.

The electric dipole operator can be separated into the nuclear and electronic parts,

$$\hat{\mu} = \hat{\mu}_{nuc} + \hat{\mu}_{el} \,, \tag{2.45}$$

with $\hat{\mu}_{nuc} = Z_A e \mathbf{R}_A + Z_B e \mathbf{R}_B$ and $\hat{\mu}_{el} = -e \sum_i \mathbf{r}_i$. When the molecule makes a transition from one electronic state to a different electronic state, the contribution from $\hat{\mu}_{nuc}$ is zero because the electron wavefunctions are orthogonal. After inserting Eqs. (2.45) and (2.43) into Eq. (2.39) one obtains [35, 37, 39],

$$A_{nm} = \frac{8\pi^2 \nu_{nm}^3 S_{J_n,J_m}}{3\epsilon_0 c^3 \hbar (2J_n + 1)} \left| \int \chi_n^{v*} \chi_m^v dR \int \phi_n^{el*} \hat{\mu}^{el} \phi_m^{el} d\tau_{el} \right|^2 , \tag{2.46}$$

where we have separated the total wavefunction into products of the electronic and nuclear wavefunctions as in Eq. (2.9). We have further factored the nuclear wavefunction into radial and angular functions according to Eq. (2.19). The integration of the nuclear angular coordinates eliminates the rotational wavefunctions and results in Hönl-London factors, S_{J_n,J_m}. The Hönl-London factors represent the rotational line strength, and are dependent on the rotational quantum numbers in the transition [39]. Specifically, they also lead to selection rules on J, Λ, and Ω for electronic transitions.

Once the angular factors have been integrated out, only the electronic and vibration terms remain. Assuming that the transition electric dipole moment function ($\int \phi_n^{el*} \hat{\mu}^{el} \phi_m^{el} d\tau_{el} \equiv \mu_{nm}^{el}(R)$) depends only weakly on R, it can be removed from the integral over R to yield

$$A_{nm} = \frac{8\pi^2 \nu_{nm}^3 S_{J_n,J_m}}{3\epsilon_0 c^3 \hbar (2J_n+1)} \left|\overline{\mu_{nm}^{el}(R)}\right|^2 \left| \int \chi_n^{v*} \chi_m^v dR \right|^2, \tag{2.47}$$

where $\overline{\mu_{nm}^{el}(R)}$ is the value of $\mu_{nm}^{el}(R)$ averaged over the vibrational wavefunctions. The vibrational wavefunction overlap integral squared, appearing on the right hand side of Eq. (2.47), is called the Franck-Condon factor.

The intensity of an emission line (energy emitted per second per m^3)involving upper state n and lower state m, depends on the Franck-Condon factor and is given by

$$I_{em} = h\nu_{nm} A_{nm} n_n = \frac{16\pi^3}{3\epsilon_0 c^3} n_n \nu_{nm}^4 \frac{S_{J_n,J_m}}{2J_n+1} \left|\overline{\mu_{nm}^{el}(R)}\right|^2 \left| \int \chi_n^{v*} \chi_m^v dR \right|^2. \tag{2.48}$$

Similarly, the intensity of an absorption line is given by

$$\begin{aligned} I_{abs}(\nu) &= I_0(\nu) \Delta x h \nu_{nm} n_m B_{mn}^I \\ &= \frac{2\pi I_0(\nu) \Delta x \nu_{nm} n_m g(\nu - \nu_{nm})}{6c\epsilon_0 \hbar} \frac{S_{J_n,J_m}}{2J_m+1} \left|\overline{\mu_{nm}^{el}}(R)\right|^2 \left| \int \chi_n^{v*} \chi_m^v dR \right|^2. \end{aligned} \tag{2.49}$$

The terms n_n and n_m are the number densities of molecules (m^{-3}) in the initial states of the transition (n and m, respectively, for emission and absorption), $I_0(\nu)$ is the incident light intensity at frequency ν and Δx is the width of the absorbing medium.

From the analysis of electronic transition probabilities, one can also derive various selection rules. Selection rules for electronic transitions arise from considering the Hönl-London factors and the matrix elements of the transition electric dipole

moment operator. The selection rules for transitions in Hund's case (a) are:

$$\Delta\Lambda = 0, \pm 1 \tag{2.50a}$$

$$\Delta S = 0 \tag{2.50b}$$

$$\Delta\Sigma = 0 \tag{2.50c}$$

$$\Delta\Omega = 0, \pm 1 \tag{2.50d}$$

$$\Delta J = 0, \pm 1 \tag{2.50e}$$

where $\Delta J = 0$ is forbidden for a $\Sigma \leftrightarrow \Sigma$ or $\Omega = 0 \leftrightarrow \Omega = 0$ transition. The selection rules on Σ and Ω, Eqs. (2.50c) and (2.50d), are not valid for Hund's case (b) where Σ and Ω are not defined. The first three selection rules, (2.50a), (2.50b), and (2.50c) are not valid in Hund's case (c). Further discussion on the selection rules can be found in Refs. [35] and [37]. There is no selection rule on Δv in electronic transitions. However, as electronic transition intensities depend on the square of the vibrational wavefunction overlap integral, some transitions are stronger than others.

Chapter 3

Empirical Model of Collisional Transfer of Population and Orientation

3.1 Overview

In this chapter, I discuss the theoretical basis of our collision experiment. Beginning in Sec. 3.2, I discuss the population transfer resulting from an inelastic collision that changes the rotational quantum number J. This section on population transfer addresses a steady-state, two-level rate equation model we use to analyze our spectral data.

In order to understand orientation transfer collisions, I begin in Sec. 3.3 with the theory behind the technique of polarization spectroscopy (experimental details are described in Sec. 5.4). Also in Sec. 3.3, I describe the effects of the heat pipe oven windows and alkali vapor on the polarization of a propagating probe laser beam, and the polarization spectroscopy line shapes. Finally, in Sec. 3.4 I address the transfer of orientation again using a steady-state, two-level rate equation model, and compare our definition of orientation to the definition used in a previous NaK collision study by Wolfe *et al.* [30].

3.2 Collisional Transfer of Population

As discussed in more detail in Sec. 5.3, we excite NaK or NaCs molecules from the ground state, $1(X)^1\Sigma^+$, to a particular ro-vibrational level of an intermediate state, $2(A)^1\Sigma^+$, using a continuous wave (cw) laser. During the lifetime of the molecule in the intermediate state, it can undergo an inelastic collision with another atom or molecule in the heat pipe oven that changes the rotational level, vibrational level, or both of the initial molecule. A second cw laser is used as a probe to determine what happened. In our system, the dominant collision partners are the buffer gas atoms and either potassium atoms in the NaK heat pipe or cesium atoms in the NaCs heat pipe. Fluorescence data give information about population transfer during a collision, or specifically what fraction of the molecules in the directly populated ro-vibrational level (level $1'$ below) move into a neighboring ro-vibrational level (level $2'$ below) due to the collision. To describe the relevant processes, we write a rate equation describing a simple two-state model of rotationally inelastic collisions (see Fig. 3.1),

$$\dot{n}_{2'} = 0 = k_{buf}^{\Delta J} n_{buf} n_{1'} + k_{alk}^{\Delta J} n_{alk} n_{1'} - k_{buf}^{Q} n_{buf} n_{2'} - k_{alk}^{Q} n_{alk} n_{2'} - \Gamma n_{2'} \,. \qquad (3.1)$$

The factors $k_{buf}^{\Delta J}$ and $k_{alk}^{\Delta J}$ are the collisional rate coefficients describing collisions with buffer gas atoms and alkali atoms, respectively, that move population into level $2'$ from level $1'$. The remaining terms involving k_{buf}^{Q}, k_{alk}^{Q}, and Γ describe the population that leaves state $2'$ by quenching collisions with buffer gas and alkali perturbers and by radiative decay to all other energy states, respectively. The value of Γ is determined from the $1(X)^1\Sigma^+$ and $2(A)^1\Sigma^+$ potentials of Russier-Antoine *et al.* [10] and Ross *et al.* [11], respectively, and the transition dipole moment function of Magnier *et al.* [33] using the computer code LEVEL 8.0 by R.J. LeRoy [40]. The various n values in Eq. (3.1) refer to the number densities of buffer gas atoms, alkali perturbers, and molecules in either the directly populated level $1'$ or collisionally populated level $2'$. This simple model assumes a single collision regime (where level $2'$ is not significantly populated from some level $3'$, which is itself populated collisionally from level $1'$). We also assume that the pumping rate of the probe beam is small compared to the radiative decay rate, and can therefore be neglected.

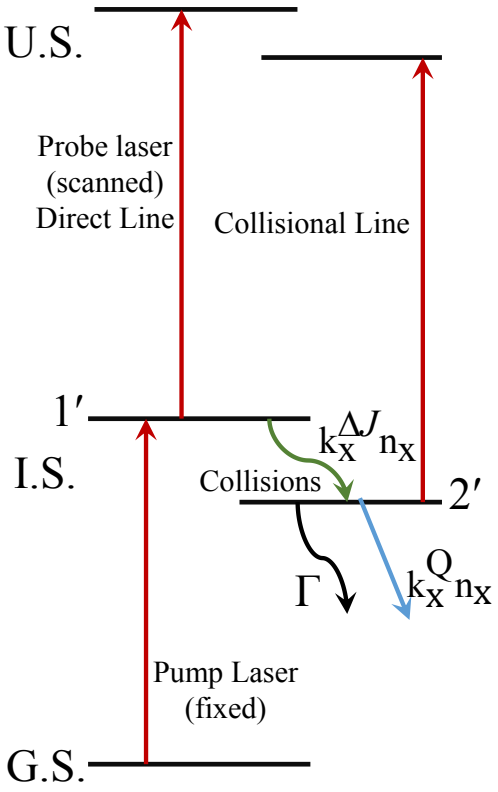

Figure 3.1: Schematic diagram showing collisional and radiative population transfer mechanisms included in the rate equation model of Eq. (3.1). The molecule is first excited from the ground state (G.S.) to the intermediate state (I.S.) using the pump laser of fixed frequency. Collisions take population from the directly populated level ($1'$) to the collisionally populated level ($2'$). A probe laser is used to scan over transitions involving the directly populated and collisionally populated levels to excite the molecule to specific ro-vibrationals level in the upper state (U.S.). The subscript X represents the perturber, either buffer gas or alkali.

When Eq. (3.1) is rearranged, we obtain the ratio of density in the collisionally populated level $2'$ to the density in the directly populated level $1'$,

$$\frac{n_{2'}}{n_{1'}} = \frac{k_{buf}^{\Delta J} n_{buf} + k_{alk}^{\Delta J} n_{alk}}{\Gamma + k_{buf}^{Q} n_{buf} + k_{alk}^{Q} n_{alk}} \,. \tag{3.2}$$

It is useful to divide through the numerator and denominator by Γ,

$$\frac{n_{2'}}{n_{1'}} = \frac{\frac{k_{buf}^{\Delta J}}{\Gamma} n_{buf} + \frac{k_{alk}^{\Delta J}}{\Gamma} n_{alk}}{1 + \frac{k_{buf}^{Q}}{\Gamma} n_{buf} + \frac{k_{alk}^{Q}}{\Gamma} n_{alk}} \,. \tag{3.3}$$

We fit our data obtained with different combinations of buffer gas and alkali densities, to a function of this general form, in order to determine rate coefficients for J-changing collisions of interest and for quenching collisions. This process will be discussed in more detail in Chapter 6. Experimentally, the population transfer information is determined by comparing recorded fluorescence intensities for "collisional satellite lines" and "directly populated lines" following excitation to levels of a higher electronic state using the probe laser.

In general, the measured probe laser-induced fluorescence intensity is given by

$$I^F = n_{upper} \Gamma_{u \to l} h \nu_{u \to l} \epsilon_{u \to l} \frac{d\Omega}{4\pi} a_{u \to l} V \,, \tag{3.4}$$

where n_{upper} is the density of molecules in the upper level excited by the probe laser, typically a level of the $3^1\Pi$ electronic state for NaK or the $5^3\Pi$ electronic state for NaCs in our collision experiments. The term, $\Gamma_{u \to l}$, is the radiative rate for the observed fluorescence transition or transitions; ro-vibrational transitions of $3^1\Pi \to 1(X)^1\Sigma^+$ in NaK or $5^3\Pi \to 1(a)^3\Sigma^+$ in NaCs. $\nu_{u \to l}$ is the weighted average fluorescence transition frequency, $\epsilon_{u \to l}$ is the relative detector efficiency for the observed fluorescence, $d\Omega$ is the solid angle subtended by the detector, $a_{u \to l}$ is an anisotropy factor depending on the polarization of the fluorescence, and V is the detection volume. We assume that $n_{upper} \propto n_{i'} \Gamma_{u \to i'} I_{probe}$ where $i' = 1'$ or $2'$ is the level of interest and $\Gamma_{u \to i'}$ and I_{probe} are the transition rate for the probe transition and the probe laser intensity, respectively. In addition, we assume that radiative rates are the same for neighboring P lines (or R lines) of the same electronic transition and vibrational band, but J levels that differ by only one or a few units. Similarly, we assume that $\epsilon_{u \to l}$, $\nu_{u \to l}$, and $a_{u \to l}$ are approximately equal for neighboring rotational transitions. Thus we find that the ratio of the probe laser induced collisional line fluorescence intensity to the probe laser induced direct line fluorescence intensity,

as recorded in the lab, is given by

$$R_F \equiv \frac{I^F_{col}}{I^F_{dir}} = \frac{n_{col(2')}}{n_{dir(1')}}. \tag{3.5}$$

Combining Eq. (3.5) with Eq. (3.3), where the collisionally populated level is $n_{2'}$ and the directly populated level is $n_{1'}$, we obtain the relationship between the fluorescence line intensities and the collisional and radiative transfer rates,

$$R_F = \frac{I^F_{col}}{I^F_{dir}} \approx \frac{n_{col}}{n_{dir}} = \frac{\frac{k^{\Delta J}_{buf}}{\Gamma} n_{buf} + \frac{k^{\Delta J}_{alk}}{\Gamma} n_{alk}}{1 + \frac{k^{Q}_{buf}}{\Gamma} n_{buf} + \frac{k^{Q}_{alk}}{\Gamma} n_{alk}}\,. \tag{3.6}$$

Data are gathered for various J changing collisions, buffer gas densities, and alkali metal vapor densities. Methods of obtaining the buffer gas and alkali perturber densities from our experimental set up are described in Sec. 5.2.

3.3 Polarization Spectroscopy

The orientation transfer study involves a different method called polarization labeling (PL) spectroscopy, often referred to in this work as simply polarization spectroscopy. The polarization spectroscopy experimental technique is addressed in greater detail in Sec. 5.4. Polarization spectroscopy utilizes a circularly polarized (pump) laser beam as a first step in the excitation scheme to create a non-uniform population among the the NaK M_J sublevels of the intermediate state. This is done utilizing the selection rule that $\Delta M_J = \pm 1$ for a circularly polarized beam, with the sign depending on whether the beam is right or left circularly polarized ("+" for left and "–" for right). Whether the beam is left or right circularly polarized is not important for our experiment, as long as it creates a net orientation in the intermediate state; i.e., $\langle M'_J \rangle \neq 0$. A counter-propagating, linearly polarized (probe) beam is overlapped with the circularly polarized beam to induce a second excitation when in resonance with a transition frequency. One can think of the linearly polarized probe beam as having equal contributions of left and right circular polarization. Due to the preferential M_J population distribution created by the pump laser (as

demonstrated in an example in Fig. 3.2), when the probe beam is in resonance with a transition sharing a level with the pump transition, the left and right circular polarization components of the probe are unequally absorbed and/or experience a different index of refraction. When the two components are (figuratively) recombined at the exit window, the probe beam has acquired a slight elliptical polarization and some fraction of its intensity passes through a polarizer crossed with respect to the original linear probe beam polarization. We use a PMT to detect this light that passes through the polarizer. When the probe frequency is not on such a resonance, the probe beam maintains its linear polarization and is therefore blocked by the crossed analyzer, so that no signal is detected.

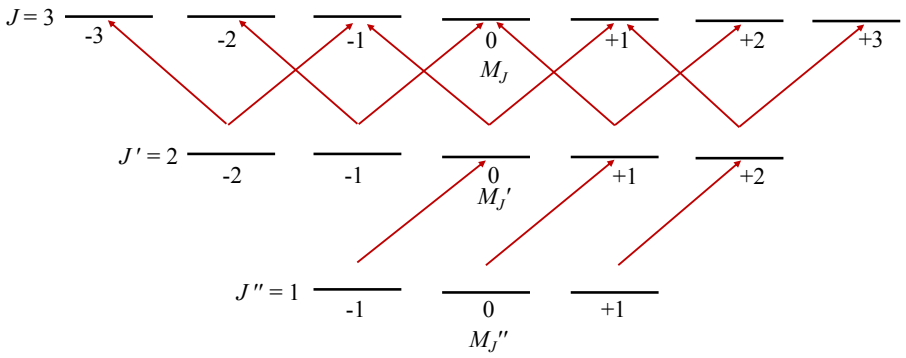

Figure 3.2: Schematic diagram showing how an orientation is prepared in the intermediate state using a circularly polarized pump beam (here we assume very low values of J for the purposes of illustration). The value of M_J is the projection of **J** onto the quantization axis and can take integer values from $-J$ to $+J$. We take the quantization axis to be the direction of the probe beam propagation. Notice the population in the lower state that is being excited by the pump laser is being driven toward higher M'_J values in the intermediate state.

When we look at the lineshape produced from this type of spectroscopy, we must consider the elements that affect the beam polarization along the probe beam path. In this section, we follow the derivation of the polarization spectroscopy lineshape presented by Demtröder [41], with some minor corrections addressed by Wolfe *et al.* [30].

First, we consider a laser beam propagating in the $+z$ direction and linearly polarized in the $+x$ direction with an electric field of the form

$$\mathbf{E}(z=0) = E_0 \hat{\mathbf{x}} e^{-i\omega t} \,. \tag{3.7}$$

The electric field can be written in a form containing equal contributions of left and right circular polarization,

$$\mathbf{E}(z=0) = \frac{E_0}{2}\left[(\hat{\mathbf{x}} + i\hat{\mathbf{y}})e^{-i\omega t} + (\hat{\mathbf{x}} - i\hat{\mathbf{y}})e^{-i\omega t}\right] \,. \tag{3.8}$$

So far, we have simply written an expression for the electric field of the EM wave at a fixed position ($z = 0$) in space. As the beam travels, it interacts with the windows of the heat pipe and with the vapor inside. The windows and the vapor each have different effects on the right and left circular components of the probe electric field. The complex indices of refraction for the left (+) and right (–) circular polarization components due to the windows (w) and vapor (v), are written as

$$n_w = \mathrm{Re}[n_w^{\pm}] + i\mathrm{Im}[n_w^{\pm}] \tag{3.9}$$

and

$$n_v = \mathrm{Re}[n_v^{\pm}] + i\mathrm{Im}[n_v^{\pm}] \,. \tag{3.10}$$

The real part of each index of refraction is responsible for the dispersion properties, whereas the imaginary part is responsible for the absorption properties. Both parts are dependent on the direction of circular polarization. When the beam propagates through the heat pipe, it passes through two windows, each of width d, and a total length L of vapor. Therefore, we can write the following expression, incorporating

the effects of the windows and vapor, for the probe laser beam electric field as it emerges from the far end of the heat pipe,

$$\begin{aligned}\mathbf{E} =& \frac{E_0}{2}\Bigg\{(\hat{\mathbf{x}} + i\hat{\mathbf{y}})\exp\left[i\left(\frac{2d\omega}{c}\mathrm{Re}[n_w^+] + \frac{L\omega}{c}\mathrm{Re}[n_v^+] - \omega t\right)\right] \\ & \times \exp\left[-\left(\frac{2d\omega}{c}\mathrm{Im}[n_w^+] + \frac{L\omega}{c}\mathrm{Im}[n_v^+]\right)\right] \\ & + (\hat{\mathbf{x}} - i\hat{\mathbf{y}})\exp\left[i\left(\frac{2d\omega}{c}\mathrm{Re}[n_w^-] + \frac{L\omega}{c}\mathrm{Re}[n_v^-] - \omega t\right)\right] \\ & \times \exp\left[-\left(\frac{2d\omega}{c}\mathrm{Im}[n_w^-] + \frac{L\omega}{c}\mathrm{Im}[n_v^-]\right)\right]\Bigg\}. \end{aligned} \tag{3.11}$$

To simplify Eq. (3.11), we define new parameters describing the effects due to the real and imaginary parts of the index of refraction from the windows and vapor, respectively:

$$b^{\pm} = \frac{2d\omega}{c}\mathrm{Re}[n_w^{\pm}] \tag{3.12a}$$

$$\beta^{\pm} = \frac{2d\omega}{c}\mathrm{Im}[n_w^{\pm}] \tag{3.12b}$$

$$n^{\pm} = \frac{L\omega}{c}\mathrm{Re}[n_v^{\pm}] \tag{3.12c}$$

$$\alpha^{\pm} = \frac{L\omega}{c}\mathrm{Im}[n_v^{\pm}]. \tag{3.12d}$$

The values of $b^{\pm}$ and $\beta^{\pm}$ represent the window dispersion and the window absorption, respectively. The vapor contributions for dispersion and absorption are $n^{\pm}$ and $\alpha^{\pm}$, respectively. Again, when considering either the windows or the vapor, it is assumed that the effects of dispersion and absorption might be different for left and right circularly polarized light. Redefining these terms in this way allows us to write Eq. (3.11) in a more compact form,

$$\mathbf{E} = \frac{E_0}{2}\left\{(\hat{\mathbf{x}} + i\hat{\mathbf{y}})\, e^{i(b^+ + n^+ - \omega t)}e^{-(\beta^+ + \alpha^+)} + (\hat{\mathbf{x}} - i\hat{\mathbf{y}})\, e^{i(b^- + n^- - \omega t)}e^{-(\beta^- + \alpha^-)}\right\}. \tag{3.13}$$

After the probe beam interacts with the windows and the oriented NaK molecules of the alkali vapor within the heat pipe, it is sent through an analyzer nearly crossed

with the original vertical polarization of the probe beam. Assuming there is a small uncrossing angle, θ, we can write the transmitted electric field through the analyzer,

$$E_t = \mathbf{E} \cdot \hat{\mathbf{y}}' = -E_x \sin\theta + E_y \cos\theta \,. \tag{3.14}$$

The axis of the polarizer, $\hat{\mathbf{y}}'$, is rotated at a small angle (θ) from the perfectly crossed axis, $\hat{\mathbf{y}}$. Based on Eq. (3.14), it is convenient to decompose the electric field at the analyzer into $\hat{\mathbf{x}}$ and $\hat{\mathbf{y}}$ components and we also define the parameters

$$\begin{aligned} b &= \frac{b^+ + b^-}{2}, & \Delta b &= \frac{b^+ - b^-}{2}, \\ \beta &= \frac{\beta^+ + \beta^-}{2}, & \Delta\beta &= \frac{\beta^+ - \beta^-}{2}, \\ n &= \frac{n^+ + n^-}{2}, & \Delta n &= \frac{n^+ - n^-}{2}, \\ \alpha &= \frac{\alpha^+ + \alpha^-}{2}, & \Delta\alpha &= \frac{\alpha^+ - \alpha^-}{2}, \end{aligned} \tag{3.15}$$

such that

$$\begin{aligned} b^+ &= b + \Delta b, & b^- &= b - \Delta b, \\ \beta^+ &= \beta + \Delta\beta, & \beta^- &= \beta - \Delta\beta, \\ n^+ &= n + \Delta n, & n^- &= n - \Delta n, \\ \alpha^+ &= \alpha + \Delta\alpha, & \alpha^- &= \alpha - \Delta\alpha. \end{aligned} \tag{3.16}$$

Substituting into the $\hat{\mathbf{x}}$ and $\hat{\mathbf{y}}$ components of the electric field given in Eq. (3.13), we obtain

$$E_x = \frac{E_0}{2} e^{i(b+n-\omega t)} e^{-(\beta+\alpha)} \{ e^{i(\Delta b+\Delta n)} e^{-(\Delta\beta+\Delta\alpha)} + e^{-i(\Delta b+\Delta n)} e^{(\Delta\beta+\Delta\alpha)} \}, \tag{3.17a}$$

$$E_y = \frac{E_0}{2} i e^{i(b+n-\omega t)} e^{-(\beta+\alpha)} \{ e^{i(\Delta b+\Delta n)} e^{-(\Delta\beta+\Delta\alpha)} - e^{-i(\Delta b+\Delta n)} e^{(\Delta\beta+\Delta\alpha)} \}. \tag{3.17b}$$

If we use Eqs. (3.17a) and (3.17b) in Eq. (3.14) we obtain

$$\begin{aligned} E_t = & \frac{E_0}{2} e^{i(b+n-\omega t)} e^{-(\beta+\alpha)} \{ -\sin\theta e^{i(\Delta b+\Delta n)} e^{-(\Delta\beta+\Delta\alpha)} - \sin\theta e^{-i(\Delta b+\Delta n)} e^{(\Delta\beta+\Delta\alpha)} \\ & + i\cos\theta e^{i(\Delta b+\Delta n)} e^{-(\Delta\beta+\Delta\alpha)} - i\cos\theta e^{-i(\Delta b+\Delta n)} e^{(\Delta\beta+\Delta\alpha)} \} \,. \end{aligned} \tag{3.18}$$

We can simplify Eq. (3.18) using the Euler equation, $e^{\pm i\theta} = \cos\theta \pm i\sin\theta$,

$$E_t = \frac{E_0}{2} e^{i(b+n-\omega t)} e^{-(\beta+\alpha)} \{ i e^{i(\Delta b+\Delta n+\theta)} e^{-(\Delta\beta+\Delta\alpha)} - i e^{-i(\Delta b+\Delta n+\theta)} e^{(\Delta\beta+\Delta\alpha)} \} . \quad (3.19)$$

To obtain the intensity of the transmitted light through the polarizer, we utilize $I = c\epsilon_0 |E|^2$:

$$\begin{aligned} I_t &= \frac{c\epsilon_0 E_0^2}{4} e^{-2(\beta+\alpha)} \{ e^{-2(\Delta\beta+\Delta\alpha)} + e^{2(\Delta\beta+\Delta\alpha)} - e^{2i(\Delta b+\Delta n+\theta)} - e^{-2i(\Delta b+\Delta n+\theta)} \} \\ &= \frac{I_0}{2} e^{-2(\beta+\alpha)} \{ \cosh\left[2(\Delta\beta+\Delta\alpha)\right] - \cos\left[2(\Delta n+\theta')\right] \} . \end{aligned} \quad (3.20)$$

In this last expression, the beam intensity incident on the heat pipe entrance window is $I_0 = c\epsilon_0 E_0^2$ and we have defined $\theta' = \theta + \Delta b$. The presence of this later combination in the result means that the effects of the window birefringence can be canceled out by changing the angle of the analyzer (i.e., using a slight uncrossing angle $\theta = -\Delta b$).

Use of the trigonometric identities,

$$\cos(A \pm B) = \cos A \cos B \mp \sin A \sin B \quad (3.21)$$

$$\cosh(A \pm B) = \cosh A \cosh B \pm \sinh A \sinh B , \quad (3.22)$$

allows us to rewrite the the above equation for the intensity as

$$\begin{aligned} I_t = & \frac{I_0}{2} e^{-2(\beta+\alpha)} \{ \cosh(2\Delta\beta)\cosh(2\Delta\alpha) + \sinh(2\Delta\beta)\sinh(2\Delta\alpha) \\ & - \cos(2\Delta n)\cos(2\theta') + \sin(2\Delta n)\sin(2\theta') \} . \end{aligned} \quad (3.23)$$

Assuming that the effects of the windows and vapor are small, and that the uncrossing angle of the analyzer is small, the trigonometric functions can be expanded through second order,

$$\begin{aligned} &\sin x \approx x, \\ &\cos x \approx 1 - \frac{x^2}{2}, \\ &\sinh x \approx x, \\ &\cosh x \approx 1 + \frac{x^2}{2}. \end{aligned}$$

Using these expansions and substituting back into Eq. (3.23), we obtain,

$$\begin{aligned} I_t =& \frac{I_0}{2} e^{-2(\beta+\alpha)} \{1 + 2(\Delta\beta)^2 + 2(\Delta\alpha)^2 + 4(\Delta\beta)^2(\Delta\alpha)^2 \\ &+ 4\Delta\beta\Delta\alpha - 1 + 2(\Delta n)^2 + 2(\theta')^2 - 4(\Delta n)^2(\theta')^2 + 4\Delta n\theta'\} \,, \end{aligned} \tag{3.24}$$

where the fourth and ninth terms in the expansion are fourth order in small quantities and must therefore be neglected for consistency.

Thus far in the derivation of the transmitted polarization signal, we have not considered the effects of various line broadening mechanisms. The bandwidth of the cw pump laser is sufficiently narrow that only a single velocity group of the thermal ground state velocity distribution is excited to the intermediate level. Thus the velocity distribution in the intermediate level is extremely narrow, and Doppler broadening effects on the probe laser transition are completely negligible. Pressure broadening and natural broadening can each be described by a Lorentzian lineshape, and the convolution of the two Lorentzians is itself a Lorentzian. Thus, the vapor dependent absorption term in Eq. (3.24) can be described well by a Lorentzian profile (due to the homogeneous line broadening mechanisms) about the line center transition frequency,

$$\Delta\alpha(\omega) = \frac{\Delta\alpha_0}{1 + x^2} \,. \tag{3.25}$$

Similarly, it can be shown using the Kramers-Kronig relation that the real part of the index can be represented by a dispersion profile,

$$\Delta n(\omega) = \frac{\Delta\alpha_0 x}{1 + x^2} \,. \tag{3.26}$$

Here, the subscript naught denotes a quantity evaluated at line center, $x = \frac{\omega_0 - \omega}{\frac{1}{2}\Gamma}$ is the dimensionless frequency detuning, and Γ is the homogeneous linewidth (FWHM). Substituting these expansions back into Eq. (3.24) and dropping the terms that are more than second order in small quantities, yields an expression containing the line

shape information,

$$I_t = I_0 e^{-2(\beta+\alpha)} \Bigg\{ (\Delta\beta)^2 + (\theta')^2 + 2\Delta\beta \frac{\Delta\alpha_0}{1+x^2} + 2\theta' \frac{\Delta\alpha_0 x}{1+x^2} + \left(\frac{\Delta\alpha_0}{1+x^2}\right)^2 + \left(\frac{\Delta\alpha_0 x}{1+x^2}\right)^2 \Bigg\} . \tag{3.27}$$

The last two terms of Eq.(3.27) can be combined,

$$\left(\frac{\Delta\alpha_0}{1+x^2}\right)^2 + \left(\frac{\Delta\alpha_0 x}{1+x^2}\right)^2 = \frac{\Delta\alpha_0^2}{1+x^2} . \tag{3.28}$$

Until now we have assumed that the polarization spectroscopy experiment utilizes perfect polarizers. A final term needs to be added to the result due to the non-zero polarizer extinction. The term ξ, represents the fraction of light transmitted through the analyzer if it is perfectly crossed with the polarizer ($\theta = 0$) and the heat pipe (vapor and windows) is removed from the experiment. Including this small term, which accounts for the imperfection of the polarizers, and again only keeping terms up to second order in small quantities, we obtain the final expression for the intensity transmitted through the analyzer [30],

$$I_t = I_0 e^{-2(\beta+\alpha)} \left\{ \xi + (\Delta\beta)^2 + (\theta')^2 + (2\Delta\beta + \Delta\alpha_0) \frac{\Delta\alpha_0}{1+x^2} + 2\theta' \frac{\Delta\alpha_0 x}{1+x^2} \right\} . \tag{3.29}$$

The first three terms contribute to the constant (frequency independent) background. The ξ term is due to the imperfect polarizers, the $\Delta\beta$ term results from the circular dichroism due to the uneven absorption of left and right circular polarized light in the windows, and the θ' term results from the combination of non-zero polarizer crossing angle θ and Δb, which represents the birefringence or difference in refractive index for left and right circularly polarized light in the windows. The dispersion term can be set to zero by adjusting the analyzer crossing angle to cancel the effects of the window birefringence ($\theta = -\Delta b$). These last two terms are indeed small, and a description of how the background terms are measured and how their

sum is minimized is given in Sec. 5.4.2. In the present work, we purposely set $\theta' = \theta + \Delta b = 0$ in order to eliminate the dispersion term and analyze the remaining Lorentzian line shape. It is important to realize that, in general, $\Delta\beta >> \Delta\alpha_0$, so the resulting Lorentzian line shape is linear in $\Delta\alpha_0$. The presence of the $(\Delta\alpha_0)^2$ Lorentzian term for particularly strong lines is a source of error in the direct line intensities. Alternatively, one could set $\theta' \neq 0$ and adjust $\Delta\beta$ (by adjusting the pressure on the heat pipe oven windows) such that dispersion line shapes are observed. This approach is advantageous for determination of absolute transition frequencies.

3.4 Collisional Transfer of Orientation

In the collisional transfer of orientation experiment, we create Lorentzian line shapes and determine intensities from integrated areas under the lines. We achieve the Lorentzian line shapes by adjusting the uncrossing angle (θ) to achieve the condition $\theta' \approx 0$. From the derivation of the polarization signal, Eq. (3.29), we see that the Lorentzian signal is dependent on the window circular dichroism and the difference in line center absorption of left and right circular polarized light by the vapor. The latter can be described by the difference in the total absorption of left and right circular polarized light by molecules distributed over the various magnetic sublevels (M'_J) of the intermediate level:

$$\begin{aligned} I &\propto \sum(\text{Left absorptions}) - \sum(\text{Right absorptions}) \\ &= \sum_{M'_J=-J'}^{+J'} n_{M'_J} F^L_{M'_J} - \sum_{M'_J=-J'}^{+J'} n_{M'_J} F^R_{M'_J} \\ &= \sum_{M'_J=-J'}^{+J'} n_{M'_J} \left(F^L_{M'_J} - F^R_{M'_J} \right) . \end{aligned} \tag{3.30}$$

Here the F values are proportional to the dipole transition probabilities for the individual M'_J level probe transitions described by Spano [42] and Wolfe *et al.* [30]. They are given superscripts R and L to represent the factors for right circular and left circular components, respectively. Specifically, $F^{L,R}_{M'_J}$ corresponds to the probability

that the molecule in sublevel M'_J will absorb a photon from the left circular or right circular polarized component of the probe beam. Following Wolfe *et al.* [30], a factor of one-half arises in the F factors so that the coefficients are normalized such that the branching ratios over J and M_J sum to one. The F factors for P, Q, and R transitions and $\Delta M_J = \pm 1$ are given in Table 3.1 for $^1\Sigma \rightarrow {}^1\Pi$ transitions.

ΔJ	$F^{L,R}_{M'_J}$
R Transitions $(J - J' = +1)$	$F^R_{M'_J} = \frac{(J'+2)}{2(J'+1)(2J'+1)(2J'+3)}(J' + M'_J + 1)(J' + M'_J + 2)$ $F^L_{M'_J} = \frac{(J'+2)}{2(J'+1)(2J'+1)(2J'+3)}(J' - M'_J + 1)(J' - M'_J + 2)$
Q Transitions $(J - J' = 0)$	$F^R_{M'_J} = \frac{1}{2J'(J'+1)}(J' - M'_J)(J' + M'_J + 1)$ $F^L_{M'_J} = \frac{1}{2J'(J'+1)}(J' + M'_J)(J' - M'_J + 1)$
P Transitions $(J - J' = -1)$	$F^R_{M'_J} = \frac{J'-1}{2J'(2J'+1)(2J'-1)}(J' - M'_J)(J' - M'_J - 1)$ $F^L_{M'_J} = \frac{J'-1}{2J'(2J'+1)(2J'-1)}(J' + M'_J)(J' + M'_J - 1)$

Table 3.1: The $F^{L,R}_{M'_J}$ values for a $^1\Sigma \rightarrow {}^1\Pi$ electronic transition used in our collisional study of NaK.

If we consider any single transition obeying the selection rule $\Delta J = \pm 1, 0$ (P, Q, or R), we can show that the difference $F^L_{M'_J} - F^R_{M'_J}$ is linearly dependent on the intermediate state M'_J sublevel value. We use a Q transition as an example

$$\begin{aligned} F^L_{M'_J} - F^R_{M'_J} &= \frac{1}{2J'(J'+1)}\left[(J' + M'_J)(J' - M'_J + 1) - (J' - M'_J)(J' + M'_J + 1)\right] \\ &= \frac{1}{2J'(J'+1)} 2M'_J \\ &= \frac{1}{J'(J'+1)} M'_J \,. \end{aligned} \tag{3.31}$$

This approach works for P and R transitions as well, and we may write in general that

$$F^L_{M'_J} - F^R_{M'_J} = f(J, J')M'_J \tag{3.32}$$

(see Ref. [42, 43]). The values for $f(J, J')$ depend on the type of transition (P, Q, or R) and are given in Table 3.2 for $^1\Sigma \rightarrow {}^1\Pi$ transitions. Using the appropriate $f(J, J')$ values for the transition, and noting that $f(J, J')$ is independent of M'_J, we can write Eq. (3.30) as

$$I \propto f(J, J') \sum_{M'_J=-J'}^{+J'} M'_J n_{M'_J} \,. \tag{3.33}$$

Previously, in the collisional study of Wolfe *et al.* [30], orientation was defined to be

$$\mathscr{O}^{Wolfe} \equiv \langle M'_J \rangle = \frac{\sum_{M'_J=-J'}^{+J'} M'_J n_{M'_J}}{\sum_{M'_J=-J'}^{+J'} n_{M'_J}} \,. \tag{3.34}$$

In the present work, we define orientation in a way that is more consistent with standard texts [44] and is also used by Hickman's group for calculations on NaK orientation transfer [45, 31]. The textbook definition is based on the angular momentum vector model shown in Fig. 3.3.

ΔJ	$f(J, J')$
R Transitions $(J - J' = +1)$	$-\frac{(J'+2)}{(J'+1)(2J'+1)}$
Q Transitions $(J - J' = 0)$	$\frac{1}{J'(J'+1)}$
P Transitions $(J - J' = -1)$	$\frac{(J'-1)}{J'(2J'+1)}$

Table 3.2: The $f(J, J')$ values for $^1\Sigma \rightarrow {}^1\Pi$ electronic transitions used in our collisional study of NaK.

From this model, the orientation in the intermediate (primed) state is defined as [44],

$$\mathscr{O} = \langle \cos\theta \rangle = \left\langle \frac{M'_J}{\sqrt{J'(J'+1)}} \right\rangle . \tag{3.35}$$

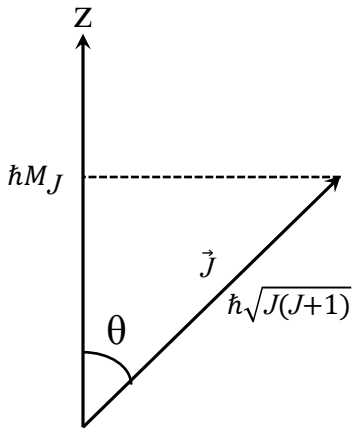

Figure 3.3: Vector diagram showing the rotational angular momentum, $\vec{J}$, and its component M_J along the laboratory fixed z axis. The vector model is used to define the orientation of a system of molecules.

Because we are considering molecules prepared in a single J level of the intermediate state, we determine the orientation from Eqs. (3.34) and (3.35),

$$\mathscr{O} = \frac{\langle M'_J \rangle}{\sqrt{J'(J'+1)}} = \frac{\sum_{M'_J=-J'}^{+J'} M'_J n_{M'_J}}{\sqrt{J'(J'+1)} \sum_{M'_J=-J'}^{+J'} n_{M'_J}} \,. \tag{3.36}$$

As can be seen by combining Eqs. (3.33) and (3.34), the polarization spectroscopy signal is dependent on the population times orientation transfer,

$$I \propto f(J,J')\langle M'_J\rangle \sum_{M'_J=-J'}^{+J'} n_{M'_J} = f(J,J')\sqrt{J'(J'+1)}\mathscr{O} \sum_{M'_J=-J'}^{+J'} n_{M'_J}$$
$$= f(J,J')\mathscr{O}^{Wolfe} \sum_{M'_J=-J'}^{+J'} n_{M'_J}\,. \tag{3.37}$$

In order to observe a polarization spectroscopy signal when probing a collisional line transition, population needs to be transferred in the collision, but without completely destroying the orientation. Similar to the argument made for population intensity ratios, we assume that other factors influencing the intensity of the detected signal (probe transition radiative rate, detector efficiency, etc.) are the same for the direct and collisional lines. Therefore, the collisional line to direct line intensity ratio is given by

$$\frac{I^P_{col}}{I^P_{dir}} = \frac{f(J_{col},J'_{col})\mathscr{O}^{Wolfe}_{col} n_{col}}{f(J_{dir},J'_{dir})\mathscr{O}^{Wolfe}_{dir} n_{dir}}$$
$$= \frac{f(J_{col},J'_{col})\sqrt{J'_{col}(J'_{col}+1)}\mathscr{O}_{col} n_{col}}{f(J_{dir},J'_{dir})\sqrt{J'_{dir}(J'_{dir}+1)}\mathscr{O}_{dir} n_{dir}}\,. \tag{3.38}$$

In the case of large J and small $|\Delta J|$, the polarization intensity ratio reduces to

$$\frac{I^P_{col}}{I^P_{dir}} \approx \frac{\mathscr{O}^{Wolfe}_{col} n_{col}}{\mathscr{O}^{Wolfe}_{dir} n_{dir}} \approx \frac{\mathscr{O}_{col} n_{col}}{\mathscr{O}_{dir} n_{dir}}\,, \tag{3.39}$$

assuming the collisional and direct probe transitions are of the same type (i.e. both P lines).

Similar to the analysis of the population transfer measurements, and following Wolfe *et al.* [30] we can write a rate equation representing the collisionally induced population and orientation transfer for our steady state experiment:

$$\frac{d}{dt}\left(\mathscr{O}_{col} n_{col}\right) = 0 = k^{O,\Delta J}_{buf} n_{buf}\mathscr{O}_{dir} n_{dir} + k^{O,\Delta J}_{alk} n_{alk}\mathscr{O}_{dir} n_{dir}$$
$$- g_{buf} n_{buf}\mathscr{O}_{col} n_{col} - g_{alk} n_{alk}\mathscr{O}_{col} n_{col} - \Gamma\mathscr{O}_{col} n_{col}\,. \tag{3.40}$$

Here, the rate coefficient $k_X^{O,\Delta J}$ (X is the perturber) corresponds to transfer of population and orientation and is related to the population rate coefficient introduced in Sec. 3.2,

$$k_X^{O,\Delta J} = k_X^{\Delta J}(1 - f_X^{\Delta J})\,. \tag{3.41}$$

The value of $f_X^{\Delta J}$ is the probability (or fraction of) orientation that is *destroyed* during a collision. The term g_X is the total collisional rate of destruction of orientation for the collisional level (i.e., in collisions occurring after the collisional level is initially populated). g_X includes the rate coefficient for any collision that removes population from the collisional level (k_X^Q from Sec. 3.2) plus the rate coefficient for collisions that do not change J but still scramble the M_J level population (denoted by g'_X),

$$g_X = k_X^Q + g'_X\,. \tag{3.42}$$

If we substitute the quenching and orientation transfer rate coefficients, Eqs. (3.41) and (3.42), into Eq. (3.40) and solve for the ratio of population times fraction of orientation transferred during a collision $\left(\frac{\mathscr{O}_{col} n_{col}}{\mathscr{O}_{dir} n_{dir}}\right)$ we obtain,

$$R_P \equiv \frac{I^P_{col}}{I^P_{dir}} = \frac{f(J_{col}, J'_{col})\sqrt{J'_{col}(J'_{col}+1)}}{f(J_{dir}, J'_{dir})\sqrt{J'_{dir}(J'_{dir}+1)}} \left[\frac{\frac{k_{buf}^{\Delta J}}{\Gamma}(1-f_{buf})n_{buf} + \frac{k_{alk}^{\Delta J}}{\Gamma}(1-f_{alk})n_{alk}}{1 + \frac{k_{buf}^{Q}+g'_{buf}}{\Gamma}n_{buf} + \frac{k_{alk}^{Q}+g'_{alk}}{\Gamma}n_{alk}}\right]. \tag{3.43}$$

We note that Eq. (3.43) differs from Eq. (27) in Wolfe *et al.* [30] by the $\sqrt{J'(J'+1)}$ factors. This means the orientation factors $(1-f)$ defined in the present work are a factor of $\frac{\sqrt{J'_{col}(J'_{col}+1)}}{\sqrt{J'_{dir}(J'_{dir}+1)}}$ smaller than the values defined by Wolfe. In the work of Wolfe *et al.*, the data were recorded for $J'_{dir} = 30$ and $|\Delta J| \leq 4$. Thus, this difference in definition of orientation results in differences in reported orientation transfer rate coefficients of $\sim 13\%$ for $|\Delta J| = 4$, and $\sim 6.5\%$ for $|\Delta J| = 2$. In the present work, we have chosen not to include the $\frac{\sqrt{J'_{col}(J'_{col}+1)}}{\sqrt{J'_{dir}(J'_{dir}+1)}}$ factor so that the f-values reported here are directly comparable to those of Wolfe *et al.* However, we will include these factors in a more complete analysis that is planned for publication in the near future.

We assume that the value of g'_X is small compared to the quenching rate coefficient k_X^Q. In the work of Wolfe *et al.* [30], the value of g'_X was approximated

as

$$g'_X = \frac{1}{2}\left(f_X^{\Delta J=-1} k_x^{\Delta J=-1} + f_X^{\Delta J=+1} k_x^{\Delta J=+1}\right) . \tag{3.44}$$

This approximation was made assuming that the rate coefficients for collisions that change orientation but not J should be approximately equal to the average of the rate coefficients for collisions that change J by ± 1 and simultaneously destroy orientation. Although this assumption seems reasonable, there is no *a priori* reason to believe it is true. However, we think that an upper limit to g_X is provided by the rate coefficient for the collisional contribution to the direct line broadening (collisional rate of destruction of coherence) due to species X. The broadening rate coefficient k_X^{br} reflects the effects of all phase changing interactions of the NaK molecule with atoms of species X, including elastic collisions with regard to J and M_J. Thus we expect $g_X = g'_X + k_X^Q \leq k_X^{br}$.

Chapter 4

Experimental Setup

4.1 Overview

In this chapter, I will describe experiment, starting with containment of the alkali metal vapor in the heat pipe oven. First I will outline the principles of operation of the heat pipe. Section 4.2.1 details the design and construction of the heat pipe oven. Section 4.2.2 will describe how we determine alkali atom densities in the oven.

Section 4.3 provides a description of the lasers used to prepare diatomic alkali molecules in precise quantum states and to probe the populations in various levels after collisions have occurred. Section 4.4 describes the photon detection systems. A visual description of the experimental setup is shown in Fig. 4.1. The chapter concludes with a description (Sec. 4.5) of the FTS experimental setup used in Lyon.

4.2 Heat Pipe Oven

The heat pipe oven used in this experiment has six arms, with four lying in the horizontal plane (as it is depicted in Fig. 4.1) and two vertical arms. Of the two vertical arms, one short arm projecting downward acts as a well for liquid alkali

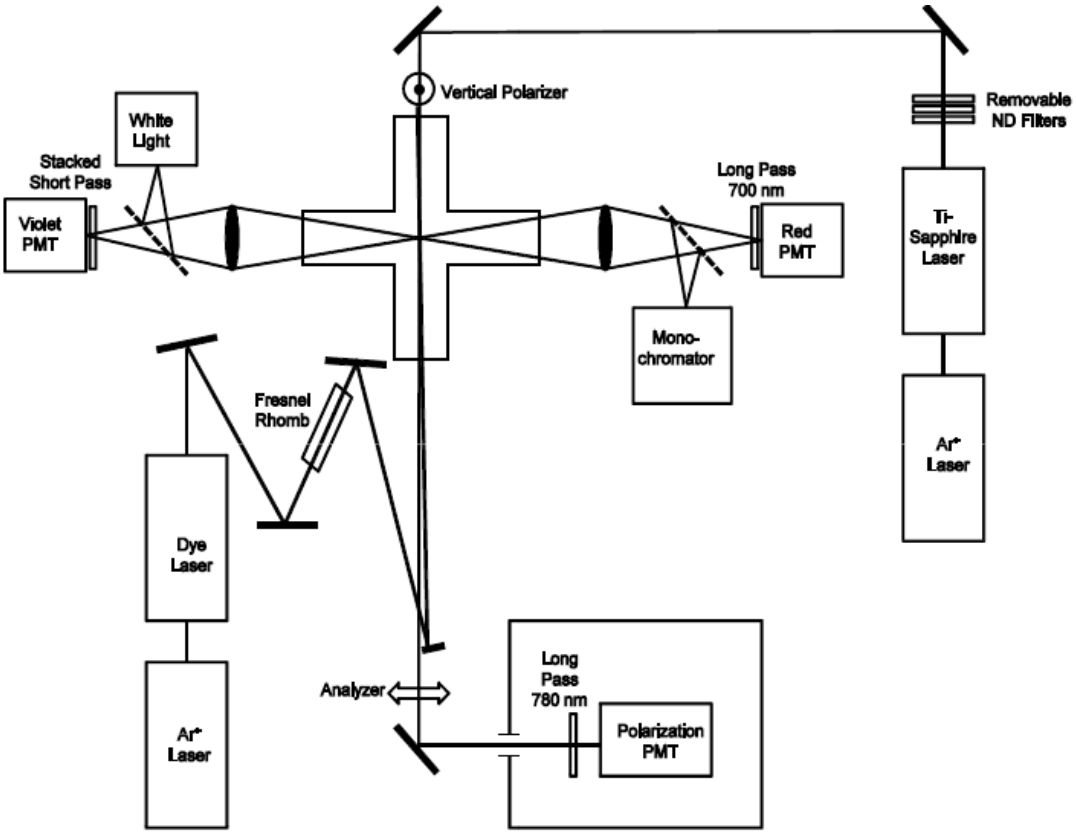

Figure 4.1: Experimental setup at Lehigh

metal near the center of the heat pipe. The design for a basic heat pipe oven was first published in 1969 by Vidal and Cooper [46].

4.2.1 Heat Pipe Oven: Theory of Operation

The heat pipe uses heating elements to liquefy and then evaporate the alkali metal sample that was previously loaded into the central region of the oven. As the alkali vapor moves out from the central region, it is met by an inert buffer gas. Inert gas enters the oven through a set of inlets located near the windows capping each arm. The buffer gas is necessary to prevent the alkali vapor from reaching and coating the cold windows. The ends of the arms are externally chilled with water cooling coils. When the hot alkali vapor meets the cold buffer gas, the alkali atoms condense onto

a rolled up stainless steel screen lining each arm. The screen acts as a wick, so that the liquid metal moves back to the center well of the heat pipe by capillary action.

There are two operating modes in which the heat pipe can be used: either in the "oven" or "heat pipe" mode. In either case, prior to heating, the oven is evacuated using a roughing pump. The heat pipe is then filled with buffer gas to a pressure that is equal to or greater than the desired alkali vapor pressure. When the heat pipe is running in the "oven" mode, the buffer vapor pressure is greater than the alkali metal vapor pressure. In this regime, the buffer gas fills the entire heat pipe, including the central region. When the buffer gas pressure is sufficiently larger than the metal vapor pressure, the buffer gas atoms are the dominant collision partners for collisions with the species of interest, excited diatomic alkali molecules in our case.

"Heat pipe" mode is attained when sufficient power is provided to the heaters that the alkali vapor pressure becomes equal to the buffer gas pressure. In heat pipe mode, there is a uniform temperature profile within the central hot region (see Ref. [46]). In this case, the buffer gas and metal vapor physically separate, and the buffer gas is excluded from the central region. The alkali vapor is almost exclusively confined to the central hot region, the buffer gas is confined primarily to the chilled region by the windows, and there is a short transition zone where they mix. The position of the intermediate zone can change based on the buffer gas vapor pressure and electrical power provided to the heaters. Thus, in "heat pipe" mode, the free alkali atoms in the metal vapor are the dominant collision partners.

4.2.2 Heat Pipe Oven Construction and Maintenance

The heat pipe used for the present NaK experiment was constructed by Laurie Morgus in the spring of 2004. In the spring of 2013, after prolonged use, the ability of the liquid metal to return to the center region began to seriously degrade. Eventually over time, some of the metal had oxidized and had collected on the mesh. When

this occurs, oxidized metal builds up and creates an obstruction for the pure liquid alkali metal, preventing it from returning to the center region. Because of their very different vapor pressures, the sodium and potassium metals tend to separate. In particular, the potassium metal migrates out of the central hot zone. This effect, combined with the degraded ability of the wick to return alkali metal to the center region of the oven, reduced signals due to low NaK molecule densities. In addition to the frequent cleaning of the oven arms, and loading the oven, our last working thermocouple attached to the oven exterior to measure temperature failed during the fall of 2013. Thus we decided that a major overhaul of the NaK heat pipe oven was needed.

Before we replaced the old stainless steel screen (the "mesh"), each arm and buffer gas line was carefully cleaned to remove any remaining alkali metal and oxides. To rebuild the heat pipe oven, we followed the detailed description of its construction presented in Laurie Morgus's thesis (where additional details can be found) [47]. We replaced the old mesh with new screen consisting of 0.0037" diameter stainless steel wire and containing 120x120 openings per square inch. The wire mesh was ordered in 12"x12" squares, which we cut and rolled into 8.5" long cylinders. When inserted into an arm of the oven, the mesh spanned the region from the edge of the central cross region to the inner edge of the cooling coils. When the mesh was inserted into the arm, it was rolled tightly and then released inside the arm in a way that allowed it to expand and fill the inner arm at a diameter of 1.375". Each arm was inspected to ensure the mesh was flush against the wall of the heat pipe, and that it did not obstruct the central cross region.

For each horizontal arm, a new circular BK7 glass window of 0.25" thickness and 2" diameter replaced the previous, deteriorated BK7 windows. Each window was re-seated into a Varian conflat flange secured onto the heat pipe. For better vacuum seals, new Viton type 223 O-rings were placed between each window and flange for every arm of the oven. The buffer gas supply line was run as a full circuit connecting to each arm (see Fig. 4.2), so that buffer gas would still reach each arm even if part of the tubing became blocked. In the previous design, the buffer gas

line made only a three-quarter circuit, so when a blockage occurred, buffer gas was unable to reach the downstream arms.

We measure temperatures on the exterior walls of the heat pipe oven with an Omega Type K chromel-alumel thermocouple wire connected to an Omega model 650 Type K thermocouple thermometer. When a chromel-alumel junction is made, a potential difference proportional to the temperature is generated and this voltage is measured with the thermometer. The circuit is simple and is easy to troubleshoot, however, problems can be difficult to fix because of the placement of the junction against the heat pipe wall underneath a blanket of insulation and ceramic clam-shell heating elements.

After the last thermocouple stopped working, due to an open circuit, we removed the insulation, heaters, and broken thermocouple wires. We replaced the thermocouples with two Type K thermocouple wires on each arm, 12 in total. Next, we used a thin sheet of malleable ceramic insulation to prevent the thermocouples from making contact with the heaters to avoid a short. Before the insulation could completely dry and set, we attached 6" long cylindrical "clam-shell" heaters of inner diameter 1.625" so that the insulation would mold into shape. Once they were set, we wrapped each arm with half-inch ceramic blanket insulation.

When we fit the gas lines back to the heat pipe with Swagelok connectors and valves, we leak-tested and replaced any faulty connections. We connected two separate, calibrated, millitorr gauges, a Kurt Lesker KJL-6000 thermocouple gauge and a Varian Type 0531 thermocouple gauge, to measure the residual pressure when a dual rotary vane Varian rough pump was used to evacuate the heat pipe system. A pressure reading of less than 30 millitorr is considered to indicate that no significant leaks exist and that the system is sufficiently clean to run the experiment. After reassembly, we were able to pump the system down to 20 millitorr according to both thermocouple type pressure gauges.

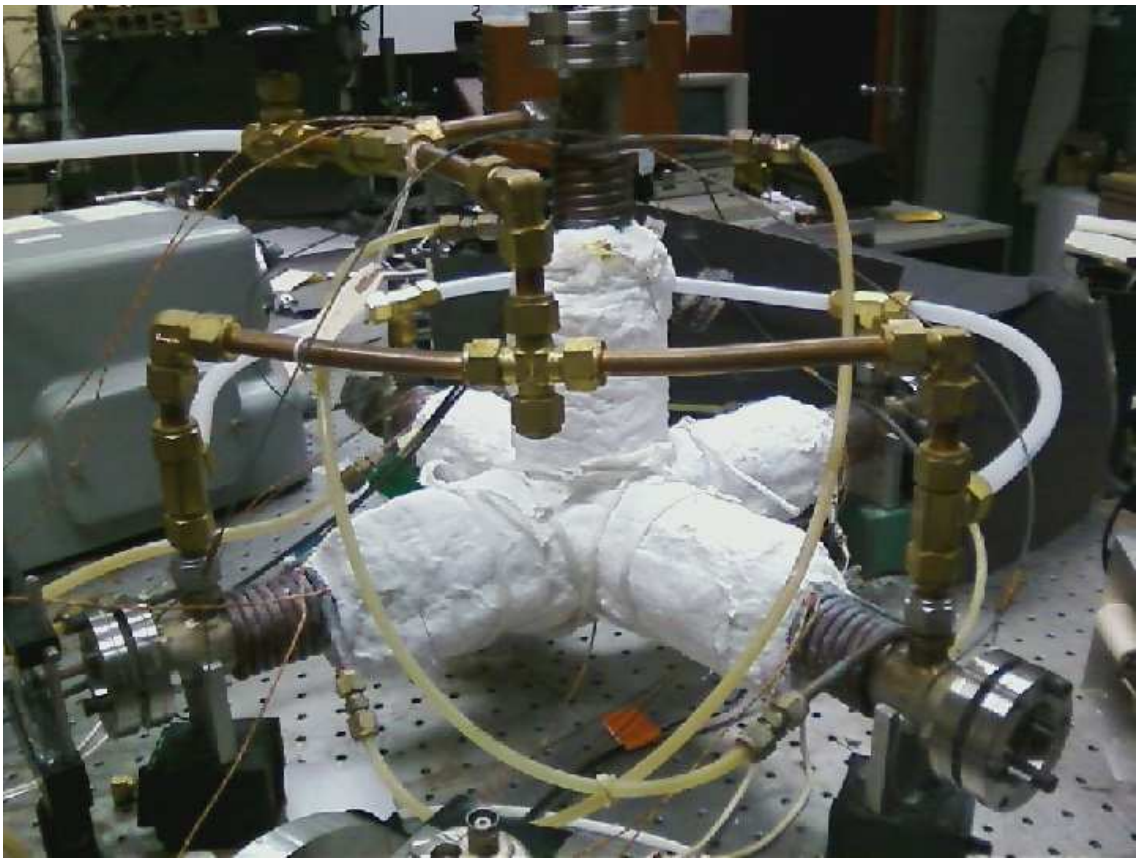

Figure 4.2: A photograph of the heat pipe oven loaded with sodium and potassium for this work. Each arm of the heat pipe is wrapped by a "clam-shell" heater and insulation. Underneath the heaters, there is a total of twelve thermocouple wires. The ends of each arm are capped with BK7 windows held in place by a stainless steel flange. The outer end of each arm is cooled by liquid water carried by copper tubing wrapped around each end. Plastic and copper tubing carries the buffer gas, which makes a whole circuit around the heat pipe oven.

During normal operation, the buffer gas is continuously flowed into the system from a gas bottle. Two valves on the handling system are used to regulate the buffer gas supplied to the heat pipe oven from the tank. Another valve regulates the vacuum pumping on the system and is left slightly open for continuous flow of the buffer gas. Adjustment of these valves allows us to change the buffer gas pressure throughout the day or maintain it as the oven is heated. During the course of the

experiment, gas pressure is measured using an MKS Baratron capacitance manometer located along the gas line connecting the heat pipe oven to the manifold.

4.3 Laser Systems

Two externally pumped, tunable, continuous wave (cw) lasers were used for the collision experiments. Labeled as "dye laser" in Fig. 4.1, a Coherent 699-29 laser utilizing LDS-722 (Pyridine-2) dye as the lasing medium is pumped by 7.90 W from the 514 nm emission of a Coherent Sabre argon ion laser. The dye laser can be frequency tuned from about 12,900 cm^{-1} to 13,800 cm^{-1} with a power output ranging from 125 mW to 400 mW. A Coherent 899-29 titanium sapphire laser labeled "Ti:Sapphire Laser" in Fig. 4.1, is pumped by 10 W of the multiline emission of a Coherent Innova 200 argon ion laser. The Ti:Sapphire laser has a frequency output range from 10,900 cm^{-1} to 12,700 cm^{-1} with a power output between 150 mW and 600 mW. Frequency ranges and power outputs are dependent on the optics set used, quality and stability of the pump laser, and the alignment of the optics within the cavity. An attached wavemeter and the Coherent Autoscan program aid with frequency tuning and data scans for both the Ti:Sapphire and dye lasers.

The Coherent Autoscan program allows the user to record spectra corresponding to the frequency of the laser. Typically we record spectra in 10GHz ($1cm^{-1} \approx 30$GHz) intervals with a 10MHz step size for scans of the Ti:Sapphire laser, or a 25MHz step size for scans of the dye laser. Longer scans can be taken by stacking multiple 10GHz scans. The dye laser acts as the pump and the Ti:Sapphire as the probe laser for NaK when the intermediate state is $A^1\Sigma^+(v = 16, J = 14 \text{ or } 30)$. When the intermediate level is the NaK $A^1\Sigma^+(v = 0, J = 14 \text{ or } 30)$ state and for all the NaCs collision experiments, the roles of the lasers are reversed.

Due to the close spacing of molecular ro-vibrational energy levels, it is important that we use narrow-band, single mode lasers to excite specific transitions. To this end, the dye and Ti:Sapphire laser each have a linewidth of about 750 kHz. The

dye and Ti:Sapphire lasers share very similar optical designs, and full descriptions of each can be found in their respective manuals [48, 49]. A layout of the internal optics of the Ti:Sapphire laser is given in Fig. 4.3 [48, 49].

Tuning to a specific laser frequency involves selecting only one longitudinal mode of the laser cavity. The resonating modes are tuned by a coarse adjustment done with the birefringent filter (BRF), and a fine adjustment of an intracavity etalon assembly. The combination of these components selects a single longitudinal cavity mode capable of enough gain to achieve the lasing threshold. A 10GHz scan is done by slowly rotating a Brewster plate to slightly change the optical path length of the laser cavity, and thus slightly changing the resonating wavelength. To ensure frequency stability, part of the beam is picked off by front and back surfaces of a beam splitter upon exiting the laser cavity. One of the two beams is directed to an external reference cavity, which is a temperature-controlled, confocal interferometer, and then to a detector. The second beam is attenuated and then subtracted from the reference cavity signal. This difference signal is used as feedback for cavity adjustments using a fast response piezo-electric driven "tweeter" mirror, and to adjust the Brewster plate. These adjustments keep the laser locked to a single cavity mode, and frequency stabilized. Additionally, the output beam is split again, and a weak beam is sent to a built-in Coherent wave meter. Because we are interested in relative intensities of lines in the spectra corresponding to transitions that have already been catalogued, we don't use an additional wavelength calibration system for this experiment.

4.4 Detection Systems

Three free-standing photomultiplier tubes (PMT) are used to detect fluorescence and polarization signals. A fourth PMT, attached to the output of the monochromator, is used to record white light absorption spectra. Each of the four PMT's is a Hammatsu model 928 and is contained within a housing. Glass filters at the entrance to each PMT housing restrict the transmitted wavelengths to a desired range. The NaK $2(A)^1\Sigma^+ \rightarrow 1(X)^1\Sigma^+$ fluorescence is detected by the "red PMT" (see Fig. 4.1)

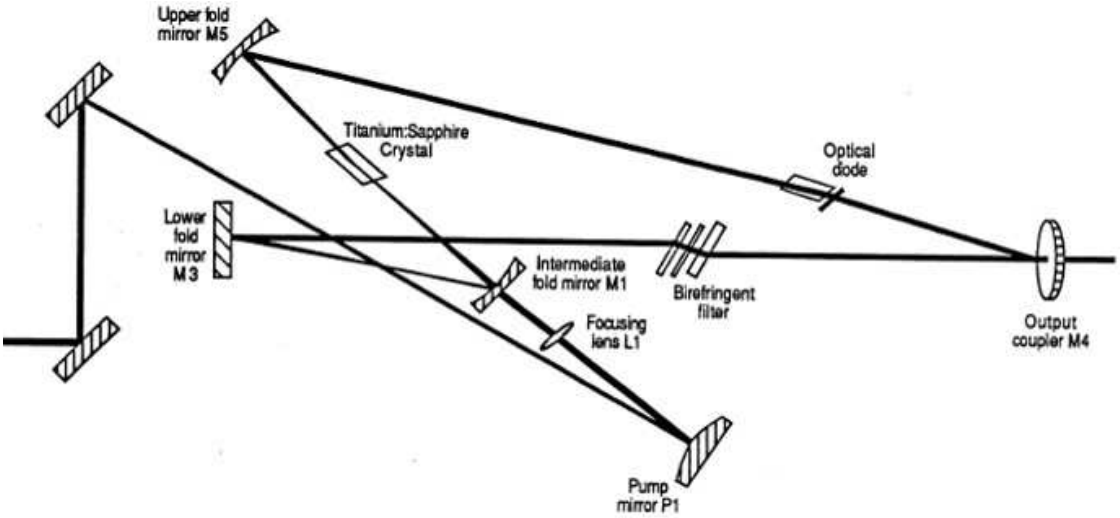

Figure 4.3: Figure reproduced from Coherent Ti:Sapphire manual [49] showing basic optics within the laser cavity.

using a 700 nm long-pass glass filter (Schott RG700). $3^1\Pi \rightarrow 1(X)^1\Sigma^+$ fluorescence is detected by the "violet PMT" using a combination of a 475 nm short-pass filter (Reynard R00905) and a 600 nm short-pass filter (Reynard R00930). The 600 nm short-pass filter is necessary to block out additional longer wavelength light that the 475 nm short pass filter does not block. The polarization PMT, which detects probe laser light transmitted through crossed polarizers placed before and after the heat pipe oven, uses a 780nm long-pass filter (Schott RG780) to filter out scattered dye laser light.

Filters are also used in front of the monochromator entrance slit to filter out background light and light associated with higher orders ($m > 1$) of the grating. The equation governing the diffraction angles of intensity maxima for a diffraction grating is

$$m\lambda = d[\sin(\alpha) + \sin(\beta)], \tag{4.1}$$

where m is the diffraction order, d is the grating spacing (distance between grooves of the grating) and α and β are the incident and diffraction angles, respectively. The grating of the monochromator used in the present work is blazed for 1.0 μm,

which means the grating is most efficient when used near this wavelength in first order, or near half this wavelength in second order. Thus we record potassium white light absorption scans for the lines at 766.7 nm and 770.1 nm in first order and the sodium white light absorption scans for lines at 589.0 nm and 589.6 nm in second order. The monochromator resolution is limited by the slit width and is given by

$$\text{resolution} = \text{reciprocal linear dispersion} \times \text{slit width}\,. \tag{4.2}$$

The MacPherson 0.33 meter monochromator used in this work at Lehigh has a 600 groove/mm grating with reciprocal linear dispersion of 26.5 Å/mm, and the slit width was set to 50 μm, yielding a resolution of 0.13 nm.

Further signal filtering is done electronically with a lock-in amplifier. A mechanical chopper is placed in front of the pump laser beam, and the lock-in amplifier only amplifies signals modulated at the set chopper frequency. Lock-in detection is critical in polarization spectroscopy due to the high background terms from the probe beam (unchopped) caused by imperfect polarizers (ξ), window birefringence ($\Delta\beta$), and window circular dichroism (Δb). An overview of the these background terms and how they are measured is given in Sec. 5.4.2.

4.5 Fourier Transform Spectrometer: Collaborative Work in Lyon

During October of 2012 and November of 2013, our group worked in collaboration with Dr. Amanda J. Ross and Dr. Patrick Crozet at the Université Lyon 1. During the first trip, Carl Faust and I joined the Lyon group to try to locate pump transitions to populate the NaK $2(A)^1\Sigma^+(0, 14)$ level from the ground state. In the following trip, Kara Richter and I worked with Drs. Ross and Crozet to study collisions of argon and helium atoms with NaK molecules prepared in various initial ro-vibrational levels of the $2(A)^1\Sigma^+$state. The main purpose to working in Lyon was to take advantage of the Fourier Transform Spectrometer (FTS) used to record the

data. In Sec. 4.5.1 we describe the heat pipe oven used in Lyon. The design and procedures for loading and controlling this oven are somewhat different from those described previously for the experiment at Lehigh. Section 4.5.2 describes the laser systems used in Lyon and Sec. 4.5.3 describes the FTS and light detectors.

4.5.1 Heat Pipe

The experimental setup in Lyon is similar to the one at Lehigh. In Lyon, we used a linear heat pipe oven lined with stainless steel mesh. Sodium and potassium metal was loaded into the heat pipe oven and, when heated, an alkali vapor forms, surrounded by buffer gas. Outer arms of the oven are cooled, causing the metal to condense onto the mesh wick, and the liquid metal flows back to the central region, as in the crossed heat pipe oven.

There are a few differences between the way the two separate heat pipe ovens are prepared and used. Since the Lyon heat pipe is linear, we cannot detect fluorescence at right angles to beam propagation. Therefore, the beam is sent into the heat pipe through a pierced mirror (see Fig. 4.4). Fluorescence along the axis of the heat pipe is collected by the pierced mirror and focused onto the input aperture of the FTS. To avoid collection of significant amounts of laser scatter, the windows of the heat pipe are oriented at Brewster's angle. This arrangement both reduces total reflection and prevents specular retro-reflection from the windows from reaching the FTS. Additionally, we use long and short-pass filters to block the laser light from entering the FTS whenever possible.

As mentioned previously, we continuously flow inert gas to the Lehigh heat pipe oven at pressures equal to or greater than the alkali vapor pressure, which allows us to adjust the inert gas pressure in the heat pipe over the course of a day's experiment. In contrast, the heat pipe in Lyon is filled with gas in one room and then transported to the room where the experiment is carried out. First the heat pipe oven is evacuated with a vacuum pump at room temperature. The oven is

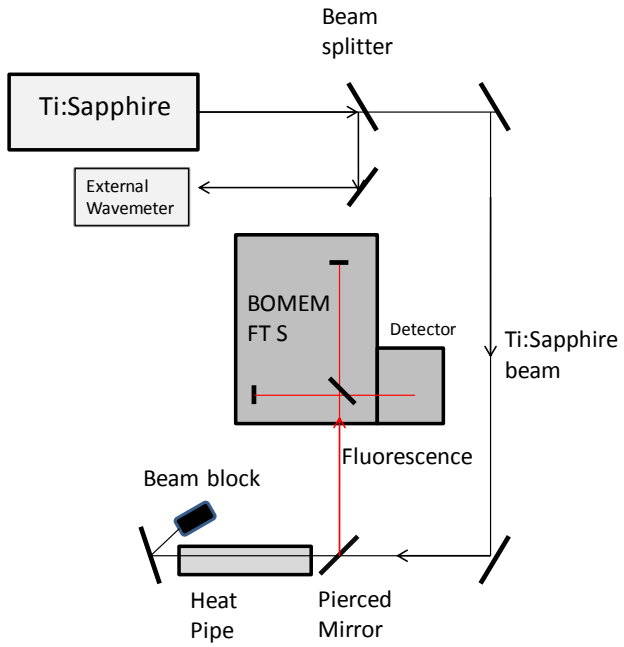

Figure 4.4: Experimental setup in Lyon.

then slowly filled with inert gas to the desired pressure. When set, the heat pipe is sealed for the remainder of the day and carried into the room where the experiment is conducted. The heat pipe oven is heated to the desired temperature, measured by a thermocouple placed against the exterior wall of the oven. The pressure is expected to rise according to the ideal gas law, $PV = Nk_BT$. Assuming there are no significant leaks in the oven, we expect the inert gas number density to remain constant during the experiment.

4.5.2 Laser Systems

The collision experiment run in Lyon involves a single-step excitation, in which we monitor the emission from the pumped ro-vibrational levels in the $2(A)^1\Sigma^+$ state to the ground state. For the excitation, we used a Sirah Matisse TSF Ti:Sapphire laser pumped by 6-8 W of the 532 nm line from a Nd:YVO4 laser. Output powers of the Ti:Sapphire laser are 0.5 W to 1.2 W depending on wavelength. We worked with the mid-range optics set with a tuning range of 740 nm to 880 nm.

4.5.3 Lyon Fourier Transform Spectrometer (FTS) and Light Detection System

Molecular fluorescence is directed from the oven into a Bomem Fourier transform interferometer through an iris. As shown in Fig. 4.5, light enters the FTS on the right side ("emission beam input"). Inside the FTS, the light is first collimated and then sent to a 50/50 beam splitter. Half of the fluorescence is directed along an arm with a motor-controlled translating mirror used to change the path length of the light in this arm of the interferometer. The other half is sent along a fixed path to another mirror. After traveling along the two separate arms and being retro-reflected, the light is recombined, where each frequency component interferes constructively or destructively depending on the optical path difference. The recombined light is directed to one of two detectors, which can be selected by rotating a flat mirror. We used either a silicon avalanche or an Indium-Gallium-Arsenide (InGaAs) detector, depending on the wavelength range of interest for a particular experiment. The silicon avalanche detector is used for shorter wavelengths (less than 1000 nm), and the Indium-Gallium-Arsenide (InGaAs) detector is used for longer wavelengths, further in the infrared. The choice of detector is made by the orientation of the "output beam selection mirror" (see Fig. 4.5). To reduce thermal background (dark current), the detectors are cooled by liquid air.

A raw scan of the fluorescence is in the form of an interferogram, such as the one shown in Fig. 4.6. The power of the interferogram is that although it can't be

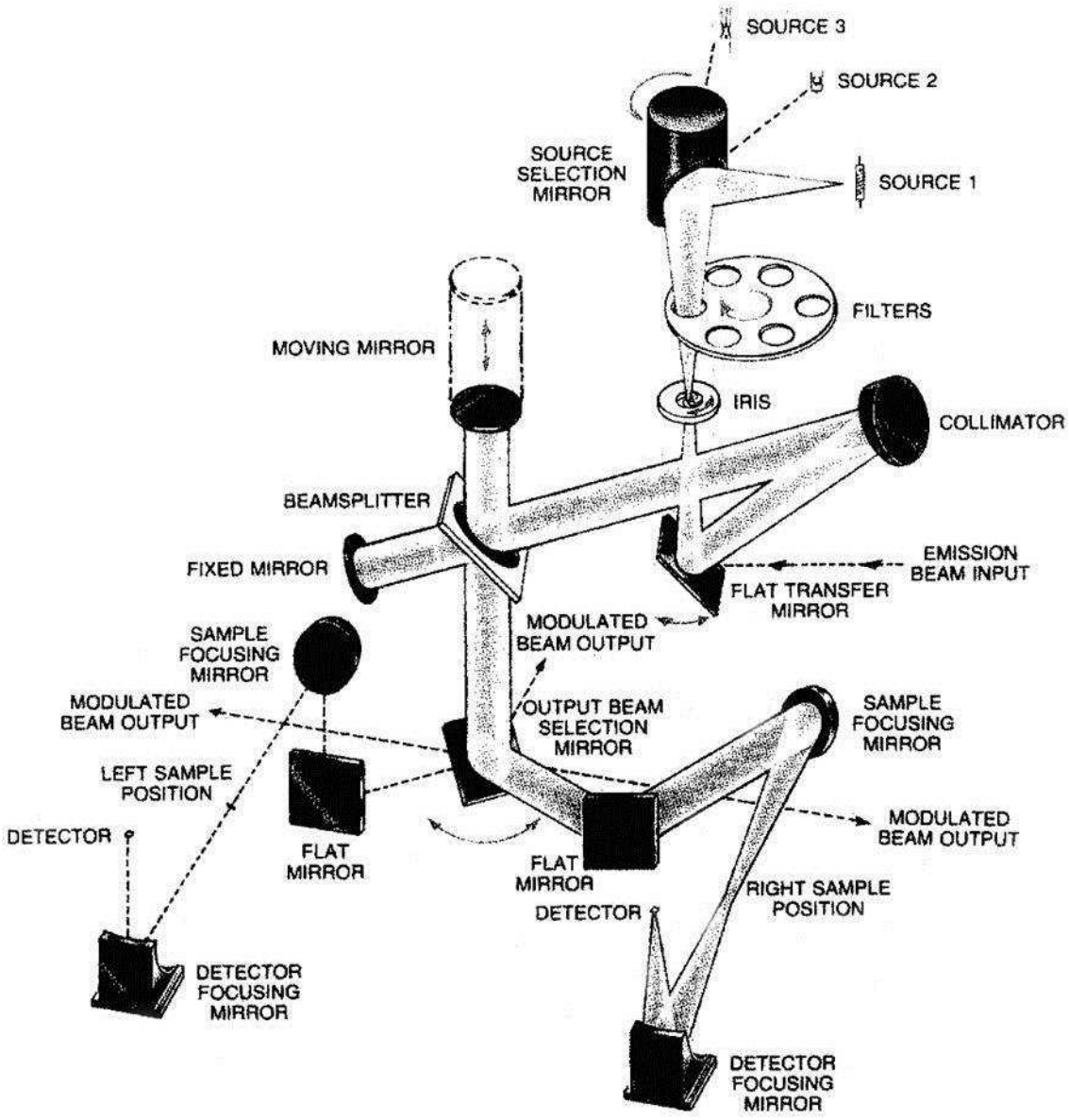

Figure 4.5: Schematic illustration of the Fourier transform spectrometer similar to the one used in Lyon, France. Figure reproduced from Bomem Training Manual [50].

interpreted by eye in this form, a Fourier transform of the interferogram produces a high resolution, analyzable spectrum (Fig. 4.6). The Bomem FTS used in Lyon has

several resolution options. The further the movable mirror is allowed to travel, the better the resolution, but at the cost of longer scan times. For low light intensities, the FTS can be run for longer time periods to accumulate more data. One big advantage for collision experiments is that the fluorescence signals for the direct and collisional lines are acquired simultaneously. Therefore, the intensities scale with each other, as fluorescence is acquired so the relative intensities are constant, even if the laser frequency drifts slightly. In contrast, the direct and collisional line data taken at Lehigh are recorded sequentially. As a consequence, in the latter case, we repeat the scan of the probe laser frequency over the direct transition after recording the collisional lines to verify that no drift has occurred. The data sequence must be repeated if the "before" and "after" direct line intensities differ by more than five percent.

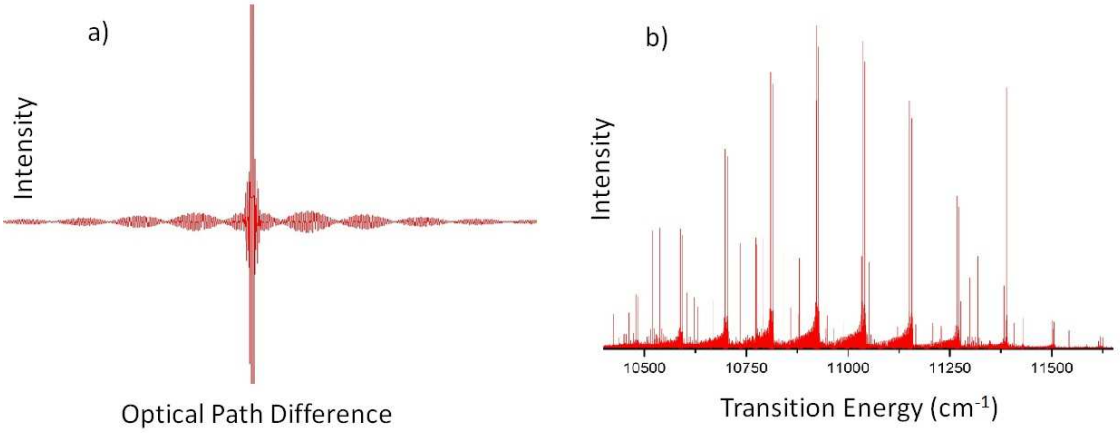

Figure 4.6: a) An example of the pre-processed interferogram generated by the FTS from NaK fluorescence. b) After a Fourier transform of the interferogram in (a), the result is a spectrum like that seen in (b). There are many peaks in the spectrum. The process of analyzing them is addressed in chapter 6.

Chapter 5

Experimental Techniques

5.1 Overview

I begin this chapter with a discussion (Sec. 5.2) of how we predict and experimentally determine alkali densities. Section 5.2.1 discusses the estimation of densities from vapor pressure formulas. The discussion in Sec. 5.2.2 addresses the daily white light absorption measurements taken to determine densities. The following section (Sec. 5.2.3) describes the use of laser absorption as a check to white light measurements. Section 5.2.4 includes a comparison of results from the methods of potassium density measurement using the equivalent width method and laser line absorption method.

In Sec. 5.3, I discuss the methods by which we excite the molecules utilizing tunable lasers. The technique of optical-optical double resonance is discussed in Sec. 5.3.1, and I describe how this technique is used to observe collisions of diatomic alkali molcules. Section 5.3.2 presents a related technique called perturbation facilitated optical-optical double resonance. Section 5.4 describes the polarization labeling technique, and how it is used to study collisional transfer of orientation. I also address the issues of background noise and how we measure and minimize the noise effects on polarization signals.

5.2 Determining Atomic and Molecular Alkali Densities

5.2.1 The Nesmeyanov Vapor Pressure Formulas

The alkali vapor density is roughly controlled by adjusting the power supplied to the heating elements attached to the outer surface of the heat pipe oven. There are several methods by which we can determine the alkali vapor pressures. The simplest method is to obtain an initial estimate of the sodium, potassium, or cesium density from a vapor pressure formula and the temperature of the heat pipe oven. Although a number of authors have published vapor pressure formulas for the alkalis, Nesmeyanov [51] created a critical compilation of all data for each of the elements available at the time his book was published in 1963. For each atomic and molecular species, Nesmeyanov produced a "best" vapor pressure formula of the general form

$$\log_{10} P = A - \frac{B}{T} + CT + D\log_{10} T. \tag{5.1}$$

The coefficients A, B, C, and D given by Nesmeyanov for substances important to the present work are listed in Table 5.1. Using the Nesmeyanov parameters for a particular atomic or molecular alkali species with the measured absolute temperature, T, of the heat pipe oven, we can then estimate a partial pressure, P, for that species.

The result from the Nesmeyanov vapor pressure prediction is used to determine the atomic or molecular number density via the ideal gas law,

$$n = \frac{N}{V} = \frac{P}{k_B T}, \tag{5.2}$$

where n is the atomic or molecular number density and k_B is Boltzmann's constant. Use of the Nesmeyanov vapor pressure formula, or any other vapor pressure formula, assumes that the sample consists purely of one atomic or molecular species. This assumption is not the case in our work because we vaporize an amalgam of two alkali species. Dalton's law (discussed in Ref. [52]) states that the total pressure of

Species	A	B	C	D
Na	10.86423	5619.406	-0.00000345	-1.04111
Na_2	5.33624	6866.162	-0.00106668	1.23023
K	13.83624	4857.902	0.00034940	-2.21542
K_2	17.05231	6806.144	0.00012351	-2.98966
Cs	8.22127	4006.048	-0.0006019	-0.19623
Cs_2	18.22054	6064.472	0.00009016	-3.45395

Table 5.1: Nesmeyanov vapor pressure coefficients for Na, K, Cs and their dimers.

the system is given by a sum of the partial pressures of each species in the vapor,

$$P_{total} = P_a + P_b + \dots , \tag{5.3}$$

where P_i is the partial pressure of species i at the oven temperature. Raoult's law states $P_i = P_i^* x_i$ where P_i^* is the vapor pressure of the pure component "i" and x_i is the mole fraction of that species. Using Raoult's law in conjunction with Dalton's law yields

$$P_{total} = P_a^* x_a + P_b^* x_b + \dots , \tag{5.4}$$

where the partial pressure of each species is dependent on the relative amount of that species within the oven. However, Raoult's law is known to have only limited validity. In our work, we find use of Raoult's law and the Nesmeyanov vapor pressure formula lead to a systematic under-estimation of the actual vapor pressure.

5.2.2 White Light Absorption and Equivalent Width

The Nesmeyanov vapor pressure formulas have the benefit of serving as a simple method to generate an initial prediction of the alkali atomic and dimer densities. However, use of these formulas does not constitute an actual measurement of pressure or density.

We can determine the atomic densities spectroscopically by the method of equivalent width from an absorption spectrum. Following the discussion in Ref. [53], we define the equivalent width of the spectral line as:

$$W_\nu = \int \left(1 - \frac{I_\nu(L)}{I_\nu(0)}\right) \mathrm{d}\nu = \int (1 - \mathrm{e}^{-k_\nu L}) \mathrm{d}\nu, \tag{5.5}$$

where W_ν is the equivalent width in frequency units, k_ν is the absorption coefficient at frequency ν, L is the length of the column of absorbing particles, and $I_\nu(0)$ and $I_\nu(L)$ describe, respectively, the incident and transmitted intensities of the light at frequency ν. The equivalent width, W_ν, is the width (in frequency units) of a rectangle whose height is $I_\nu(0)$ and whose area is the same as that of the spectral line of interest (see Fig. 5.1). Since we record the spectra in units of wavelength, the conversion of the equivalent width from frequency units to wavelength units is

$$W_\lambda = \frac{\lambda_0^2}{c} W_\nu, \tag{5.6}$$

where λ_0 is the line center wavelength of the transition and c is the speed of light.

To calculate an equivalent width, the absorption lineshape must be known. For alkali resonance transitions, a huge number of studies (see Ref. [54]) have shown that a convolution of Lorentzian and Gaussian lineshapes, called a Voigt profile, can be used to describe the lineshape k_ν accurately,

$$k_\nu = \frac{\lambda_0^2 n A_{21}}{8\pi} \frac{g_2}{g_1} \int \mathscr{G}(\nu' - \nu_0) \mathscr{L}(\nu - \nu') d\nu' \,. \tag{5.7}$$

Here, A_{21} is the transition Einstein A coefficient and g_2 and g_1 are the statistical weights of the upper and lower levels, respectively. The terms $\mathscr{G}(\nu' - \nu_0)$ and $\mathscr{L}(\nu - \nu')$ describe the normalized Gaussian and Lorentzian functions that make up the Voigt profile. The Lorentzian contribution to the lineshape (normalized with respect to $d\nu$) is given by the function,

$$\mathscr{L}(\nu - \nu_0) = \frac{\Gamma}{4\pi^2(\nu - \nu_0)^2 + \frac{\Gamma^2}{4}} \tag{5.8}$$

where $\frac{\Gamma}{2\pi}$ is the full width at half maximum (FWHM) of the line (in Hz), and $\nu - \nu_0$ is the detuning from linecenter, ν_0. Information about the homogeneous line broadening mechanisms, such as natural and collisional broadening, is contained within

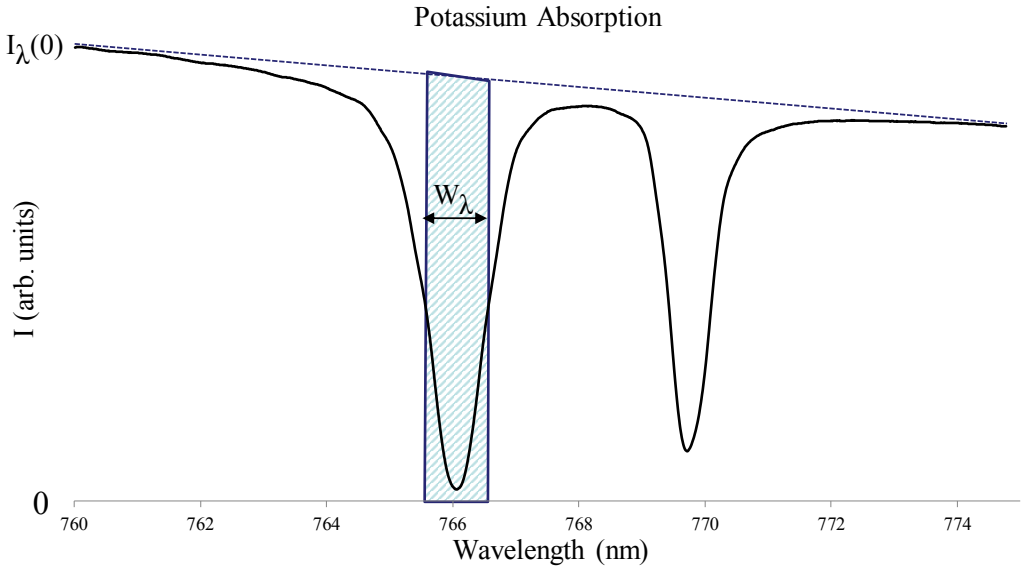

Figure 5.1: A potassium resonance line white light absorption spectrum demonstrating the concept of equivalent width. To obtain the equivalent width, a box of width W_λ and height $I_\lambda(0)$ preserving the area of the spectral line is constructed. From W_λ one can determine the atomic potassium number density.

the Lorentzian lineshape. The normalized Gaussian contribution to the lineshape is described by

$$\mathscr{G}(\nu-\nu_0) = \sqrt{\frac{mc^2}{2\pi k_B T \nu_0^2}}\, \mathrm{e}^{\frac{-mc^2(\nu-\nu_0)^2}{2k_B T \nu_0^2}}, \tag{5.9}$$

where the mass of the atom or molecule, m, and the temperature, T, are the only newly introduced parameters. Doppler effects, due to the thermal motion of particles with a Maxwell-Boltzmann velocity distribution, are taken into account using a Gaussian lineshape.

The Voigt profile must be calculated numerically because the Voigt profile has no closed-form solution. To carry out this calculation, we have developed a short Fortran program with the help of a Voigt subroutine [55, 56]. The subroutine has a distinct accuracy and time advantage over a simple trapezoidal rule integration

method. Our equivalent width Fortran program calculates W_λ for sodium or potassium resonance lines with a given type of buffer gas and pressure, and a given sodium or potassium density.

To determine the density experimentally, we take a white light absorption measurement using a calibrated tungsten halogen source, and directing it through the alkali vapor in the heat pipe oven and to a monochromator/photomultiplier system. The monochromator/photomultiplier can record light intensity versus wavelength over a large wavelength range by rotating the monochromator grating. For our equivalent width measurements, we scan the monochromator over a strong, well known resonance transition of the alkali atom of interest. The white light source is mechanically chopped and raw data are collected using a lock-in amplifier and recorded using LabView (Ver. 2011). The raw data scan is imported into Origin (Ver. 7.5) and an equivalent width, in wavelength units, is determined by integrating the area of the absorption line with respect to the baseline, $I_\lambda(0)$. Finally, to obtain an experimental value for the atom density, we iteratively adjust the atomic alkali density in the equivalent width computer code until the calculated equivalent width matches the experimental equivalent width.

Despite the limited resolution of the monochromator, the area of any spectral line is independent of the resolution as we show below. As stated earlier, the equivalent width is defined to be the integral of the normalized absorption $[I_\nu(0) - I_\nu(L)]/I_\nu(0) = 1 - T(\nu)$ (where $T(\nu)$ is the transmittance at frequency ν). Therefore, we can consider the apparent equivalent width measured with a monochromator of finite resolution to be a convolution of the true lineshape transmittance, $T(\nu')$, with the normalized monochromator instrument function, $m(\nu-\nu')$,

$$W_\nu = \int \mathrm{d}\nu \int \mathrm{d}\nu' \, [1 - T(\nu')] \, m(\nu - \nu') \, . \tag{5.10}$$

Here, $m(\nu - \nu')$ represents the amount of light of frequency ν' that passes through the monochromator exit slit when the monochromator is set to frequency ν. Now,

we rearrange the integration to

$$W = \int [1 - T(\nu')] \left[\int m(\nu - \nu') \mathrm{d}\nu \right] \mathrm{d}\nu'$$
$$= \int [1 - T(\nu')] \, \mathrm{d}\nu', \tag{5.11}$$

where we used the fact that

$$\int m(\nu - \nu') \mathrm{d}\nu = 1. \tag{5.12}$$

Therefore, we have shown that the equivalent width is independent of the monochromator resolution. It is advantageous to choose the monochromator slit widths (which control the resolution) so that they are not too wide (which leads to broad, flat absorption dips that are extremely sensitive to baseline errors) and not too narrow (which leads to low throughput and hence low signal to noise).

5.2.3 Laser Absorption in the Line Wing

Having a second experimental method for determining the alkali density is beneficial as a check of the white light equivalent width method. The line wing absorption measurement is based on a measurement of the fraction of laser intensity absorbed at a specific detuning from line center. To avoid saturation effects, a highly attenuated laser beam (on the order of microWatts) is required for this measurement. We cannot examine line wing absorption using the white light source and monochromator due to the limited monochromator resolution. However, our single mode dye and Ti:Sapphire lasers provide light of very narrow linewidth (about 750 kHz), while the atomic lines are typically 1 GHz wide.

Now, instead of measuring the entire integral under the absorption line, we can instead determine

$$\frac{I_\nu(L)}{I_\nu(0)} = \mathrm{e}^{-k_\nu L} \tag{5.13}$$

for a single known frequency ν. If the absorption measurement is taken far enough in the wings of the line, the lineshape k_ν can be well described by a single Lorentzian

function. This is because the Gaussian wings drop off much faster than the Lorentzian wings. The absorption coefficient can be calculated from

$$k_\nu = \frac{\lambda_0^2 n A_{21}}{8\pi} \frac{g_2}{g_1} \frac{\Gamma}{4\pi^2(\nu-\nu_0)^2 + (\frac{\Gamma}{2})^2} = \frac{1}{L} \ln\left(\frac{I_\nu(0)}{I_\nu(L)}\right). \tag{5.14}$$

Assuming the Lorentzian (homogeneous) linewidth Γ, the Einstein A coefficient, and the detuning from line center $(\nu - \nu_0)$ are all known, the atom density n can be determined from the transmitted intensity. Of course the linewidth and A coefficient are also needed to determine density from equivalent width. The parameter Γ includes information from all homogeneous lineshape contributions. In our situation, we consider natural broadening and collisional (pressure) broadening,

$$\Gamma = \Gamma_{nat} + k_{alk}^{br} n_{alk} + k_{buf}^{br} n_{buf}. \tag{5.15}$$

The contribution to the Lorentzian linewidth due to natural lifetime broadening is given by $\Gamma_{nat} = A_{21}$. Collisional broadening rates due to the free alkali atoms and the buffer gas atoms are expressed in terms of a broadening rate coefficient for perturber X, k_X^{br}, multiplied by the perturber density, n_X. Values of $\Gamma_{nat} = A_{21}$, k_K^{br}, k_{Ar}^{br}, and k_{He}^{br} for the potassium resonance lines $4S_{1/2} \rightarrow 4P_{1/2}$ (D1) and $4S_{1/2} \rightarrow 4P_{3/2}$ (D2) used in this work are taken from the literature and are listed in Table 5.2. Values for the sodium resonance lines $3S_{1/2} \rightarrow 3P_{1/2,3/2}$ and the cesium resonance lines $6S_{1/2} \rightarrow 6P_{1/2}$ are also given.

5.2.4 Experimental Density Measurements

As mentioned in Sec. 5.2.2, we routinely take white light absorption measurements to determine the alkali density. On occasion, we also take laser line absorption measurements to confirm the accuracy of the equivalent width method using the potassium D2 transition. The strong atomic transitions of sodium are not accessible within the frequency ranges of our lasers. In Table 5.3, we compare measured potassium densities obtained with the white light equivalent width method and with laser

Alkali	k_{Ar}^{br} ($\mathrm{cm^3 s^{-1}}$)	k_{He}^{br} ($\mathrm{cm^3 s^{-1}}$)	k_{self}^{br} ($\mathrm{cm^3 s^{-1}}$)
Na (D1)	2.77×10^{-9} [57]	1.90×10^{-9} [57]	3.07×10^{-7} [58]
Na (D2)	2.27×10^{-9} [57]	2.19×10^{-9} [57]	4.67×10^{-7} [58]
K (D1)	2.45×10^{-9} [59]	1.55×10^{-9} [59]	3.92×10^{-7} [60]
K (D2)	1.98×10^{-9} [59]	2.06×10^{-9} [59]	6.38×10^{-7} [60]
Cs (D1)	3.79×10^{-9} [61]	3.67×10^{-9} [61]	5.7×10^{-7} [62]
Cs (D2)	4.38×10^{-9} [61]	5.13×10^{-9} [61]	6.7×10^{-7} [62]

Table 5.2: Broadening rates for atomic lines used in equivalent width measurements. For each alkali atom, the corresponding perturber and broadening rate coefficient is given for the strong D1 and D2 transitions.

line wing absorption. These values agree well within our conservative 30% error bars assigned to the potassium density. The results of 11/4/2013 were obtained by Kara Richter and myself working in our collaborator's lab in Lyon, France with their heat pipe oven. In that case, the "equivalent width" density wasn't determined using the equivalent width method, but rather from wing absorption using the Bomem FTS with a white light source and a resolution of $1.0\,\mathrm{cm^{-1}}$ (corresponding to about 0.03 nm). Thus, this analysis of white light absorption was, in principle, similar to the method of laser line wing absorption (see Sec. 5.2.3). Here we chose specific points along the absorption curve (in the line wings) and compared them to a white light spectrum obtained with a cold heat pipe ($n_K = 0$). The absorption dip is fairly wide (on the order of 1 nm), and the absorption doesn't change quickly in the wings. Therefore, the resolution of the Bomem FTS is sufficient to obtain reliable values for the frequency-dependent absorption coefficient. In contrast, such measurements are not possible with the monochromator at Lehigh due its limited resolution (0.13 nm). This limited resolution produces significant distortion in the line wings.

Date/Density (K)	Laser ($\times 10^{15}$ cm^{-3})	Eq. Width ($\times 10^{15}$ cm^{-3})
1/29/2013	1.84	1.85
7/11/2013	1.83	1.78
10/21/2013	1.48	1.30
11/4/2013	1.94	2.06*
1/14/2014	3.43	3.80

Table 5.3: Table comparing potassium densities determined from the laser line wing absorption method and the white light equivalent width method. The "equivalent width" data from Lyon, marked with an asterisk, make use of high resolution FTS white light absorption to determine the density from the wings of the absorption line. The results indicate that the density measurements using either of these different methods agree well within the assumed 30% error bars and serve as a check of the consistency of our density measurements.

5.3 Excitation Methods

5.3.1 Optical-Optical Double Resonance (OODR)

We use a two-step excitation scheme called optical-optical double resonance (OODR) to excite the diatomic alkali molecules using counter-propagating beams from the dye laser and the Ti:Sapphire laser. The pump laser excites the molecules from ro-vibrational levels of the ground state, $1(X)^1\Sigma^+$, to ro-vibrational levels of the intermediate state, $2(A)^1\Sigma^+$. Total red fluorescence, corresponding to transitions from the intermediate state back down to the ground state, as shown in Fig. 5.2.a, emitted in a direction perpendicular to the laser propagation axis, is collected with a lens and detected by the red PMT (see Fig. 4.1) as the pump laser frequency is scanned. The pump laser frequency is then set to a particular peak, corresponding to a specific transition $2(A)^1\Sigma^+(v', J') \leftarrow 1(X)^1\Sigma^+(v'', J'' = J' \pm 1)$ and we scan the probe laser frequency across transitions from the specific ro-vibrational level $2(A)^1\Sigma^+(v', J')$ populated by the pump laser to various levels $3^1\Pi(v, J = J', J' \pm 1)$ of the upper $3^1\Pi$ state in NaK. Three direct lines, P, Q, and R are observed, obeying selection rules $J_{upper} - J_{lower} = -1, 0, 1$, respectively. Changing J by zero is not allowed in $\Sigma \rightarrow \Sigma$ transitions, but is allowed for $\Sigma \rightarrow \Pi$ transitions. Fluorescence

from the $3^1\Pi$ to the ground state, as shown in Fig. 5.2.(b), is monitored by the violet PMT (see Fig. 4.1).

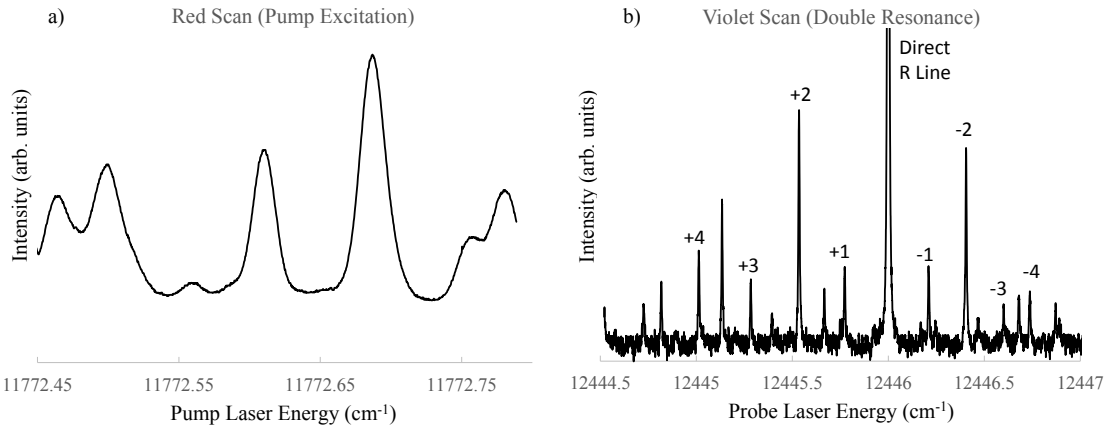

Figure 5.2: Fluorescence signals produced in an OODR experiment. Figure a) shows an example of NaCs A band fluorescence observed while scanning the pump laser over transitions to the A state from the ground state. b) shows an example of NaK collisional relaxation that occurs in the intermediate (A) state, recorded using the total violet PMT as the probe laser frequency is scanned. The direct line goes far off scale, and the associated collisional lines are labeled by the change in rotational state (ΔJ) value from the initial direct line. Lines that are not labeled are collisional progressions corresponding to a nearby direct line.

The vibrational quantum number can change by any value in an electronic transition, with certain transitions being stronger or weaker based on the Franck-Condon factors (FCF's) associated with the two ro-vibrational levels involved in the transition. We have chosen transitions with large FCF's for the experiments reported here by calculating FCF's using the program LEVEL by R. J. Le Roy [40]. We detect pump and probe laser excitation by monitoring total fluorescence corresponding to downward transitions from both the upper state, $3^1\Pi(v, J)$, and the intermediate

state, $2(A)^1\Sigma^+(v', J')$, to the ground state, $1(X)^1\Sigma^+$. Total fluorescence from the intermediate state is detected by the red PMT and the fluorescence from the upper state is detected by the violet PMT for NaK (see Fig. 4.1). Figure 5.3 shows a schematic of OODR excitation of direct P, Q, and R transitions and of collisional lines as observed in a typical excitation scan.

Flanking either side of the direct lines in the total violet fluorescence scan of the probe laser frequency, are much smaller peaks spaced at predictable intervals (assuming no significant perturbations). Some of these peaks can be observed in Fig. 5.2b. These peaks are the result of inelastic collisions that transfer some population to nearby intermediate state $2(A)^1\Sigma^+$ rotational levels from the level directly populated by the pump laser. With the pump laser frequency fixed on an $A \leftarrow X$ transition, the probe laser frequency is scanned, exciting the collisionally populated rotational levels $2(A)^1\Sigma^+(v', J' + \Delta J)$ to the $3^1\Pi$ state. The ΔJ is an integer value describing the change in the rotational quantum number during the collision. For our conditions, the intensities of these collisionally populated lines are typically about five to ten percent of the intensity of the direct lines.

Unlike the collision experiment conducted at Lehigh, the experiment in Lyon was a single-step excitation experiment. We used the Matisse Ti:Sapphire laser to excite a particular transition from one ro-vibrational level of the ground state to a ro-vibrational level of the $2(A)^1\Sigma^+$state. At Lehigh we monitor the total fluorescence due to all possible transitions from the upper state ($3^1\Pi$) to the ground state. In Lyon, the laser is fixed to the line center frequency of a transition and the total fluorescence from the $2(A)^1\Sigma^+$state is sent into the FTS. When a Fourier transform of the interferogram is processed, all the various transitions from the directly excited and collisionally populated levels of the upper state $[2(A)^1\Sigma^+]$ to various ro-vibrational levels of the ground state are recorded. In the Lyon spectra, the strong pairs of lines are due to the $\Delta J = \pm 1$ selection rule for $\Sigma \rightarrow \Sigma$ transitions (P and R lines). There are multiple pairs of lines observed due to the transitions to all possible v'' levels of the ground state. These strong pairs of lines are all labeled as "direct" lines (see Fig. 5.4(a)). The spectral lines flanking the base of each direct

line are due to rotationally inelastic (J-changing) collisions (see Fig. 5.4(b)).

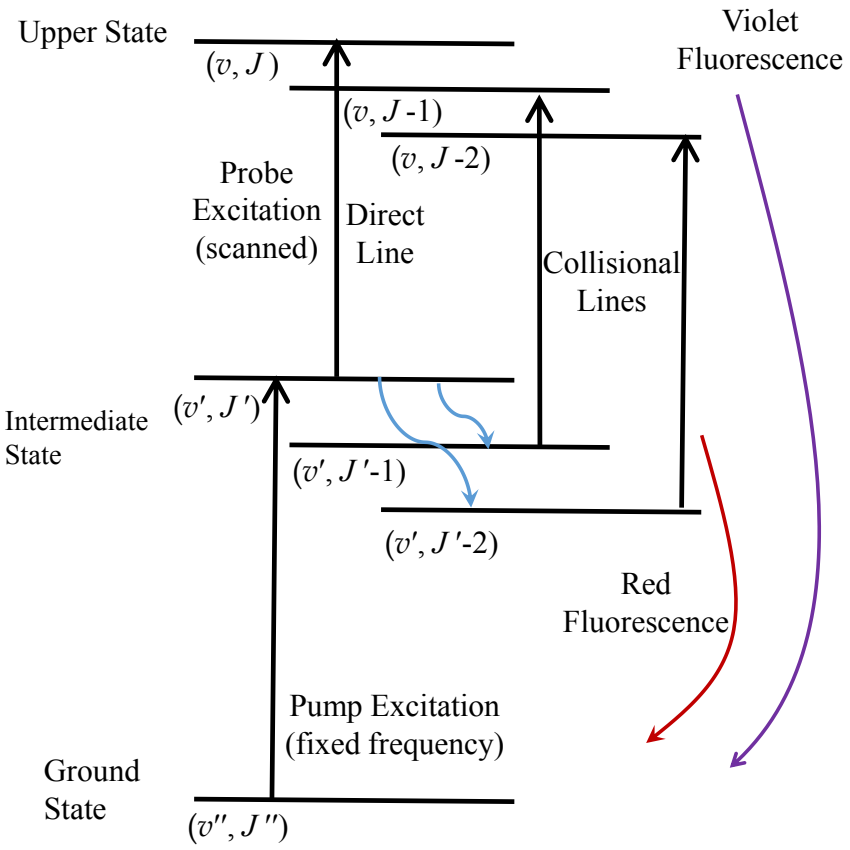

Figure 5.3: OODR excitation scheme. The pump laser frequency is fixed to excite a specific transition from the ground state to the intermediate state and the frequency of the probe is scanned. Total fluorescence is monitored for transitions from both the intermediate state and the upper state back down to the ground state. We observe direct lines corresponding to probe laser excitation of the level directly populated by the pump laser, as well as collisional lines, corresponding to intermediate state levels populated via collisions from the directly excited level. The ro-vibrational levels within a given state are close in energy and the fluorescence from the direct line and collisional lines is detected using the same filters.

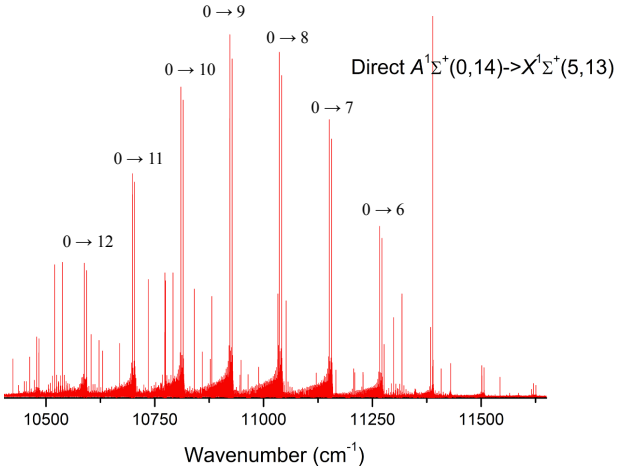

(a) Fluorescence from $2(A)^1\Sigma^+ \leftarrow X^1\Sigma^+$ transitions.

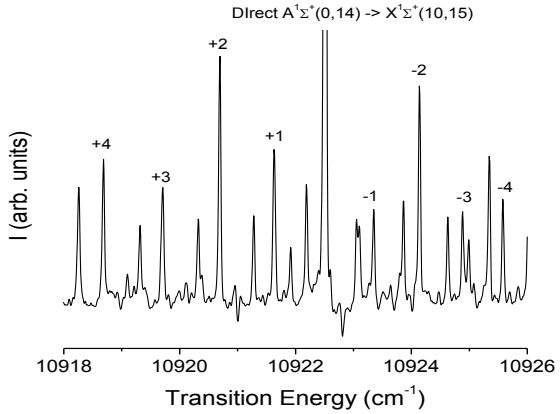

(b) Expanded view showing collisional relaxation.

Figure 5.4: Spectra taken during the Lyon experiment illustrating fluorescence associated with transitions from the $2(A)^1\Sigma^+$state to ground state. Figure (a) shows the fluorescence corresponding to pairs of direct lines representing transitions from the directly populated A state level $[2(A)^1\Sigma^+(v', J')]$ to various vibrational levels v'' of the ground state $[1(X)^1\Sigma^+(v'', J'')]$. Figure (b) is a zoomed-in section of the spectrum in (a) showing the weak lines resulting from rotationally inelastic collisions. The direct line is going far off scale in (b).

5.3.2 Perturbation Facilitated Optical-Optical Double Resonance (PFOODR)

It is possible to reach a triplet upper state by means of window levels. In the case of OODR, we assume pure singlet and pure triplet states, for which the spin quantum number cannot change during a transition (selection rule $\Delta S = 0$). It is possible to circumvent this selection rule to access upper triplet levels by utilizing perturbations between levels of two electronic states of different spin character. The interaction creates mixed levels, which can be described as having both a singlet and triplet character. In the alkali molecules, the most important mixing occurs between the $2(A)^1\Sigma^+$and $b^3\Pi$ states due to spin-orbit coupling. Nearly degenerate levels of the two states, with the same J, are coupled together to form mixed levels given by

$$|\Psi\rangle = a_s|2(A)^1\Sigma^+(v_A, J')\rangle + a_t|b^3\Pi(v_b, J')\rangle\,, \tag{5.16}$$

where the a_s and a_t coefficients describe the singlet and triplet amplitudes of the mixed level and $a_s^2 + a_t^2 = 1$. Such mixed $2(A)^1\Sigma^+ \sim b^3\Pi$ levels are called "window" levels because they allow access to the otherwise "dark" triplet states from the singlet ground state.

Previous work in our group used the perturbation facilitated optical-optical resonance (PFOODR) technique to map out various high lying triplet states of NaK and the $5^3\Pi_{0^+}$ state of NaCs with good coverage in the frequency ranges of our lasers [9]. In this technique, the molecules are excited to mixed $1(b)^3\Pi_{0^+}(v_b, J') \sim 2(A)^1\Sigma^+(v_A, J')$ levels from the $1(X)^1\Sigma^+(v'', J'')$ ground state with the pump laser. The transition ${}^3\Lambda(v, J) \leftarrow 1(b)^3\Pi_{0^+}(v_b, J') \sim 2(A)^1\Sigma^+(v_A, J')$ is then excited with the probe laser. PFOODR excitation of the NaCs $5^3\Pi_{0^+}$ state is used in the current work to study collisional population transfer between mixed $1(b)^3\Pi_{0^+} \sim 2(A)^1\Sigma^+$ levels of this molecule (see Chapter 6).

5.4 Polarization Labeling Spectroscopy

5.4.1 Polarization Spectroscopy

Polarization labeling spectroscopy is an OODR technique in which changes in the complex index of refraction induced by a pump laser tuned to an atomic or molecular transition frequency are detected. The probe beam passes through a pair of crossed polarizers (see Fig. 4.1) placed outside the heat pipe oven windows on opposite ends of the oven. If the pump beam is tuned off the relevant transitions, then the probe beam intensity will be completely blocked by the second polarizer (analyzer). However, if the pump and probe lasers are both tuned to transitions involving a common level, then the probe sees an optically anisotropic medium and its polarization is modified. Thus, some small fraction of the probe light is able to pass through the analyzer. Because the probe beam is directed straight into the PMT, even a very small transmission of the probe beam through the analyzer results in an enormous signal. Therefore it is necessary to cut the probe power down to 1 mW to 2 mW to prevent overloading the PMT. Too much probe beam power can also cause saturation of the M_J sublevels, destroying orientation in the intermediate level, which is necessary for polarization signal.

To establish an orientation in the intermediate level we use a Fresnel rhomb to create the circular polarized pump beam needed to preferentially populate some M_J levels (see Fig. 3.2). The pump beam enters the rhomb perpendicular to the first face, is internally reflected twice, then exits perpendicular to the last face traveling in the original direction, but horizontally and vertically displaced. When the rhomb is properly oriented with respect to the vertical polarization of the laser beam, one component of the beam experiences a 45° phase shift at each of the two internal reflections and the beam exits the rhomb circularly polarized. The transmitted polarization has been measured to be circular to within about ten percent. The remaining linear polarization doesn't pose a problem because it creates no orientation. Since the dye and titanium sapphire lasers are tunable, it is important to have a circular polarizer that is achromatic over a wide range of wavelengths.

The polarization of the counter propagating probe beam is first improved with a linear polarizer before the beam enters the heat pipe oven. This step is necessary because the polarization of the beam is slightly degraded as it passes through lenses and reflects from mirrors between the laser and the heat pipe oven. The linearly polarized probe beam can also be described as equal parts left and right circular polarization (quantization axis is then considered to be along the laser propagation axis). As the circular components of the probe beam interact with the alkali vapor, they experience an unequal absorption and/or refraction due to the interactions with the oriented molecules (unequal populations in the intermediate state M_J levels) when on resonance with a transition.

Once the probe beam exits the heat pipe, it passes by (but does not hit) a D-shaped mirror that directs the pump beam into the heat pipe (see Fig. 4.1). There is a slight crossing angle between the two beams, so a long path length is needed to separate only the probe beam for detection. After the D-shaped mirror, the probe beam travels to the polarizer (analyzer), which is oriented at $\sim 90^\circ$ with respect to the first polarizer. Due to the slight change in probe beam polarization acquired during its transit of the oven, some of the light reaches the detector as signal.

In order to observe a polarization signal, there must be a net orientation created in the intermediate state of our experiment. Likewise, some fraction of orientation must be preserved during a collision to observe the collisional satellite lines. The resulting collisional to direct line intensity ratios in LIF and PL spectra yield information about the transfer of population and orientation between different rotational levels in the inelastic collisions. A comparison of LIF and PL spectra is shown in Fig. 5.5 for NaK with helium perturbers. Notice that in PL spectra, the signals can be either positive or negative because of the absorption effects of the alkali vapor. For a given transition, one of the circular components of the probe beam is absorbed more. This effect causes lines of the P and R branches to have opposite signs. Depending on the adjustment of the polarizers and windows, Q lines are observed to have a dispersion shape when the P and R lines are Lorentzian. This feature makes

line identifications within the collisional relaxation much easier.

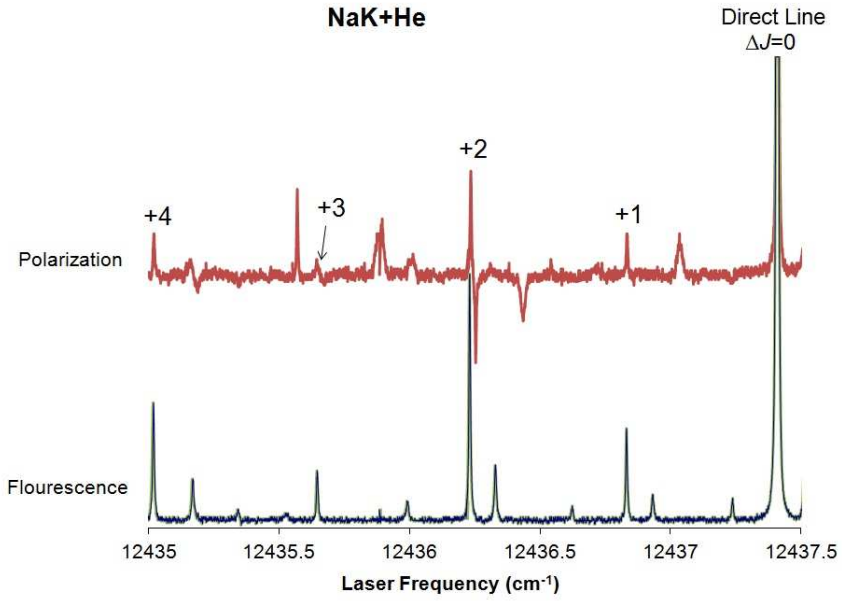

Figure 5.5: Comparison of fluorescence and polarization spectra. The direct line and collisional lines associated with positive J changes are labeled in the figure. The direct line intensity goes far off scale.

5.4.2 Measuring and Minimizing Polarization Background

Background noise is a serious concern for polarization spectroscopy, where we try to detect a relatively small signal. Sources of background can include stray light from non-laser sources, pump laser scatter, probe laser scatter, window effects, and imperfect polarizers. We minimized stray light by enclosing the detector in a light-isolated box with an entrance aperture only large enough for the beam to pass (see Fig. 4.1). Pump laser scatter occurs whenever the beam encounters an optical element on its path. Pump laser scatter is a serious problem because the pump laser is mechanically chopped. Therefore this is one source of noise that is not eliminated by lock-in detection. Filters and baffles are used to keep the scattered pump laser light from reaching the detector. The detector is orientated such that it faces away

from the experiment (a small mirror is used to direct only the probe beam onto the detector surface). This arrangement also helps to reject pump beam scatter. Probe scatter is also a serious problem because it cannot be filtered out by wavelength. However, probe scatter is not modulated, so it is filtered out by lock-in detection. Again, baffles are used to ensure that only probe light passing through the oven and crossed polarizers reaches the detector. In the end, we are able to reduce the detected pump and probe scatter to a point where they are negligible compared to other noise sources described below.

The polarization signal, as previously shown, is given by

$$I_t = I_0 e^{-2(\beta+\alpha)} \left\{ \xi + (\theta')^2 + (\Delta\beta)^2 + (2\Delta\beta + \Delta\alpha_0) \frac{\Delta\alpha_0}{1+x^2} + 2\theta' \frac{\Delta\alpha_0 x}{1+x^2} \right\}. \quad (5.17)$$

The first three terms, ξ, $(\theta')^2$, and $\Delta\beta^2$, of the signal contribute to background. The first term, ξ, represents the transmission of the polarizers when they are crossed. Since the polarizers are not perfect, there is some leakage through the analyzer that reaches the polarization PMT. The second term, $\theta' = \theta + \Delta b$, arises from the imperfect (intentional) crossing of the polarizers and from the difference in window birefringence, Δb, for right and left circularly polarized light. The third term, $\Delta\beta^2$, represents the difference in absorption in the windows for right and left circularly polarized light (circular dichroism). We chose BK7 glass for the windows on the heat pipe oven, specifically for its small circular dichroism and birefringence. We also use high quality Glan-Thompson polarizers with a high extinction ratio to minimize the effects due to ξ.

The extinction of the polarizers was measured with the heat pipe removed from between the polarizers. To avoid overloading the PMT, the laser power was attenuated using neutral density filters. Two methods were used to determine the effects of the neutral density filters. One was to directly measure the power of the laser with and without the stack of filters using a ThorLabs power meter. The second method was to chop the laser and use the PMT lock-in amplifier to determine the fraction of the laser power that was transmitted by each filter in turn. In this measurement, we also used the polarizers as a variable attenuator. The crossing angle was adjusted

until a large (a few nA), but not too large (less than 1 μA), signal was obtained so that large changes in the signal can be observed without the risk of damaging the PMT. Then we removed a filter and recorded the signal change. This process was repeated until all of the filters had been removed. In this manner, all neutral density filters could be calibrated for the laser wavelength. Use of the polarizers was necessary in this procedure to prevent overloading the PMT.

To carry out the polarizer extinction measurement, the full stack of neutral density filters was put in place, and the PMT signal was maximized by rotating the analyzer to an uncrossed orientation. This signal, divided by the neutral density stack attenuation factor, was recorded as the intensity transmitted by the polarizer pair when their polarization axes were parallel. The analyzer was then crossed relative to the polarizer (as neutral density filters were removed and the signal change recorded) until the signal was minimized and all the neutral density filters had been removed. The ratio of signal with the polarizers crossed to the signal with them uncrossed (and accounting for the effects of the neutral density filters) is the extinction ratio. With the heat pipe removed, the signal on the lock-in is dependent only on the ξ term in Eq. 5.17. Our measurement of the the polarizer extinction yields $\xi \approx 3.0 \times 10^{-9}$.

Once the polarizers are set to a crossed orientation, neutral density filters are reintroduced and the cold heat pipe is lowered into the beam path. As expected, the heat pipe windows change the polarization of the beam slightly and allow more light to pass through the analyzer. The neutral density filters are therefore needed to protect the PMT, but much less attenuation than in the extinction measurement is necessary. After the heat pipe has been placed in the beam path, Eq. (5.17) tells us that the transmitted signal is $I_{\mathrm{t}} = I_0(\xi + \Delta b^2 + \Delta\beta^2)$, where we have set the uncrossing angle, $\theta = 0$. The angle of the analyzer was then adjusted to minimize the total signal by adjusting the contribution of the $\theta' = \theta + \Delta b$ term, i.e. by setting $\theta' = 0$. In principle, the analyzer is rotated from $\theta = 0$ to $\theta' = 0$ and hence the amount of rotation yields a value for Δb. However, due to the limited resolution of the analyzer rotation mount and the small effects on the lock-in signal, we can

only conclude that the window birefringance term is quite small; i.e., $\Delta b \approx 0$, to within our measurement accuracy. With $\theta' = 0$, the remaining signal is given by $I_t = I_0(\xi + \Delta\beta^2)$. From this measurement, we determined that the window circular dichroism term is $\Delta\beta \approx 3.9 \times 10^{-6}$.

It is important to note that the background terms can change somewhat from day to day. As we want Lorentzian lineshapes for the polarization spectroscopy signals, we eliminate the dispersion term in Eq. (5.17) by setting $\theta' = 0$. However, the leading Lorentzian term is the $(\Delta\beta\Delta\alpha_0)$ term which depends on non-negligible circular dichroism of the windows. But the $\Delta\beta^2$ term is also the dominant background term. The background window terms can fluctuate from the effects of stress from being pumped on by the vacuum, pressure exerted by the bolts, and cleanliness of windows. These effects are checked and minimized regularly. If the window dichroism background term becomes too large, it is not possible to record clean polarization signals for the collisional lines. Although the background terms are not modulated, and hence are filtered out using lock-in detection, they can still be large enough to saturate the detector. Typically we increase the PMT voltage until the background signal (as measured with a picoammeter) is $\sim 300\,\mathrm{nA}$. Noise becomes a serious issue when the PMT voltage cannot be increased past 350V.

Chapter 6

Analysis and Results

6.1 Overview

In this chapter, I describe the data set we have obtained for the rotationally inelastic collisions of NaK and NaCs molecules, and how the data are analyzed to determine population transfer and destruction of orientation in these collisions.

In Sec. 6.2, I discuss how uncertainties are assigned in this work and what the major sources of known error are in this work. Section 6.3 discuses the analysis of recorded spectra. In Sec. 6.4, I discuss the fitting methods and give the results of our work investigating inelastic collisions of NaK with helium and argon. Comparison of the results from different fitting methods is given in Sec. 6.5. As an interesting contrast, our results from the study of inelastic collisions involving NaCs molecules are presented in Sec. 6.6. We have also begun investigations of vibrationally inelastic collisions in a collaboration with Drs. Ross and Crozet in the Université Lyon and this experiment is discussed in Sec. 6.7. As a by-product of our analysis of the rotationally inelastic collision data at Lehigh, we also determine properties about line broadening due to the various perturbers. These results are presented in Sec. 6.8. Lastly, comparison between experiment and theory is discussed in Sec. 6.9.

6.2 Uncertainties

In the present work, the most significant source of error stems from the uncertainty in the determination of the alkali atom densities. As described in Sec. 5.2.2, we obtain potassium densities in the NaK experiment (or cesium densities in the NaCs experiment) by recording white light absorption of the D1 and D2 transitions of potassium (cesium). However, uncertainty in the alkali density arises due to the nature of the operation of the heat pipe oven. The alkali densities are roughly controlled by adjusting the power supplied to the heating coils surrounding the heat pipe oven. When hot, the heat pipe oven is a dynamic system, and definitely not in thermal equilibrium. Therefore, it is difficult to account for effects such as migration of the alkali metal from the center of the heat pipe. Over time, the sodium and potassium (cesium) actually begin to separate, resulting in lower NaK (NaCs) molecule densities within the center of the heat pipe oven. Moreover, the alkali vapor density is not uniform throughout the oven. Additionally, the white light equivalent width measurements sample the absorption along the entire length of the vapor enclosed within the heat pipe, whereas the fluorescence signals are collected only from a small region at the center of the oven within view of the side windows, and the polarization spectra are gathered from the region of the heat pipe where the pump beam and probe beam overlap. The fact that we are using thermocouples to measure the temperature of the heat pipe oven on the outside of each arm increases our uncertainty slightly due to the fact that we are not measuring the actual temperature within the heat pipe oven. Taking all this into account, and based on previous measurements in our lab done by Jabbour *et al.* [63], Wolfe *et al.* [30], and our own density measurements, we believe that a conservative error bar of thirty percent on the potassium density (or cesium density) is reasonable.

We associate less uncertainty to the inert gas density which we control with regulating valves and measure just outside the heat pipe oven with a capacitance manometer. Since the system is open so that gas continuously flows into and out of the heat pipe oven, the total pressure measured outside by the capacitance manometer is equal to the total pressure inside the oven. Thus $P_{meas} = P_{alk} + P_{buf}$. Since we

can measure pressure to an accuracy of 0.01 Torr with the capacitance manometer, we assign an uncertainty to the buffer gas pressure in the heat pipe oven as [43]

$$\frac{\delta P_{buf}}{P_{buf}} = \frac{0.01\,\text{Torr}}{P_{buf}} + 0.3\frac{P_{alk}}{P_{buf}}\,. \tag{6.1}$$

The contributions to the error are due to the pressure gauge uncertainty (first term of the right hand side) and the uncertainty in the alkali partial pressure (second term of the right hand side of Eq. (6.1)).

The uncertainties in the buffer gas pressure and the alkali vapor pressure are incorporated into the uncertainties of the number densities of each species and therefore are also incorporated into the uncertainties of fluorescence ratios (R_F) and polarization ratios (R_P). The total error in the fluorescence ratio is determined by

$$\delta R_F = \left|\frac{\partial R_F}{\partial n_{buf}}\right|\delta n_{buf} + \left|\frac{\partial R_F}{\partial n_{alk}}\right|\delta n_{alk}\,. \tag{6.2}$$

Referring to Eq. (3.6), it can be seen that

$$\left|\frac{\partial R_F}{\partial n_{buf}}\right| = \left|\frac{\frac{k_{buf}^{\Delta J}}{\Gamma}}{1+\frac{k_{buf}^{Q}}{\Gamma}n_{buf}+\frac{k_{alk}^{Q}}{\Gamma}n_{alk}} - \frac{\left(\frac{k_{buf}^{\Delta J}}{\Gamma}n_{buf}+\frac{k_{alk}^{\Delta J}}{\Gamma}n_{alk}\right)\frac{k_{buf}^{Q}}{\Gamma}}{\left(1+\frac{k_{buf}^{Q}}{\Gamma}n_{buf}+\frac{k_{alk}^{Q}}{\Gamma}n_{alk}\right)^2}\right| \tag{6.3}$$

and

$$\left|\frac{\partial R_F}{\partial n_{alk}}\right| = \left|\frac{\frac{k_{alk}^{\Delta J}}{\Gamma}}{1+\frac{k_{buf}^{Q}}{\Gamma}n_{buf}+\frac{k_{alk}^{Q}}{\Gamma}n_{alk}} - \frac{\left(\frac{k_{buf}^{\Delta J}}{\Gamma}n_{buf}+\frac{k_{alk}^{\Delta J}}{\Gamma}n_{alk}\right)\frac{k_{alk}^{Q}}{\Gamma}}{\left(1+\frac{k_{buf}^{Q}}{\Gamma}n_{buf}+\frac{k_{alk}^{Q}}{\Gamma}n_{alk}\right)^2}\right|. \tag{6.4}$$

The relative uncertainty in the fluorescence ratio is given by

$$\begin{aligned}\frac{\delta R_F}{R_F} &= \frac{1}{R_F}\left|\frac{\partial R_F}{\partial n_{buf}}\right|\delta n_{buf} + \frac{1}{R_F}\left|\frac{\partial R_F}{\partial n_{alk}}\right|\delta n_{alk} \\ &= \left|\frac{\frac{k_{buf}^{\Delta J}}{\Gamma}}{\frac{k_{buf}^{\Delta J}}{\Gamma}n_{buf}+\frac{k_{alk}^{\Delta J}}{\Gamma}n_{alk}} - \frac{\frac{k_{buf}^{Q}}{\Gamma}}{1+\frac{k_{buf}^{Q}}{\Gamma}n_{buf}+\frac{k_{alk}^{Q}}{\Gamma}n_{alk}}\right|\delta n_{buf} \\ &\quad + \left|\frac{\frac{k_{alk}^{\Delta J}}{\Gamma}}{\frac{k_{buf}^{\Delta J}}{\Gamma}n_{buf}+\frac{k_{alk}^{\Delta J}}{\Gamma}n_{alk}} - \frac{\frac{k_{alk}^{Q}}{\Gamma}}{1+\frac{k_{buf}^{Q}}{\Gamma}n_{buf}+\frac{k_{alk}^{Q}}{\Gamma}n_{alk}}\right|\delta n_{alk}\,.\end{aligned} \tag{6.5}$$

A similar analysis yields the uncertainties in the polarization ratios using Eq. (3.43)

$$\begin{aligned}\frac{\delta R_P}{R_P} &= \frac{1}{R_P}\left|\frac{\partial R_P}{\partial n_{buf}}\right|\delta n_{buf} + \frac{1}{R_P}\left|\frac{\partial R_P}{\partial n_{alk}}\right|\delta n_{alk} \\ &= \left|\frac{\frac{k_{buf}^{\Delta J}}{\Gamma}(1-f_{buf}^{\Delta J})}{\frac{k_{buf}^{\Delta J}}{\Gamma}(1-f_{buf}^{\Delta J})n_{buf} + \frac{k_{alk}^{\Delta J}}{\Gamma}(1-f_{alk}^{\Delta J})n_{alk}} - \frac{\frac{g_{buf}}{\Gamma}}{1+\frac{g_{buf}}{\Gamma}n_{buf}+\frac{g_{alk}}{\Gamma}n_{alk}}\right|\delta n_{buf} \\ &+ \left|\frac{\frac{k_{alk}^{\Delta J}}{\Gamma}(1-f_{alk}^{\Delta J})}{\frac{k_{buf}^{\Delta J}}{\Gamma}(1-f_{buf}^{\Delta J})n_{buf} + \frac{k_{alk}^{\Delta J}}{\Gamma}(1-f_{alk}^{\Delta J})n_{alk}} - \frac{\frac{g_{alk}}{\Gamma}}{1+\frac{g_{buf}}{\Gamma}n_{buf}+\frac{g_{alk}}{\Gamma}n_{alk}}\right|\delta n_{alk}\,.\end{aligned} \tag{6.6}$$

In addition to uncertainties associated with the atomic perturber densities, there are also uncertainties in the recorded intensities of the direct and collisional spectral lines. These uncertainties are determined by examining the baseline noise from scans taken with the most sensitive setting. The minimum and maximum of the baseline are used to determine the uncertainty in the intensity for each day data are recorded. We can see from Eq. (3.6) that the relative uncertainty contributions from the collisional and direct line intensity ratios are

$$\frac{\delta R_F}{R_F} = \frac{\delta I_{col}^F}{I_{col}^F} + \frac{\delta I_{dir}^F}{I_{dir}^F} \tag{6.7}$$

for fluorescence, and similarly for the polarization signals

$$\frac{\delta R_P}{R_P} = \frac{\delta I_{col}^P}{I_{col}^P} + \frac{\delta I_{dir}^P}{I_{dir}^P}\,. \tag{6.8}$$

We include the uncertainty in the intensities for fluorescence and polarization signals by adding them to Eq. (6.5) and Eq. (6.6), respectively, to yield

$$\frac{\delta R_F}{R_F} = \frac{1}{R_F}\left|\frac{\partial R_F}{\partial n_{buf}}\right|\delta n_{buf} + \frac{1}{R_F}\left|\frac{\partial R_F}{\partial n_{alk}}\right|\delta n_{alk} + \frac{\delta I_{col}^F}{I_{col}^F} + \frac{\delta I_{dir}^F}{I_{dir}^F} \tag{6.9}$$

and

$$\frac{\delta R_P}{R_P} = \frac{1}{R_P}\left|\frac{\partial R_P}{\partial n_{buf}}\right|\delta n_{buf} + \frac{1}{R_P}\left|\frac{\partial R_P}{\partial n_{alk}}\right|\delta n_{alk} + \frac{\delta I_{col}^P}{I_{col}^P} + \frac{\delta I_{dir}^P}{I_{dir}^P}\,. \tag{6.10}$$

Equations (6.9) and (6.10) account for the errors in the alkali and noble gas atom densities (the independent variables in our fits) by incorporating them into the errors in the dependent variables R_F and R_P. This approach simplifies the fitting process and is convenient since the version of the fitting software, Origin, available in our lab, does not provide an option to assign error bars to the independent variables. The uncertainties quoted in the results presented in this dissertation are the statistical uncertainties obtained from the least-squares fits of the data as determined using the Origin non-linear fitting tool. However, we must realize that some of the sources of error in this work are systematic, and this must be taken into account when interpreting the results.

6.3 Analysis of Spectra

In recording data for this work, we have to be careful to control the collision environment. In particular, we want to make sure that the perturber density is sufficiently low that we remain in the single-collision regime. To do this, we require the collision rates to be much less than the radiative rate. This means keeping the alkali density and buffer gas densities low. However, every experiment involves trade-offs and we also need to ensure that there is enough alkali vapor and buffer gas atoms to provide a sufficiently large number of molecules for usable signal, and a sufficiently large number of collisions to distinguish collisional lines from the background noise. In this vein, we must also carefully control the ratio of alkali atom to buffer gas atom densities in order to determine their separate effects as collision partners. The cross-sections for rotationally inelastic collisions of NaK and NaCs molecules with alkali atom perturbers are typically larger than those for inert gas atom perturbers. In NaK, the rotationally inelastic collisional rate coefficients for potassium are about an order of magnitude larger than those for inert gases for the $\Delta J =$ odd collisions. The inert gas pressure must also be kept at least equal to the alkali pressure to prevent the alkali from coating the oven windows.

In observing the direct and collisional lines in this research at Lehigh, we have

noticed that the collisional lines are broader than the direct lines. Therefore, we cannot simply take the ratio of peak heights to get an accurate measure of the fluorescence and polarization intensity ratios. The OODR technique is intrinsically Doppler-free. However, pressure broadening affects both the direct and collisional lines, while the collisional lines experience additional broadening due to the inelastic collisions they have suffered that also can change the velocity of the molecule (and re-introduce some Doppler broadening). For our analysis, we incorporate these effects by using spectral line areas to determine intensity ratios.

To determine line areas, the first step is to assign a baseline to each spectrum. In our work at Lehigh, we determine a two point, sloping baseline with a point on either side of line center, and sufficiently far from line center that they are not significantly affected by the wings of the spectral line of interest. After we have determined a baseline, we integrate the area of the peak and determine the height and FWHM.

In the case of the spectra taken using the Fourier transform spectrometer in Lyon, we simply use peak heights in determining the fluorescence ratios. The width of each peak is limited by the resolution of the Bomem FTS (the NaK fluorescence peaks are much narrower than the absorption dips for the potassium atomic lines). The instrument resolution causes the direct and collisional lines to have the same widths. Therefore, intensity ratios can be determined from peak heights for the Lyon data. An additional advantage of the fact that all lines should have approximately the same width is that it allows us to determine if a given peak is contaminated by an overlapping peak. A peak that is significantly broader than the rest is likely to be contaminated by an overlapping peak and therefore should not be used in the analysis.

Another advantage of the FT spectra is that the same upper state population can be observed on several transitions ($\Delta J = \pm 1$ and many different lower state vibrational levels). Thus, we check our fluorescence ratios using direct and collisional lines associated with P or R sequences belonging to different lower state vibrational

levels. We note that the fluorescence ratios obtained from data collected in Lyon are consistent with the fluorescence ratios obtained using the OODR technique at Lehigh in the present work and in the work of Wolfe *et al.* [30].

6.4 NaK Population and Orientation Transfer

6.4.1 Inelastic Collisions of NaK $2(A)^1\Sigma^+(16, 30)$ Molecules

In this section we present our results for population and orientation transfer of NaK $2(A)^1\Sigma^+(16, 30)$ molecules colliding with argon and helium pertrubers. We have used various methods to fit our data. The results of each fitting method are presented in tables in this chapter. Since we have refit the collisional rate coefficients using the data from Wolfe *et al.* [30] in addition to our new data from Lyon, improved argon rate coefficients are also reported.

Due to correlations between some of the parameters in the fit of both R_F and R_P, there is a tendency for certain parameters to "run away" (i.e., fail to converge to a finite value). To address this issue, we employed various methods of fitting the data for comparison. These data are fit using the R_F and R_P equations [Eqs. (3.6) and (3.43)] using the computer program Origin (Ver. 7.5), with the built-in multiple regression analysis. We input an initial order-of-magnitude estimate for the value of each parameter and set upper and lower bounds on the parameters as needed; i.e., each f value must be between 0 and 1, and rate coefficients cannot be negative.

In each of the fitting methods, the values of g'_X were fixed according to Eq. (3.44). The parameter of g'_X is highly correlated to the f_X and k_X^Q values and sometimes fails to converge to a finite value if left to vary in the fitting process. Thus we fix g'_X to the value given by the approximation in Eq. (3.44). Tests of the fitting show that setting g'_X to zero in the fit for any species X, changes the corresponding f_X and k_X^Q values by only a few percent due to the fact that g'_X is more than one order of magnitude smaller than the quenching rate for that perturber. Setting the

value of $g_x = k_X^Q + g'_X$ equal to the contribution from species X to the collisional line width, k_X^{br}, of the direct line, which should represent an upper limit on g_X, causes some of the f-values to converge to one, and yields much higher χ^2 values. For each separate fitting method, the g' values were manually adjusted at each iteration according to Eq. (3.44) using the new values of $k_X^{\Delta J}$ and f_X.

Global Fit

In the first method of fitting the data, we fit all of the polarization data and all fluorescence data simultaneously. We call this method the "global fit". In this global fit, we fit the data together since the equations for R_F and R_P share the global parameters, k_{buf}^Q and k_{alk}^Q and the individual ΔJ collision rate coefficients, $k_{buf}^{\Delta J}$ and $k_{alk}^{\Delta J}$. In our analysis, we also simultaneously fit the collisional data for NaK in a given initial ro-vibrational level of the $2(A)^1\Sigma^+$state with both argon and and helium perturbers, since the alkali parameters are still shared parameters regardless of the inert gas perturber. In the global fit, the potassium rate coefficients k_K^Q, $k_K^{\Delta J=\pm1,\pm2,\pm3,\pm4}$, and $f_K^{\Delta J}$ were common parameters to the helium, argon and heat-pipe mode data sets, while the argon rate coefficients, k_{Ar}^Q, $k_{Ar}^{\Delta J}$, and $f_{Ar}^{\Delta J}$ were only relevant for the argon data (and similarly for helium). The population transfer rate coefficients resulting from this fit are listed in Table 6.1 and the orientation transfer f-values are presented in Table 6.2.

Global Fit
Population transfer and quenching rate coefficients
NaK $2(A)^1\Sigma^+(16,30)$

	Argon	Helium	Potassium
ΔJ	$k_{Ar}^{\Delta J}(10^{-11}\,\mathrm{cm^3 s^{-1}})$	$k_{He}^{\Delta J}(10^{-11}\,\mathrm{cm^3 s^{-1}})$	$k_{K}^{\Delta J}(10^{-10}\,\mathrm{cm^3 s^{-1}})$
-4	9.3 ± 0.7	11 ± 1	1.6 ± 0.2
-3	7.0 ± 0.6	2.2 ± 0.2	2.0 ± 0.2
-2	20 ± 1	20 ± 1	3.7 ± 0.4
-1	10 ± 1	4.2 ± 0.4	5.0 ± 0.5
+1	8.3 ± 0.7	3.7 ± 0.5	8.5 ± 0.7
+2	20 ± 1	20 ± 1	7.1 ± 0.7
+3	5.3 ± 0.4	3.2 ± 0.3	2.4 ± 0.3
+4	8.7 ± 0.6	11 ± 1	1.7 ± 0.2
Quenching	$k_{Ar}^{Q}(10^{-9}\,\mathrm{cm^3 s^{-1}})$	$k_{He}^{Q}(10^{-9}\,\mathrm{cm^3 s^{-1}})$	$k_{K}^{Q}(10^{-8}\,\mathrm{cm^3 s^{-1}})$
	1.3 ± 0.1	1.8 ± 0.1	1.2 ± 0.1

Table 6.1: Table of parameters determined from the "global fit" method using fluorescence ratio (R_F) data and polarization ratio (R_P) data for collisions of NaK $2(A)^1\Sigma^+(16,30)$ molecules with argon, helium, and potassium. $\Gamma = 4.4 \times 10^7\,\mathrm{s^{-1}}$, determined using the computer program LEVEL [40] with the $2(A)^1\Sigma^+$potential of Ref. [11], the $1(X)^1\Sigma^+$potential of Ref. [10] and the transition dipole moment function of Ref. [33].

Global Fit
Transfer of Orientation
NaK $2(A)^1\Sigma^+(16,30)$

	Argon	Helium	Potassium
ΔJ	$f_{Ar}^{\Delta J}$	$f_{He}^{\Delta J}$	$f_{K}^{\Delta J}$
-4	0.71 ± 0.04	0.66 ± 0.05	0.95 ± 0.04
-3	0.67 ± 0.05	0 ± 0.33	0.87 ± 0.05
-2	0.50 ± 0.04	0.30 ± 0.05	0.91 ± 0.02
-1	0.47 ± 0.05	0.27 ± 0.17	0.96 ± 0.01
+1	0.35 ± 0.05	0 ± 0.23	0.94 ± 0.01
+2	0.53 ± 0.03	0.19 ± 0.06	0.92 ± 0.01
+3	0.57 ± 0.06	0 ± 0.31	0.89 ± 0.05
+4	0.52 ± 0.06	0 ± 0.11	1 ± 0.15

Table 6.2: Table of parameters determined from the "global fit" method using fluorescence ratio (R_F) data and polarization ratio (R_P) data for collisions of NaK $2(A)^1\Sigma^+(16,30)$ molecules with argon, helium, and potassium. $\Gamma = 4.4 \times 10^7\,\mathrm{s}^{-1}$, determined using the computer program LEVEL [40] with the $2(A)^1\Sigma^+$potential of Ref. [11], the $1(X)^1\Sigma^+$potential of Ref. [10] and the transition dipole moment function of Ref. [33]. The value of $f_X^{\Delta J}$ represents the fraction of orientation destroyed in a collision of NaK $2(A)^1\Sigma^+(16,30)$ molecules with atoms of species X where the final molecular state has rotational quantum number $30 + \Delta J$.

Separate Buffer Gas Fit

In the second method, we fit the argon fluorescence and polarization data separately from the helium fluorescence and polarization data. In this case, though we separate the data for different buffer gases, we still fit the corresponding R_F and R_P data together for a given buffer gas. We call this the "separate buffer gas fit". Since the heat pipe mode data is included with the argon data but not with the helium data, we used the potassium parameters $k_K^{\Delta J}$, k_K^Q, and $f_K^{\Delta J}$ determined from the argon fit and fixed them in the helium fit to determine $k_{He}^{\Delta J=\pm1,\pm2,\pm3,\pm4}$, k_{He}^Q, and $f_K^{\Delta J}$. Results from the separate buffer gas fit are presented in Tables 6.3 and 6.4.

Separate Buffer Gas Fit
Population transfer and quenching rate coefficients
NaK $2(A)^1\Sigma^+(16,30)$

	Argon	Helium	Potassium
ΔJ	$k_{Ar}^{\Delta J}(10^{-11}\,\mathrm{cm^3 s^{-1}})$	$k_{He}^{\Delta J}(10^{-11}\,\mathrm{cm^3 s^{-1}})$	$k_{K}^{\Delta J}(10^{-10}\,\mathrm{cm^3 s^{-1}})$
-4	9.3 ± 0.7	11 ± 1	1.6 ± 0.2
-3	7.0 ± 0.6	2.1 ± 0.2	2.1 ± 0.3
-2	20 ± 1	19 ± 1	3.7 ± 0.5
-1	10 ± 0.8	4.1 ± 0.3	5.0 ± 0.6
+1	8.2 ± 0.7	3.3 ± 0.5	8.7 ± 0.9
+2	20 ± 1	19 ± 1	7.3 ± 0.8
+3	5.3 ± 0.4	3.1 ± 0.2	2.5 ± 0.3
+4	8.7 ± 0.7	11 ± 1	1.7 ± 0.3
Quenching	$k_{Ar}^{Q}(10^{-9}\,\mathrm{cm^3 s^{-1}})$	$k_{He}^{Q}(10^{-9}\,\mathrm{cm^3 s^{-1}})$	$k_{K}^{Q}(10^{-8}\,\mathrm{cm^3 s^{-1}})$
	1.3 ± 0.1	1.7 ± 0.1	1.2 ± 0.2

Table 6.3: Table of parameters determined from the "separate buffer gas fit" method using fluorescence ratio (R_F) data and polarization ratio (R_P) data for collisions of NaK $2(A)^1\Sigma^+(16,30)$ molecules with argon, helium, and potassium. $\Gamma = 4.4 \times 10^7\,\mathrm{s^{-1}}$, determined using the computer program LEVEL [40] with the $2(A)^1\Sigma^+$potential of Ref. [11], the $1(X)^1\Sigma^+$potential of Ref. [10] and the transition dipole moment function of Ref. [33].

Separate Buffer Gas Fit
Transfer of Orientation
NaK $2(A)^1\Sigma^+(16, 30)$

	Argon	Helium	Potassium
ΔJ	$f_{Ar}^{\Delta J}$	$f_{He}^{\Delta J}$	$f_{K}^{\Delta J}$
-4	0.71 ± 0.04	0.66 ± 0.05	0.95 ± 0.04
-3	0.66 ± 0.05	0 ± 0.34	0.87 ± 0.05
-2	0.50 ± 0.04	0.30 ± 0.05	0.91 ± 0.02
-1	0.47 ± 0.05	0.28 ± 0.16	0.96 ± 0.01
+1	0.33 ± 0.06	0 ± 0.25	0.94 ± 0.01
+2	0.53 ± 0.03	0.19 ± 0.05	0.92 ± 0.01
+3	0.56 ± 0.06	0 ± 0.32	0.90 ± 0.05
+4	0.49 ± 0.06	0 ± 0.10	1 ± 0.15

Table 6.4: Table of parameters determined from the "separate buffer gas fit" method using fluorescence ratio (R_F) data and polarization ratio (R_P) data for collisions of NaK $2(A)^1\Sigma^+(16, 30)$ molecules with argon, helium, and potassium. $\Gamma = 4.4 \times 10^7\,\mathrm{s}^{-1}$, determined using the computer program LEVEL [40] with the $2(A)^1\Sigma^+$potential of Ref. [11], the $1(X)^1\Sigma^+$potential of Ref. [10] and the transition dipole moment function of Ref. [33]. The value of $f_X^{\Delta J}$ represents the fraction of orientation destroyed in a collision of NaK $2(A)^1\Sigma^+(16, 30)$ molecules with atoms of species X where the final molecular state has rotational quantum number $30 + \Delta J$.

Fluorescence and Polarization Fit

In the third method, we separated the fluorescence data from the polarization data in the fits, first fitting all of the fluorescence data for the argon and the helium data sets simultaneously. We then used the collisional rate coefficients ($k_{Ar}^{\Delta J}$, $k_{He}^{\Delta J}$, $k_{K}^{\Delta J}$, k_{Ar}^{Q}, k_{He}^{Q}, and k_{K}^{Q}) for argon, helium and potassium from the fit of the fluorescence data and fixed these values when fitting the polarization data for argon and helium data sets together. We call this method the "fluorescence and polarization fit". Results from the fluorescence and polarization fit are presented in Tables 6.5 and 6.6.

Fluorescence and Polarization Fit
Population transfer rate coefficients
NaK $2(A)^1\Sigma^+(16,30)$

	Argon	Helium	Potassium
ΔJ	$k_{Ar}^{\Delta J}(10^{-11}\,\mathrm{cm^3 s^{-1}})$	$k_{He}^{\Delta J}(10^{-11}\,\mathrm{cm^3 s^{-1}})$	$k_{K}^{\Delta J}(10^{-10}\,\mathrm{cm^3 s^{-1}})$
-4	9.4 ± 0.7	9.9 ± 0.6	1.0 ± 0.1
-3	7.3 ± 0.5	2.2 ± 0.2	1.3 ± 0.2
-2	21 ± 1	18 ± 1	2.4 ± 0.3
-1	11 ± 1	4.3 ± 0.3	3.2 ± 0.4
+1	9.4 ± 0.7	4.0 ± 0.5	5.9 ± 0.6
+2	21 ± 1	19 ± 1	4.6 ± 0.5
+3	5.6 ± 0.4	3.2 ± 0.2	1.6 ± 0.2
+4	8.6 ± 0.6	10 ± 1	1.1 ± 0.2
Quenching	$k_{Ar}^{Q}(10^{-9}\,\mathrm{cm^3 s^{-1}})$	$k_{He}^{Q}(10^{-9}\,\mathrm{cm^3 s^{-1}})$	$k_{K}^{Q}(10^{-9}\,\mathrm{cm^3 s^{-1}})$
	1.4 ± 0.1	1.7 ± 0.1	7.5 ± 1.0

Table 6.5: Table of parameters determined from the "fluorescence and polarization fit" method using fluorescence ratio (R_F) data and polarization ratio (R_P) data for collisions of NaK $2(A)^1\Sigma^+(16,30)$ molecules with argon, helium, and potassium. $\Gamma = 4.4\times10^7\,\mathrm{s^{-1}}$, determined from the computer program LEVEL [40] with the $2(A)^1\Sigma^+$potential of Ref. [11], the $1(X)^1\Sigma^+$potential of Ref. [10] and the transition dipole moment of Ref. [33].

Fluorescence and Polarization Fit
Transfer of Orientation
NaK $2(A)^1\Sigma^+(16,30)$

	Argon	Helium	Potassium
ΔJ	$f_{Ar}^{\Delta J}$	$f_{He}^{\Delta J}$	$f_{K}^{\Delta J}$
-4	0.76 ± 0.03	0.67 ± 0.05	0.95 ± 0.04
-3	0.71 ± 0.04	0 ± 0.29	0.86 ± 0.05
-2	0.58 ± 0.03	0.33 ± 0.05	0.91 ± 0.02
-1	0.56 ± 0.04	0.36 ± 0.14	0.96 ± 0.01
+1	0.47 ± 0.03	0 ± 0.16	0.94 ± 0.01
+2	0.60 ± 0.02	0.26 ± 0.05	0.92 ± 0.02
+3	0.63 ± 0.05	0 ± 0.28	0.90 ± 0.06
+4	0.56 ± 0.05	0.02 ± 0.10	1 ± 0.19

Table 6.6: Table of parameters determined from the "fluorescence and polarization fit" method using fluorescence ratio (R_F) data and polarization ratio (R_P) data for collisions of NaK $2(A)^1\Sigma^+(16,30)$ molecules with argon, helium, and potassium. $\Gamma = 4.4\times10^7\,\mathrm{s}^{-1}$, determined from the computer program LEVEL [40] with the $2(A)^1\Sigma^+$potential of Ref. [11], the $1(X)^1\Sigma^+$potential of Ref. [10] and the transition dipole moment of Ref. [33]. The value of $f_X^{\Delta J}$ represents the fraction of orientation destroyed in a collision of NaK $2(A)^1\Sigma^+(16,30)$ molecules with atoms of species X where the final molecular state has rotational quantum number $30 + \Delta J$.

Fully Separated Fit

In the fourth and final method, we separately fit the argon fluorescence data, the argon polarization data, the helium fluorescence data, and the helium polarization data sets. The argon data sets (which also include the heat pipe mode data) are more sensitive to the effects of potassium, and determine potassium rate coefficients with smaller error bars. Therefore, we determine the potassium rate coefficients $k_K^{\Delta J}$ and k_K^Q from the argon R_F fit and use them in the helium R_F data fit to yield the helium rate coefficients, $k_{He}^{\Delta J}$ and k_{He}^Q. We also use $k_{Ar}^{\Delta J}$, $k_K^{\Delta J}$, k_{Ar}^Q, and k_K^Q from the argon R_F fit in the argon R_P fit to yield $f_{Ar}^{\Delta J}$ and $f_K^{\Delta J}$. Finally, we use the $k_X^{\Delta J}$ and k_X^Q rate coefficients from the argon and helium R_F fits and $f_K^{\Delta J}$ from the argon R_P fit in the helium R_P fit to determine $f_{He}^{\Delta J}$. We call this fit the "fully separated fit", and results from this fit are presented in Tables 6.7 and 6.8.

Fully Separated Fit
Population transfer rate coefficients
NaK $2(A)^1\Sigma^+(16,30)$

	Argon	Helium	Potassium
ΔJ	$k_{Ar}^{\Delta J}(10^{-11}\,\mathrm{cm^3 s^{-1}})$	$k_{He}^{\Delta J}(10^{-11}\,\mathrm{cm^3 s^{-1}})$	$k_{K}^{\Delta J}(10^{-10}\,\mathrm{cm^3 s^{-1}})$
-4	9.0 ± 0.6	9.6 ± 0.5	0.9 ± 0.1
-3	7.1 ± 0.5	2.2 ± 0.2	1.1 ± 0.2
-2	20 ± 1	18 ± 1	2.0 ± 0.3
-1	11 ± 1	4.5 ± 0.3	2.6 ± 0.4
+1	9.3 ± 0.7	4.2 ± 0.4	5.0 ± 0.6
+2	20 ± 1	18 ± 1	3.9 ± 0.5
+3	5.4 ± 0.4	3.2 ± 0.2	1.4 ± 0.2
+4	8.3 ± 0.6	10 ± 1	1.0 ± 0.2
Quenching	$k_{Ar}^{Q}(10^{-9}\,\mathrm{cm^3 s^{-1}})$	$k_{He}^{Q}(10^{-9}\,\mathrm{cm^3 s^{-1}})$	$k_{K}^{Q}(10^{-9}\,\mathrm{cm^3 s^{-1}})$
	1.4 ± 0.1	1.7 ± 0.1	6.0 ± 1.0

Table 6.7: Table of parameters determined from the "fully separated fit" method using fluorescence ratio (R_F) data and polarization ratio (R_P) data for collisions of NaK $2(A)^1\Sigma^+(16,30)$ molecules with argon, helium, and potassium. $\Gamma = 4.4 \times 10^7\,\mathrm{s^{-1}}$, determined from the computer program LEVEL [40] with the $2(A)^1\Sigma^+$potential of Ref. [11], the $1(X)^1\Sigma^+$potential of Ref. [10] and the transition dipole moment of Ref. [33].

Fully Separated Fit
Transfer of Orientation
NaK $2(A)^1\Sigma^+(16,30)$

	Argon	Helium	Potassium
ΔJ	$f_{Ar}^{\Delta J}$	$f_{He}^{\Delta J}$	$f_{K}^{\Delta J}$
-4	0.77 ± 0.03	0.67 ± 0.05	0.94 ± 0.04
-3	0.73 ± 0.04	0 ± 0.28	0.86 ± 0.06
-2	0.60 ± 0.03	0.34 ± 0.05	0.90 ± 0.02
-1	0.59 ± 0.03	0.39 ± 0.13	0.96 ± 0.01
+1	0.50 ± 0.03	0 ± 0.15	0.95 ± 0.01
+2	0.62 ± 0.02	0.28 ± 0.05	0.92 ± 0.02
+3	0.65 ± 0.04	0 ± 0.26	0.90 ± 0.06
+4	0.54 ± 0.05	0.05 ± 0.10	1 ± 0.20

Table 6.8: Table of parameters determined from the "fully separated fit" method using fluorescence ratio (R_F) data and polarization ratio (R_P) data for collisions of NaK $2(A)^1\Sigma^+(16,30)$ molecules with argon, helium, and potassium. $\Gamma = 4.4 \times 10^7\,\mathrm{s}^{-1}$, determined from the computer program LEVEL [40] with the $2(A)^1\Sigma^+$potential of Ref. [11], the $1(X)^1\Sigma^+$potential of Ref. [10] and the transition dipole moment of Ref. [33]. The value of $f_X^{\Delta J}$ represents the fraction of orientation destroyed in a collision of NaK $2(A)^1\Sigma^+(16,30)$ molecules with atoms of species X where the final molecular state has rotational quantum number $30 + \Delta J$.

6.5 Comparison of Fitting Methods and Results

Figures 6.1 through 6.13 show comparisons of the rate coefficients and f values obtained from the different fitting procedures. It can be seen that the different fitting methods produce results that are consistent within error bars. However, it appears that the global fit generally produces the "best" results (smallest error bars). This is not surprising since the global fit method uses all available data to determine each parameter. In the remainder of this chapter, we will only continue the discussion using the global fit results.

Plots of measured helium R_F values for each ΔJ and for each experimental "run" (different helium densities but fixed potassium density) are shown in Figs. 6.14 to 6.21, along with calculated R_F values obtained using the global fit parameters of Table 6.1. Similar plots for helium R_P values are shown in Figs. 6.22 to 6.29 along with calculated final R_P values obtained using the parameters of Tables 6.1 and 6.2. Final $k_{Ar}^{\Delta J}$, $k_{He}^{\Delta J}$ and $k_{K}^{\Delta J}$ values are plotted versus ΔJ in Figs. 6.30 to 6.32, while $f_{Ar}^{\Delta J}$, $f_{He}^{\Delta J}$, and $f_{K}^{\Delta J}$ are plotted in Figs. 6.33 to 6.35. Comparisons of the quenching rate coefficients are presented in Fig. 6.7

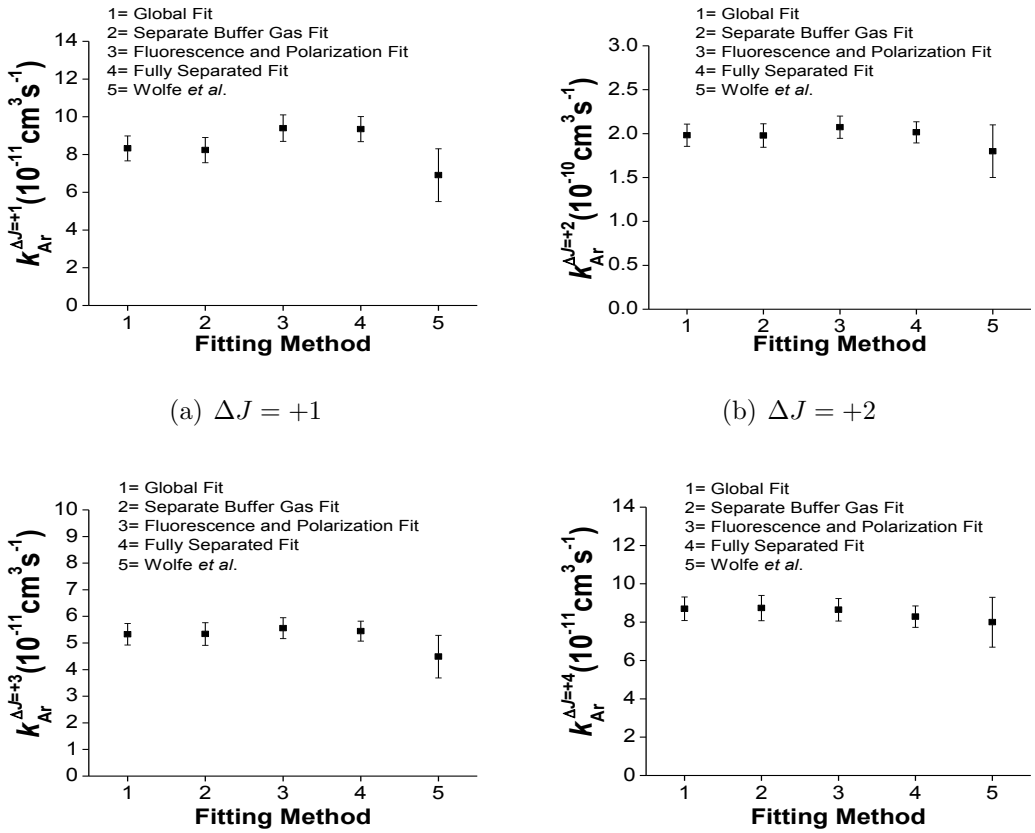

(a) $\Delta J = +1$

(b) $\Delta J = +2$

(c) $\Delta J = +3$

(d) $\Delta J = +4$

Figure 6.1: Plots of the fitted argon rate coefficients for positive ΔJ collisions obtained using each of the described fitting methods.

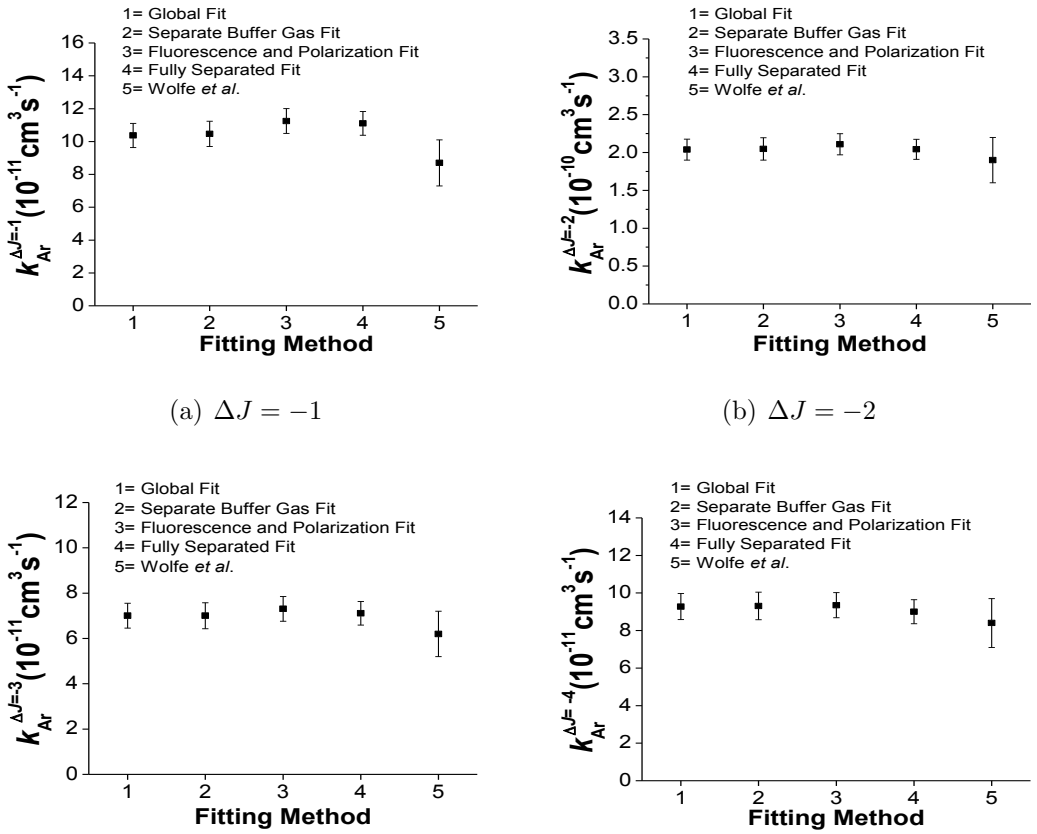

(a) $\Delta J = -1$

(b) $\Delta J = -2$

(c) $\Delta J = -3$

(d) $\Delta J = -4$

Figure 6.2: Plots of the fitted argon rate coefficients for negative ΔJ collisions for each of the described fitting methods.

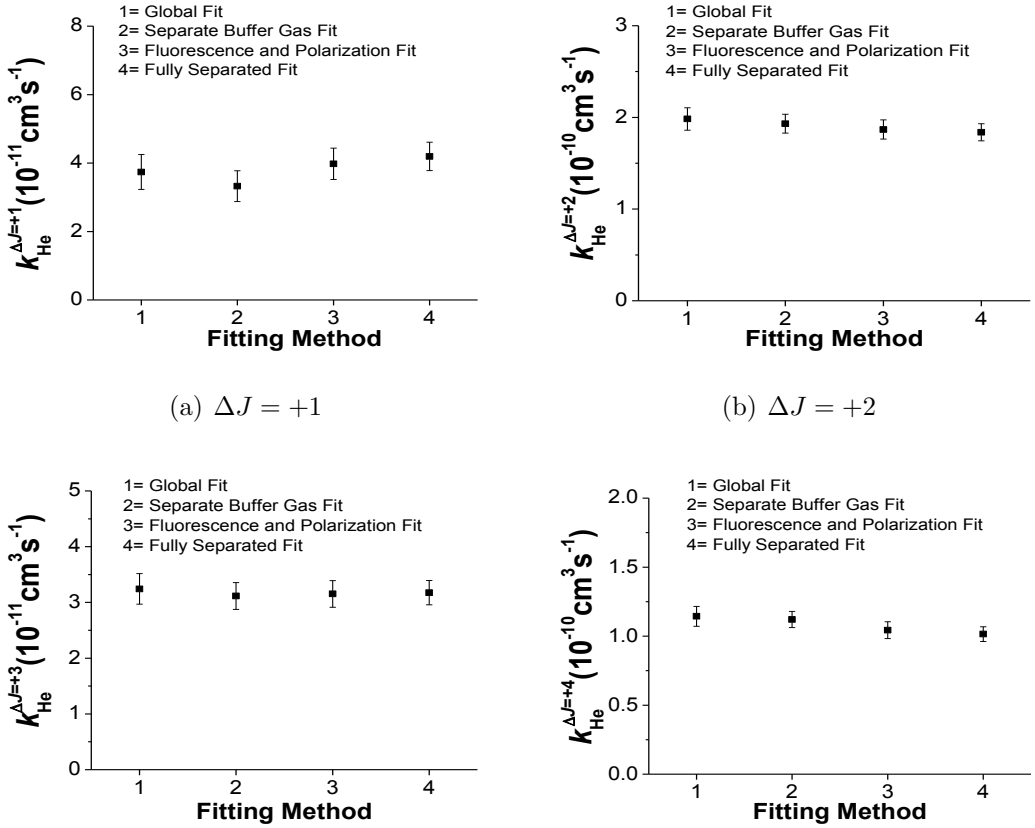

(a) $\Delta J = +1$

(b) $\Delta J = +2$

(c) $\Delta J = +3$

(d) $\Delta J = +4$

Figure 6.3: Plots of the fitted helium rate coefficients for positive ΔJ collisions for each of the described fitting methods.

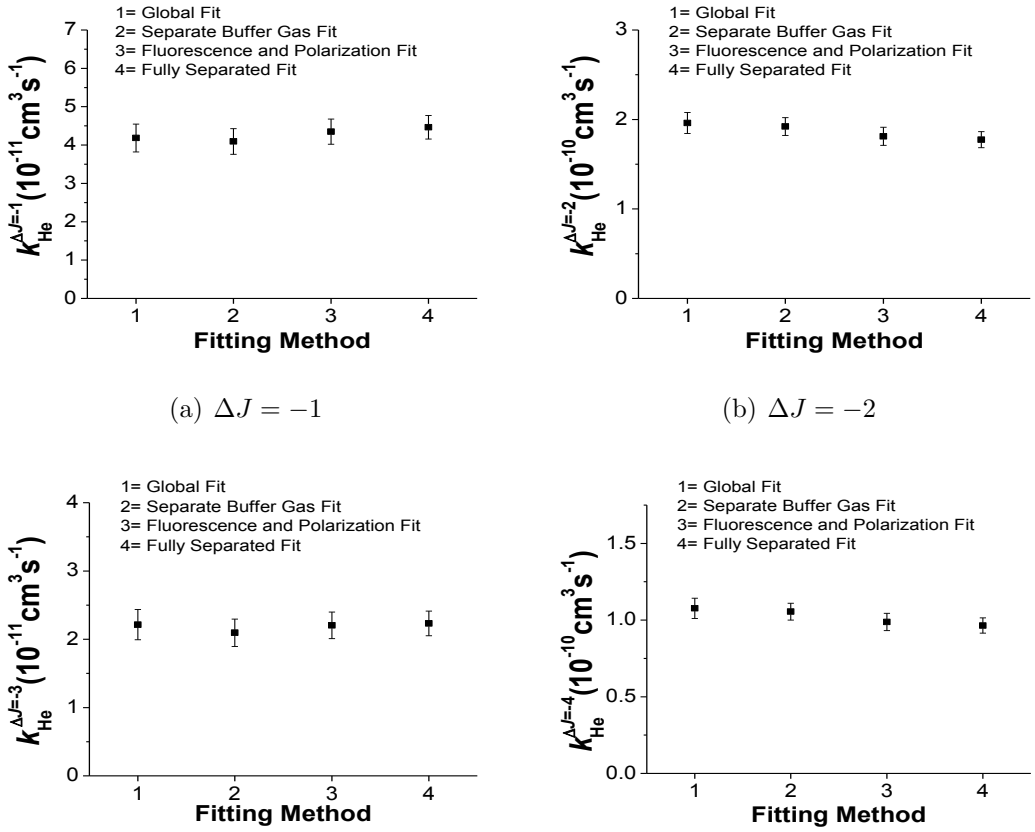

(a) $\Delta J = -1$

(b) $\Delta J = -2$

(c) $\Delta J = -3$

(d) $\Delta J = -4$

Figure 6.4: Plots of the fitted helium rate coefficients for negative ΔJ collisions for each of the described fitting methods.

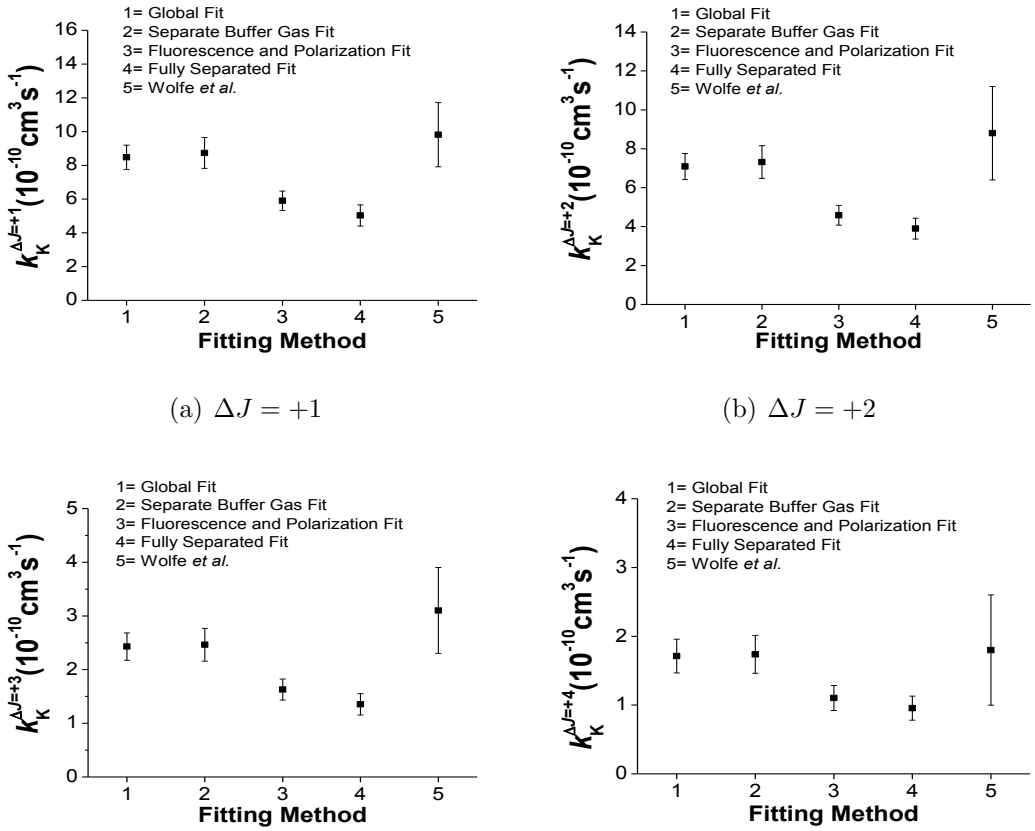

(a) $\Delta J = +1$

(b) $\Delta J = +2$

(c) $\Delta J = +3$

(d) $\Delta J = +4$

Figure 6.5: Plots of the fitted potassium rate coefficients for positive ΔJ collisions for each of the described fitting methods.

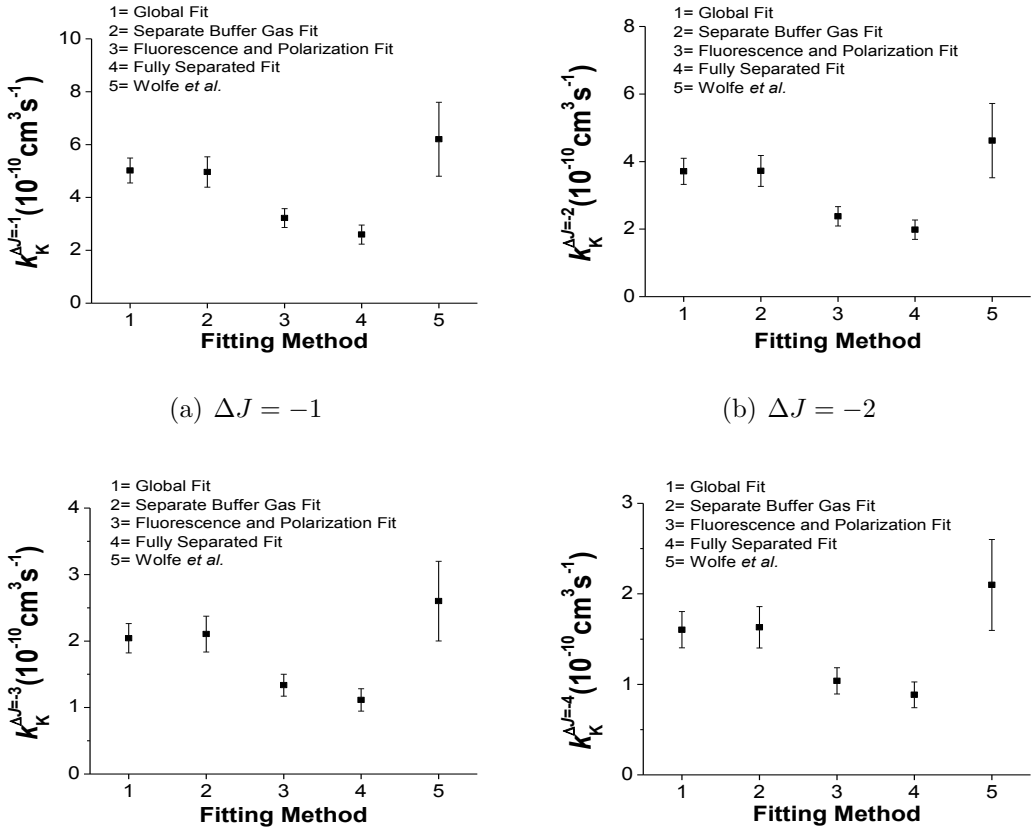

(a) $\Delta J = -1$

(b) $\Delta J = -2$

(c) $\Delta J = -3$

(d) $\Delta J = -4$

Figure 6.6: Plots of the fitted potassium rate coefficients for negative ΔJ collisions for each of the described fitting methods.

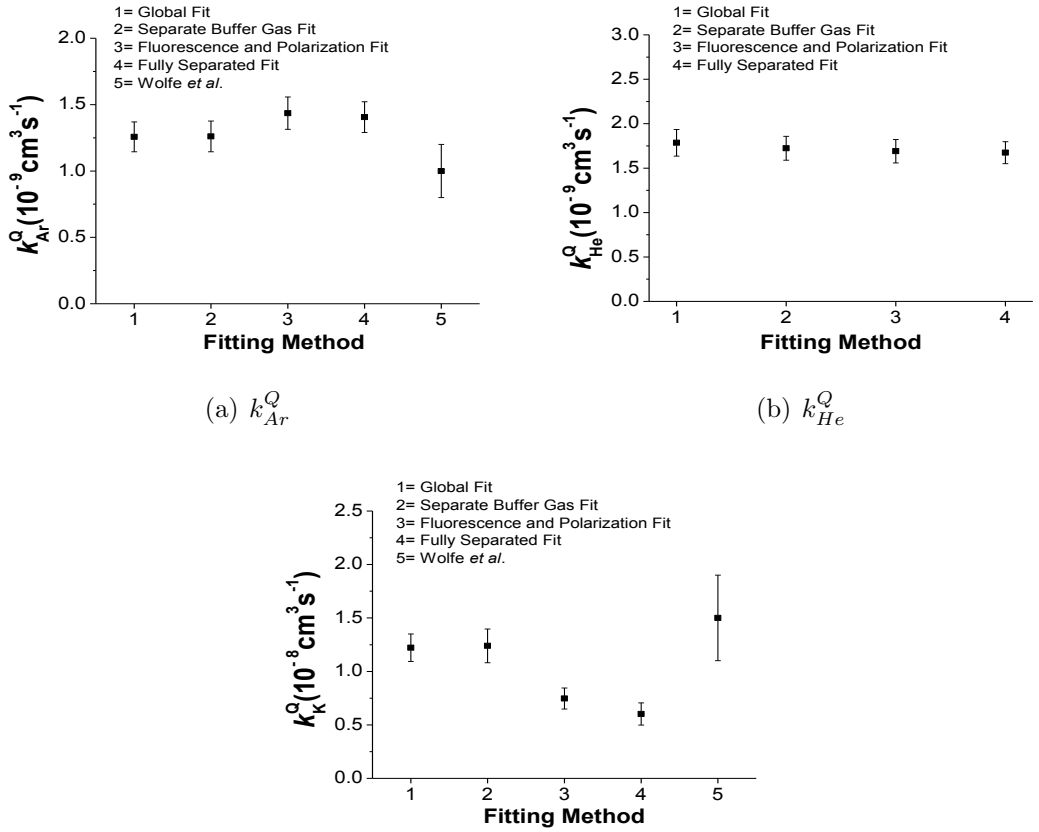

(a) k^Q_{Ar}

(b) k^Q_{He}

(c) k^Q_K

Figure 6.7: Plots of the fitted quenching rate coefficients for Ar in graph (a), He in graph (b), and K in graph (c) for each of the described fitting methods.

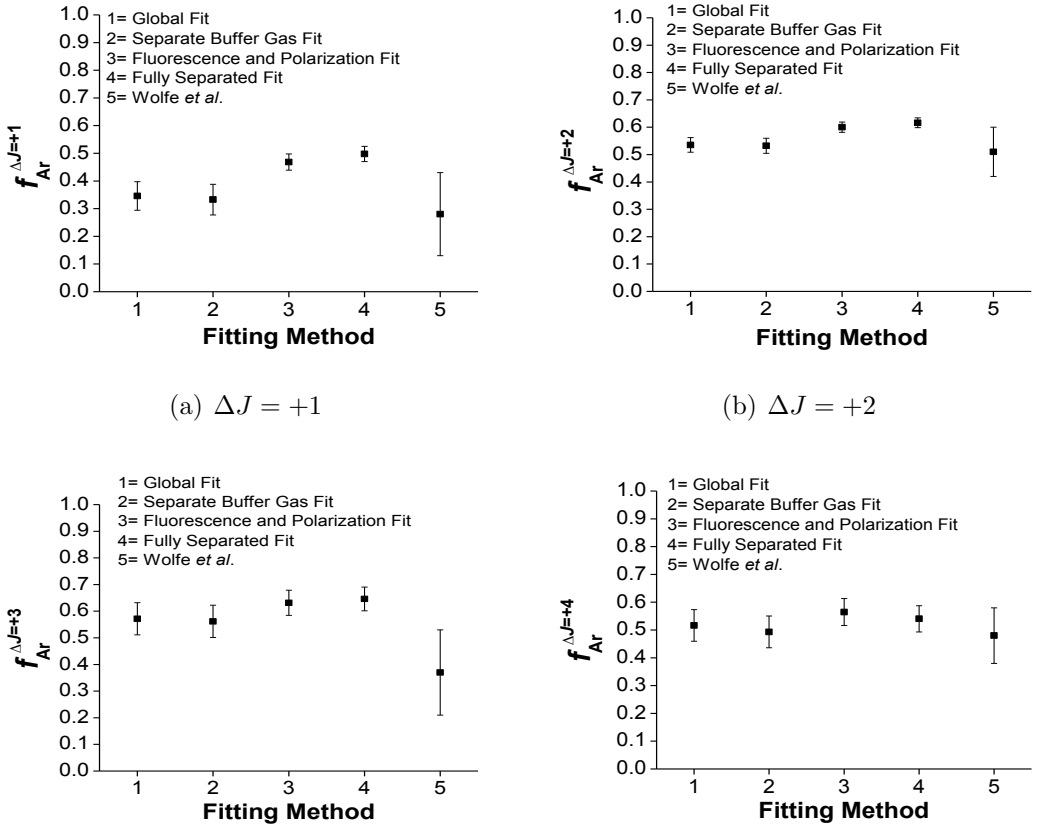

(a) $\Delta J = +1$

(b) $\Delta J = +2$

(c) $\Delta J = +3$

(d) $\Delta J = +4$

Figure 6.8: Plots of the fitted argon f values for positive ΔJ collisions obtained using each of the described fitting methods.

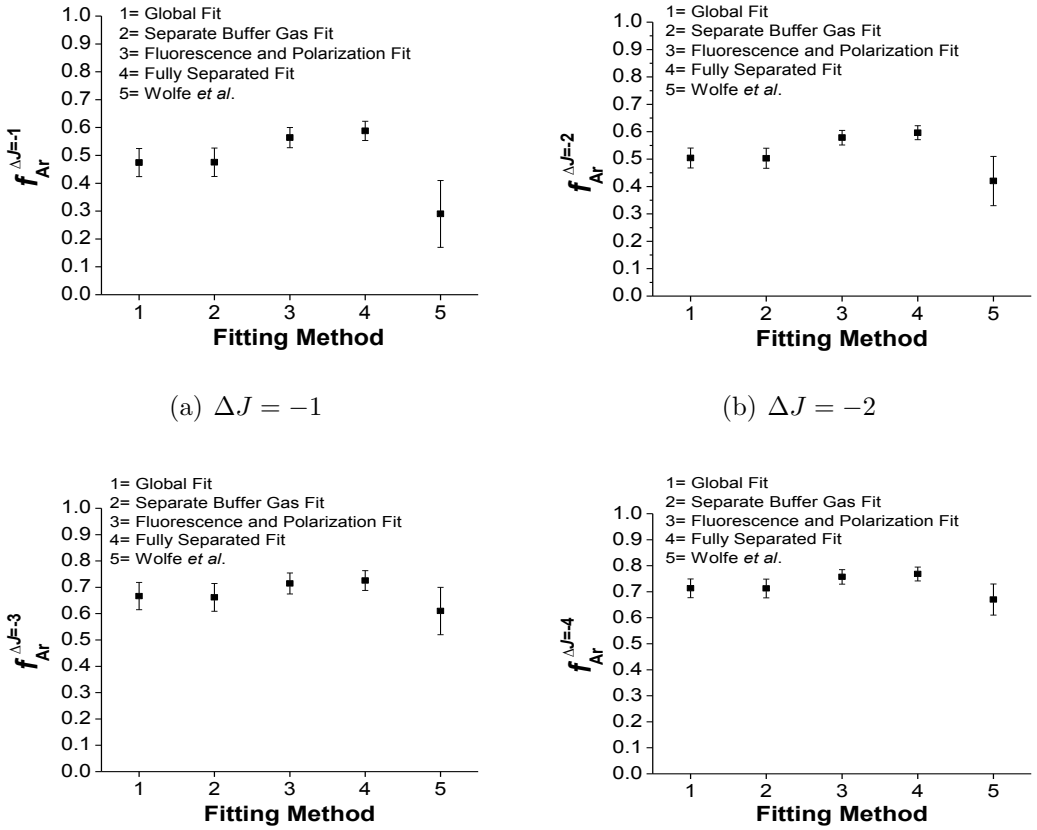

(a) $\Delta J = -1$

(b) $\Delta J = -2$

(c) $\Delta J = -3$

(d) $\Delta J = -4$

Figure 6.9: Plots of the fitted argon f values for negative ΔJ collisions for each of the described fitting methods.

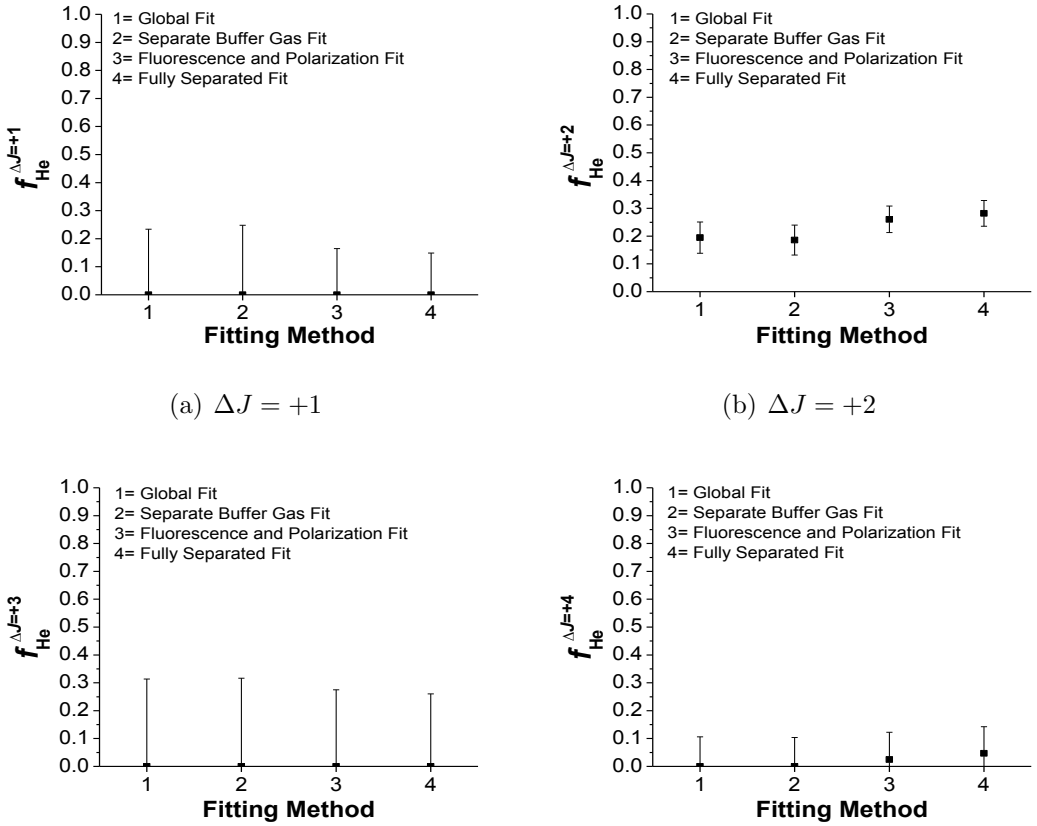

(a) $\Delta J = +1$

(b) $\Delta J = +2$

(c) $\Delta J = +3$

(d) $\Delta J = +4$

Figure 6.10: Plots of the fitted helium f values for positive ΔJ collisions for each of the described fitting methods.

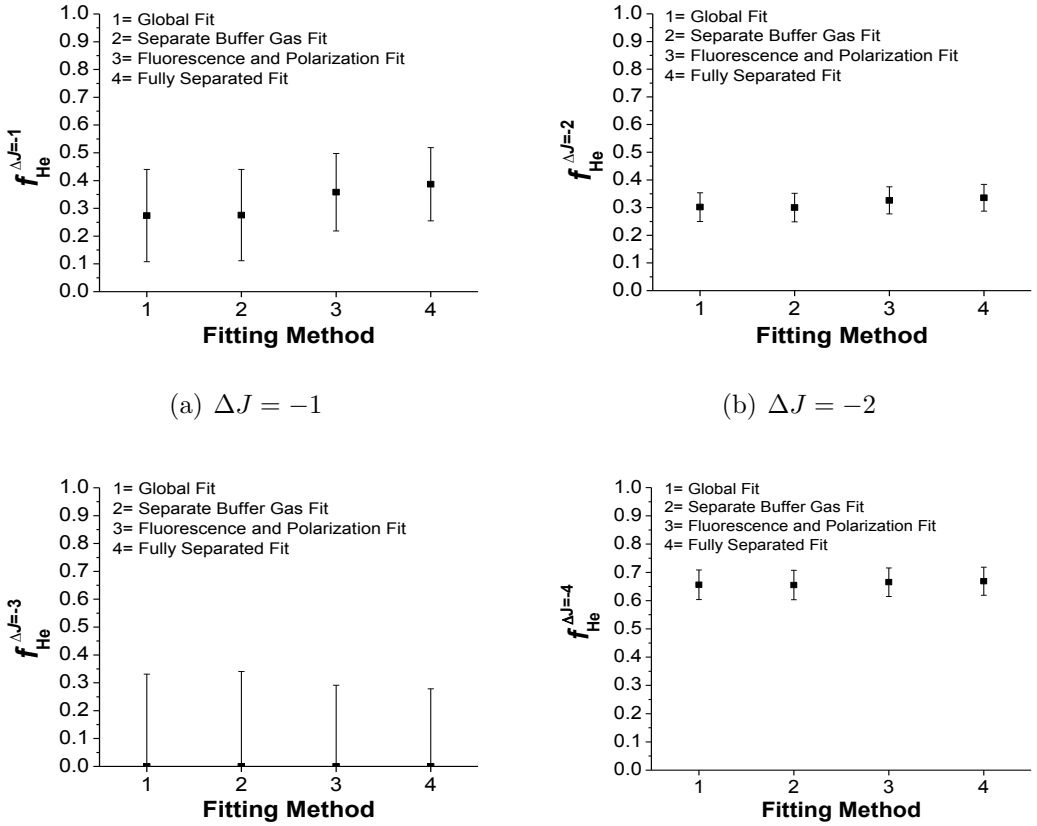

(a) $\Delta J = -1$

(b) $\Delta J = -2$

(c) $\Delta J = -3$

(d) $\Delta J = -4$

Figure 6.11: Plots of the fitted helium f values for negative ΔJ collisions for each of the described fitting methods.

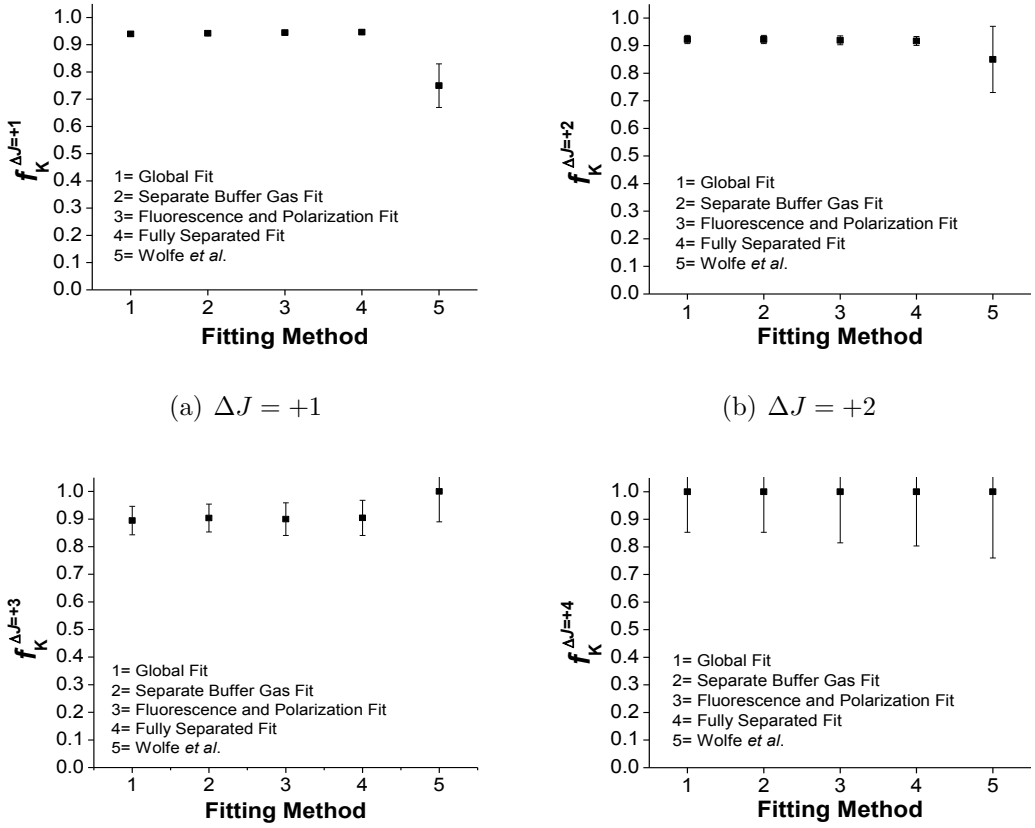

(a) $\Delta J = +1$

(b) $\Delta J = +2$

(c) $\Delta J = +3$

(d) $\Delta J = +4$

Figure 6.12: Plots of the fitted potassium f values for positive ΔJ collisions for each of the described fitting methods.

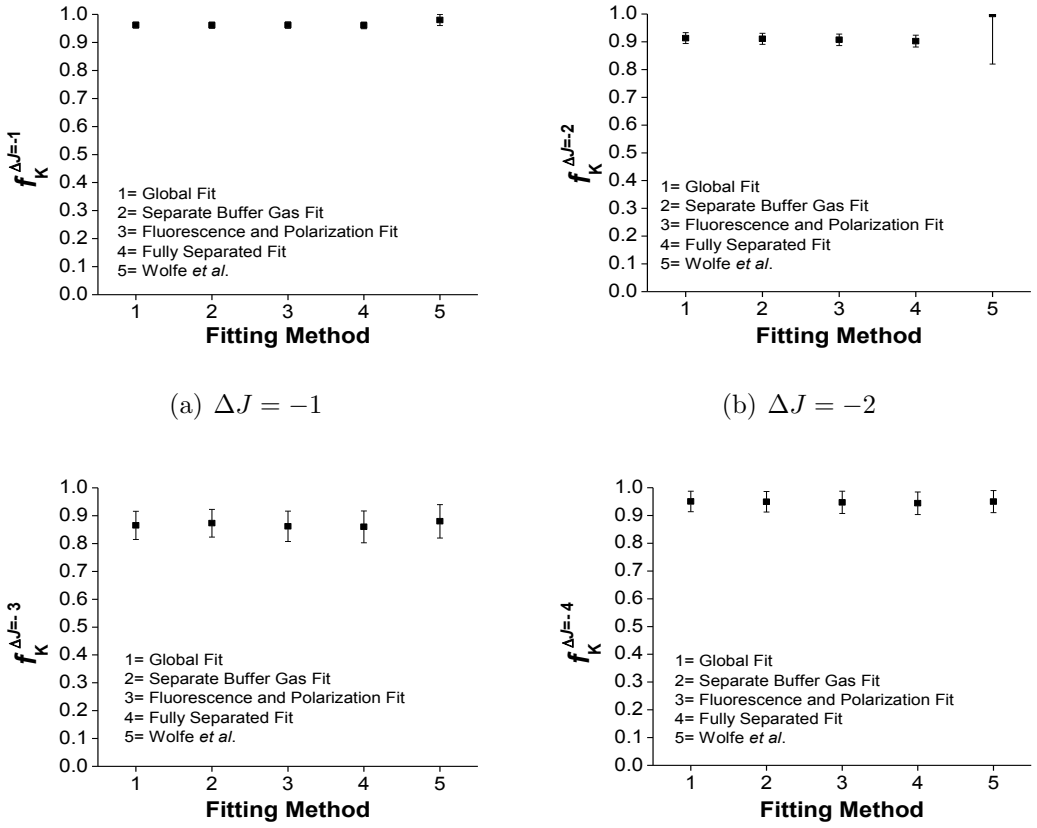

(a) $\Delta J = -1$

(b) $\Delta J = -2$

(c) $\Delta J = -3$

(d) $\Delta J = -4$

Figure 6.13: Plots of the fitted potassium f values for negative ΔJ collisions for each of the described fitting methods.

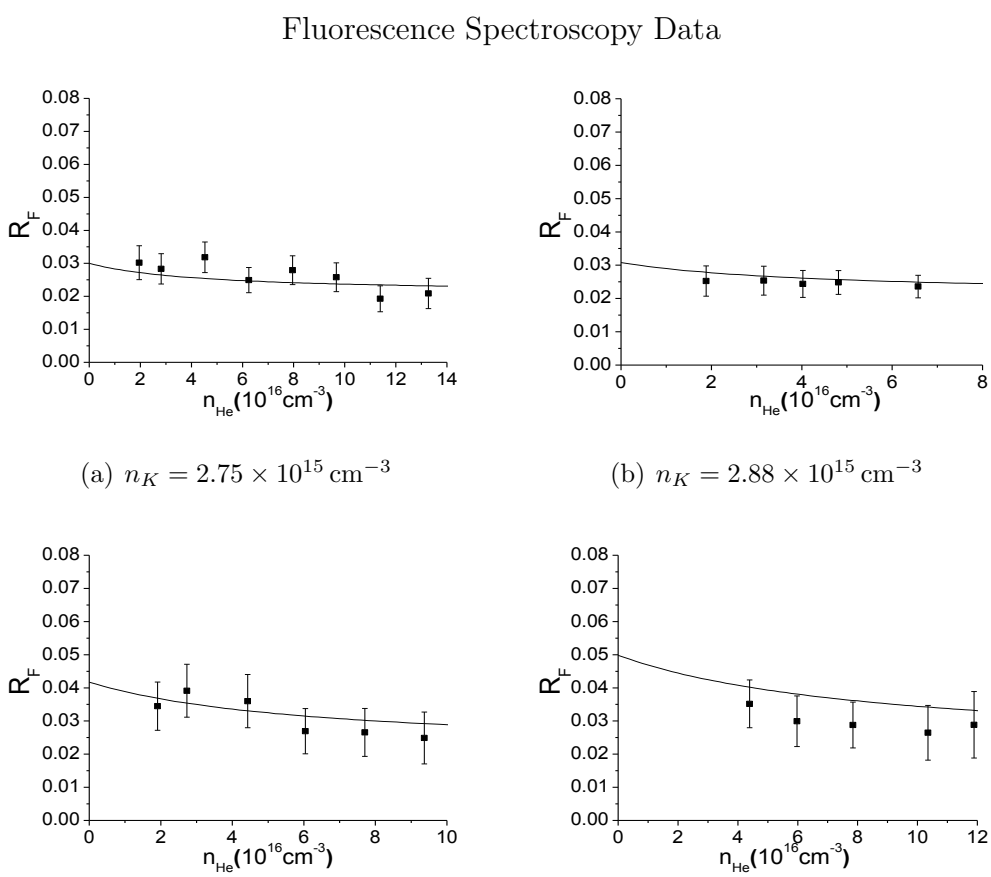

(a) $n_K = 2.75 \times 10^{15}\,\mathrm{cm}^{-3}$

(b) $n_K = 2.88 \times 10^{15}\,\mathrm{cm}^{-3}$

(c) $n_K = 5.44 \times 10^{15}\,\mathrm{cm}^{-3}$

(d) $n_K = 9.2 \times 10^{15}\,\mathrm{cm}^{-3}$

Figure 6.14: Plots of fluorescence ratio data (R_F) versus helium density for $\Delta J = +1$ collisions of NaK $2(A)^1\Sigma^+(16, 30)$ molecules with helium and potassium perturbers. Each panel represents a fixed potassium density n_K. In this, and subsequent plots, the calculated R_F values (solid curves) were obtained using the global fit parameters.

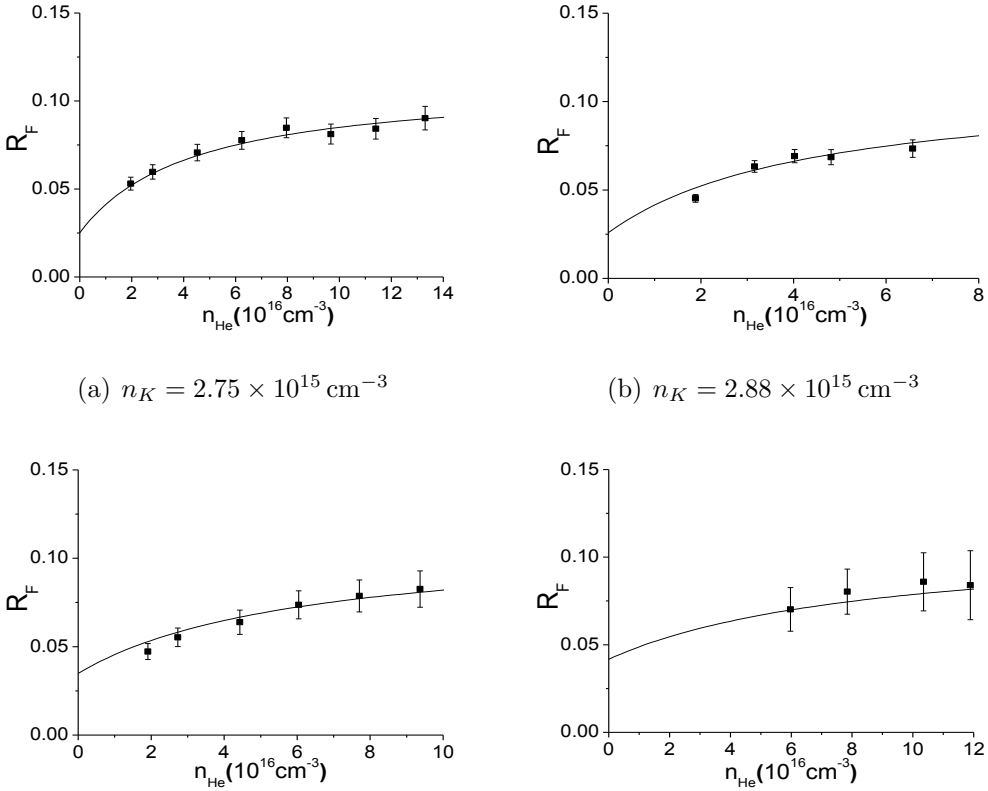

(a) $n_K = 2.75 \times 10^{15}\,\mathrm{cm}^{-3}$

(b) $n_K = 2.88 \times 10^{15}\,\mathrm{cm}^{-3}$

(c) $n_K = 5.44 \times 10^{15}\,\mathrm{cm}^{-3}$

(d) $n_K = 9.2 \times 10^{15}\,\mathrm{cm}^{-3}$

Figure 6.15: Plots of fluorescence ratio data (R_F) versus helium density for $\Delta J = +2$ collisions of NaK $2(A)^1\Sigma^+(16, 30)$ molecules with helium and potassium perturbers. Each panel represents a fixed potassium density n_K.

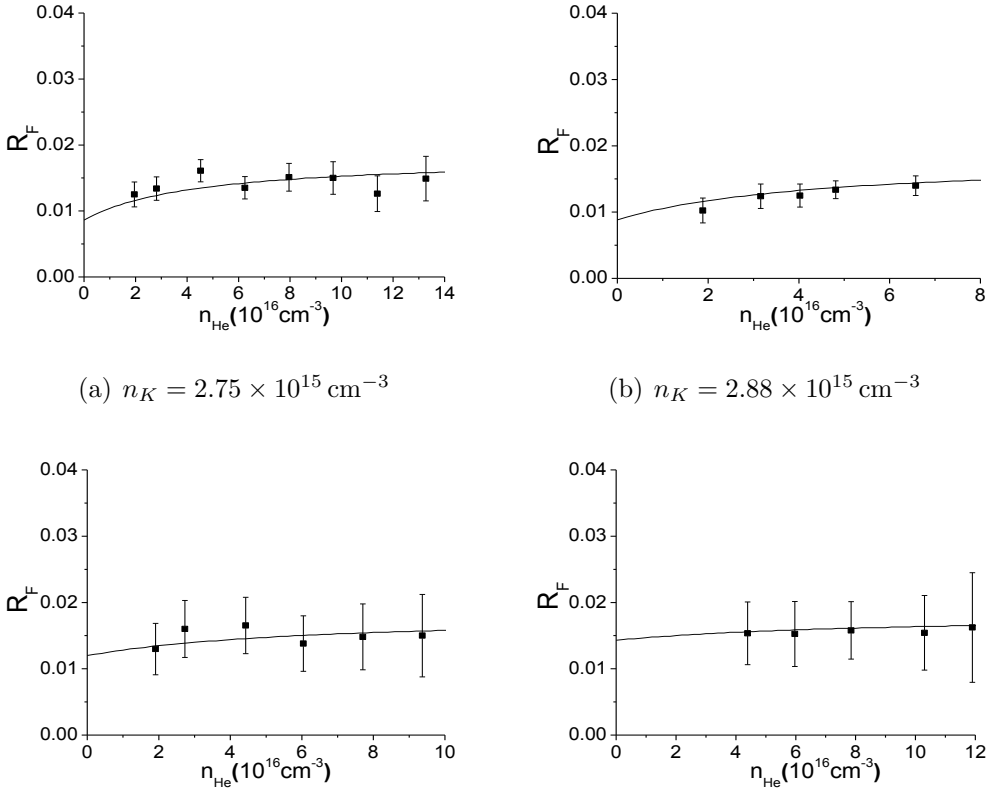

(a) $n_K = 2.75 \times 10^{15}\,\mathrm{cm}^{-3}$

(b) $n_K = 2.88 \times 10^{15}\,\mathrm{cm}^{-3}$

(c) $n_K = 5.44 \times 10^{15}\,\mathrm{cm}^{-3}$

(d) $n_K = 9.2 \times 10^{15}\,\mathrm{cm}^{-3}$

Figure 6.16: Plots of fluorescence ratio data (R_F) versus helium density for $\Delta J = +3$ collisions of NaK $2(A)^1\Sigma^+(16, 30)$ molecules with helium and potassium perturbers. Each panel represents a fixed potassium density n_K.

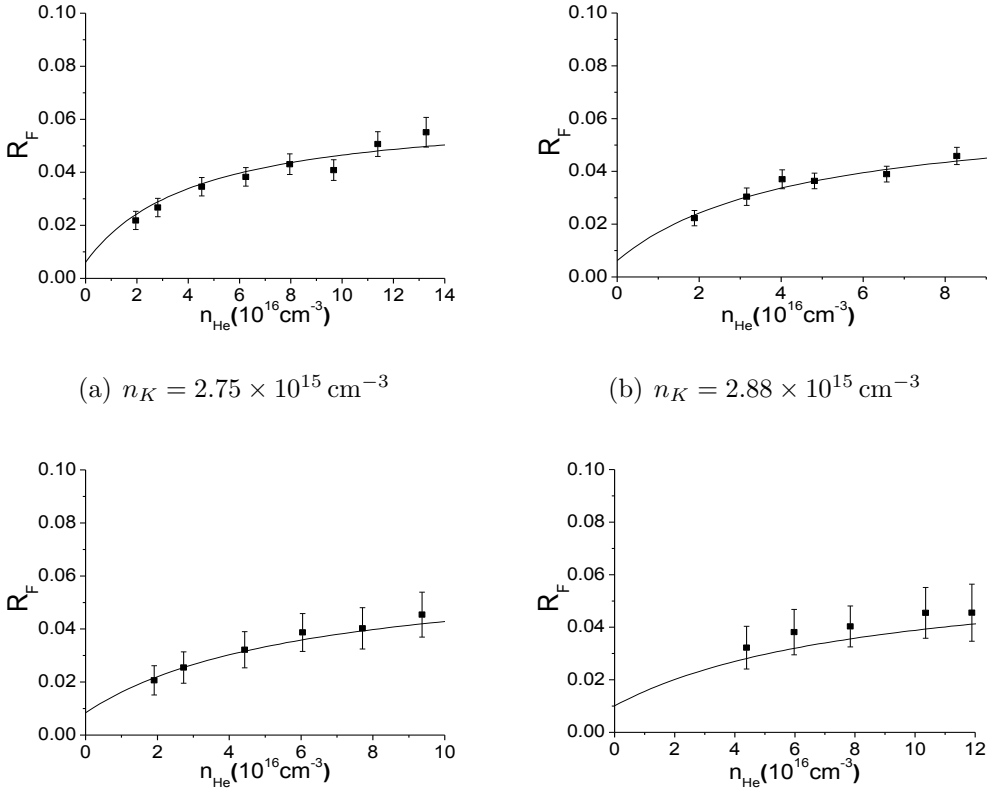

(a) $n_K = 2.75 \times 10^{15}\,\mathrm{cm}^{-3}$

(b) $n_K = 2.88 \times 10^{15}\,\mathrm{cm}^{-3}$

(c) $n_K = 5.44 \times 10^{15}\,\mathrm{cm}^{-3}$

(d) $n_K = 9.2 \times 10^{15}\,\mathrm{cm}^{-3}$

Figure 6.17: Plots of fluorescence ratio data (R_F) versus helium density for $\Delta J = +4$ collisions of NaK $2(A)^1\Sigma^+(16, 30)$ molecules with helium and potassium perturbers. Each panel represents a fixed potassium density n_K.

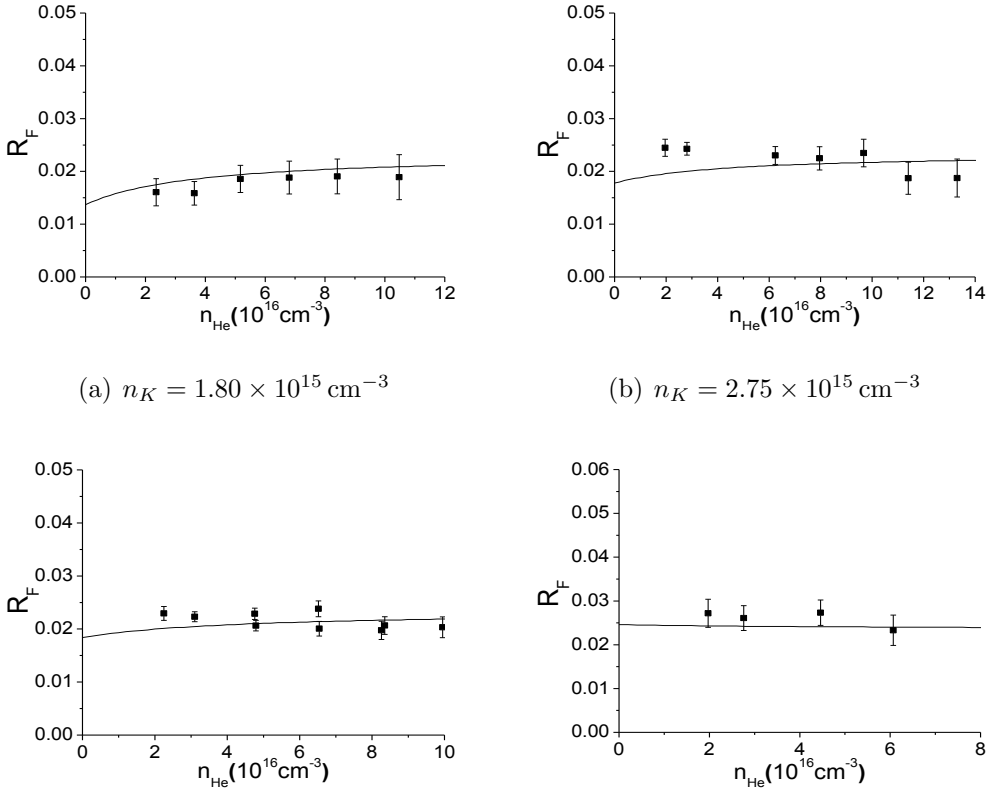

(a) $n_K = 1.80 \times 10^{15}\,\mathrm{cm}^{-3}$

(b) $n_K = 2.75 \times 10^{15}\,\mathrm{cm}^{-3}$

(c) $n_K = 2.92 \times 10^{15}\,\mathrm{cm}^{-3}$

(d) $n_K = 5.37 \times 10^{15}\,\mathrm{cm}^{-3}$

Figure 6.18: Plots of fluorescence ratio data (R_F) versus helium density for $\Delta J = -1$ collisions of NaK $2(A)^1\Sigma^+(16, 30)$ molecules with helium and potassium perturbers. Each panel represents a fixed potassium density n_K.

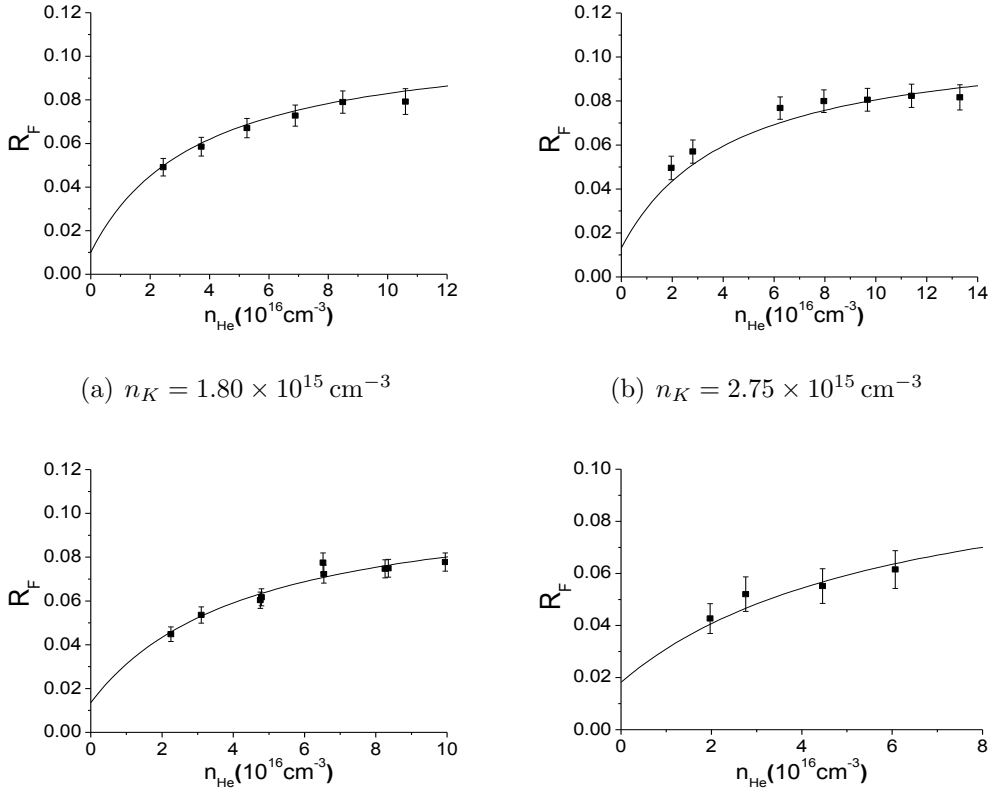

(a) $n_K = 1.80 \times 10^{15}\,\mathrm{cm}^{-3}$ (b) $n_K = 2.75 \times 10^{15}\,\mathrm{cm}^{-3}$

(c) $n_K = 2.92 \times 10^{15}\,\mathrm{cm}^{-3}$ (d) $n_K = 5.37 \times 10^{15}\,\mathrm{cm}^{-3}$

Figure 6.19: Plots of fluorescence ratio data (R_F) versus helium density for $\Delta J = -2$ collisions of NaK $2(A)^1\Sigma^+(16, 30)$ molecules with helium and potassium perturbers. Each panel represents a fixed potassium density n_K.

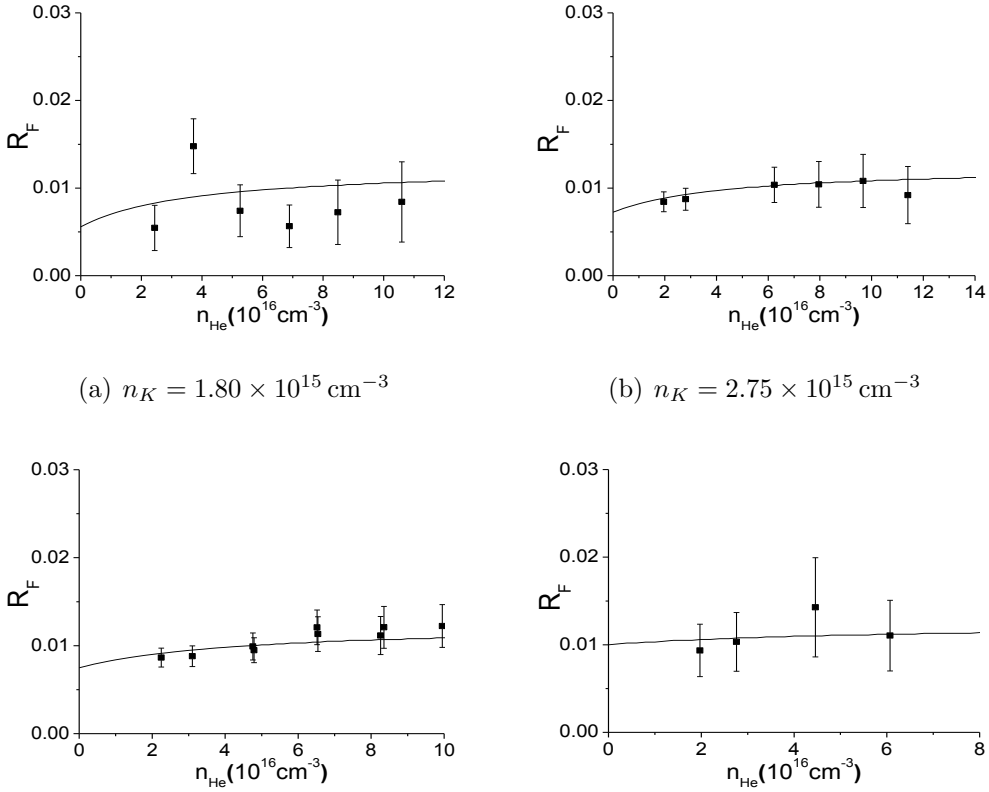

(a) $n_K = 1.80 \times 10^{15}\,\mathrm{cm}^{-3}$

(b) $n_K = 2.75 \times 10^{15}\,\mathrm{cm}^{-3}$

(c) $n_K = 2.92 \times 10^{15}\,\mathrm{cm}^{-3}$

(d) $n_K = 5.37 \times 10^{15}\,\mathrm{cm}^{-3}$

Figure 6.20: Plots of fluorescence ratio data (R_F) versus helium density for $\Delta J = -3$ collisions of NaK $2(A)^1\Sigma^+(16, 30)$ molecules with helium and potassium perturbers. Each panel represents a fixed potassium density n_K.

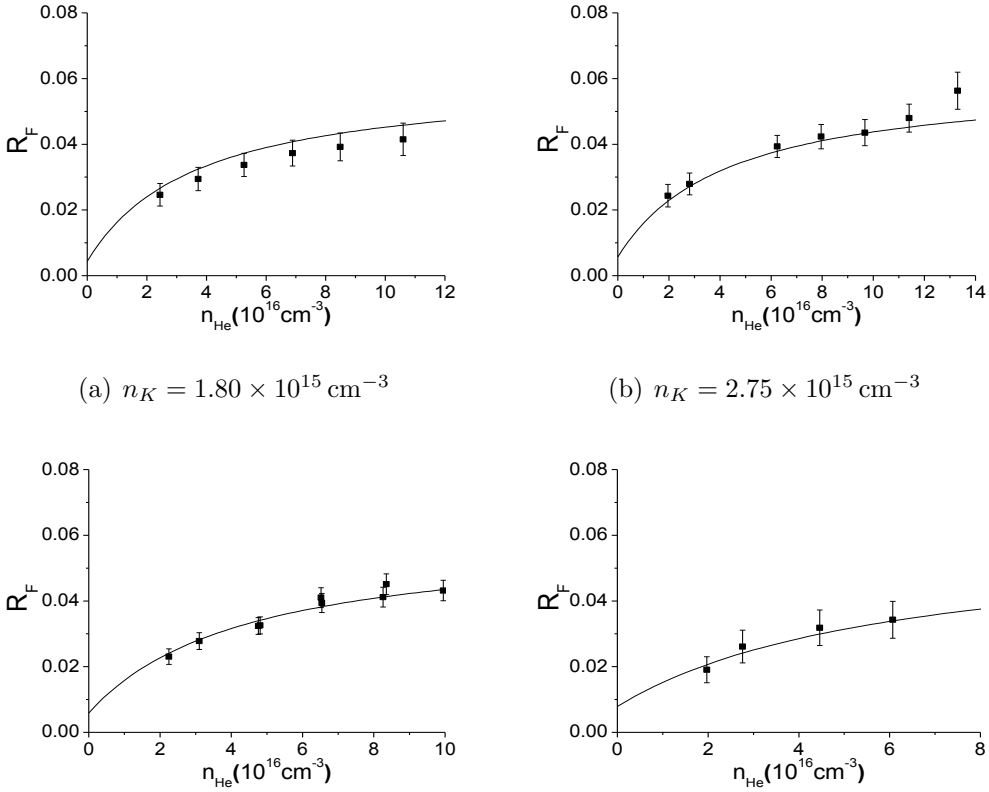

(a) $n_K = 1.80 \times 10^{15}\,\mathrm{cm}^{-3}$

(b) $n_K = 2.75 \times 10^{15}\,\mathrm{cm}^{-3}$

(c) $n_K = 2.92 \times 10^{15}\,\mathrm{cm}^{-3}$

(d) $n_K = 5.37 \times 10^{15}\,\mathrm{cm}^{-3}$

Figure 6.21: Plots of fluorescence ratio data (R_F) versus helium density for $\Delta J = -4$ collisions of NaK $2(A)^1\Sigma^+(16, 30)$ molecules with helium and potassium perturbers. Each panel represents a fixed potassium density n_K.

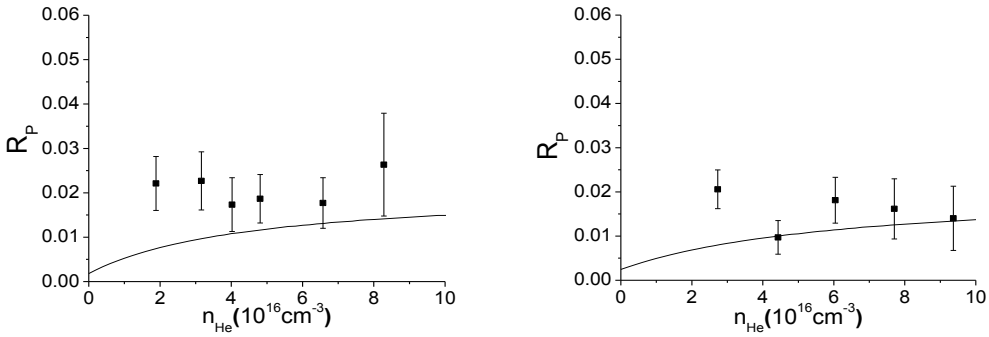

(a) $n_K = 1.80 \times 10^{15}\,\mathrm{cm}^{-3}$ (b) $n_K = 5.37 \times 10^{15}\,\mathrm{cm}^{-3}$

Figure 6.22: Plots of polarization ratio data (R_P) versus helium density for $\Delta J = +1$ collisions of NaK $2(A)^1\Sigma^+(16, 30)$ molecules with helium and potassium perturbers. Each panel represents a fixed potassium density n_K. In this, and subsequent plots, the calculated R_P (solid curves) were obtained using the global fit parameters.

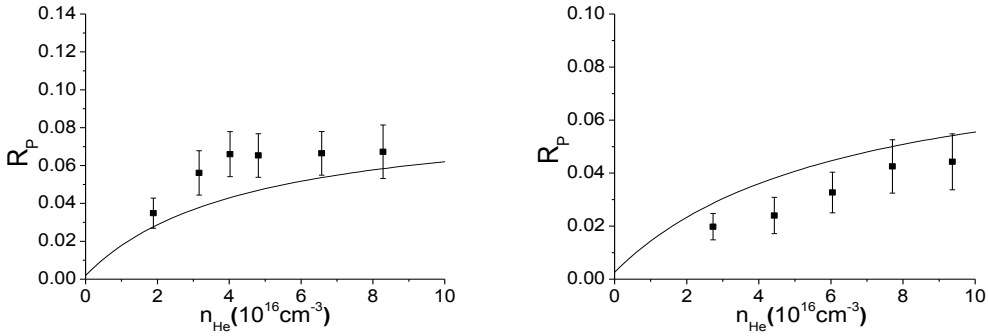

(a) $n_K = 1.80 \times 10^{15}\,\mathrm{cm}^{-3}$ (b) $n_K = 5.37 \times 10^{15}\,\mathrm{cm}^{-3}$

Figure 6.23: Plots of polarization ratio data (R_P) versus helium density for $\Delta J = +2$ collisions of NaK $2(A)^1\Sigma^+(16, 30)$ molecules with helium and potassium perturbers. Each panel represents a fixed potassium density n_K.

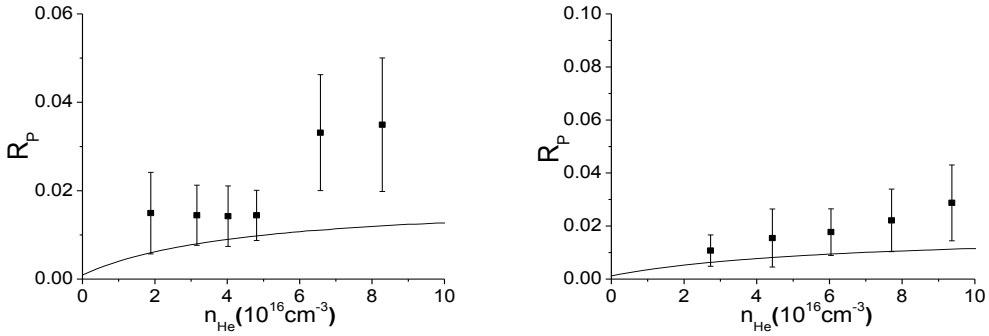

(a) $n_K = 1.80 \times 10^{15}\,\mathrm{cm}^{-3}$ (b) $n_K = 5.37 \times 10^{15}\,\mathrm{cm}^{-3}$

Figure 6.24: Plots of polarization ratio data (R_P) versus helium density for $\Delta J = +3$ collisions of NaK $2(A)^1\Sigma^+(16, 30)$ molecules with helium and potassium perturbers. Each panel represents a fixed potassium density n_K.

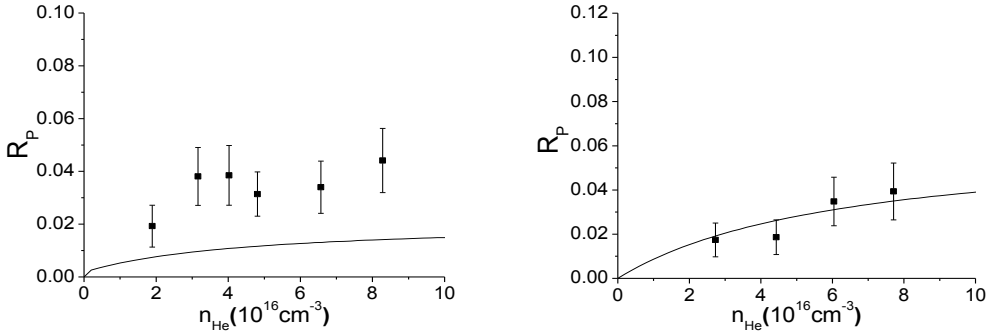

(a) $n_K = 1.80 \times 10^{15}\,\mathrm{cm}^{-3}$ (b) $n_K = 5.37 \times 10^{15}\,\mathrm{cm}^{-3}$

Figure 6.25: Plots of polarization ratio data (R_P) versus helium density for $\Delta J = +4$ collisions of NaK $2(A)^1\Sigma^+(16, 30)$ molecules with helium and potassium perturbers. Each panel represents a fixed potassium density n_K.

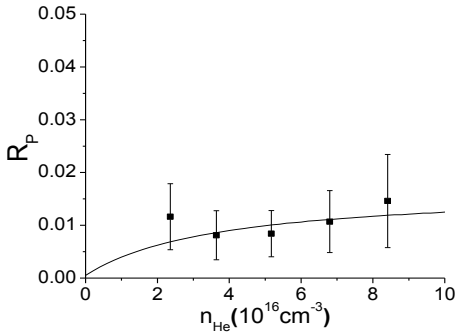

(a) $n_K = 1.80 \times 10^{15}\,\mathrm{cm}^{-3}$

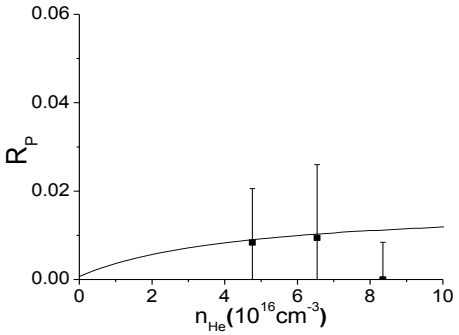

(b) $n_K = 2.92 \times 10^{15}\,\mathrm{cm}^{-3}$

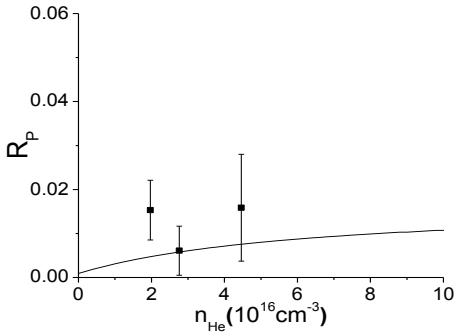

(c) $n_K = 5.37 \times 10^{15}\,\mathrm{cm}^{-3}$

Figure 6.26: Plots of polarization ratio data (R_P) versus helium density for $\Delta J = -1$ collisions of NaK $2(A)^1\Sigma^+(16, 30)$ molecules with helium and potassium perturbers. Each panel represents a fixed potassium density n_K.

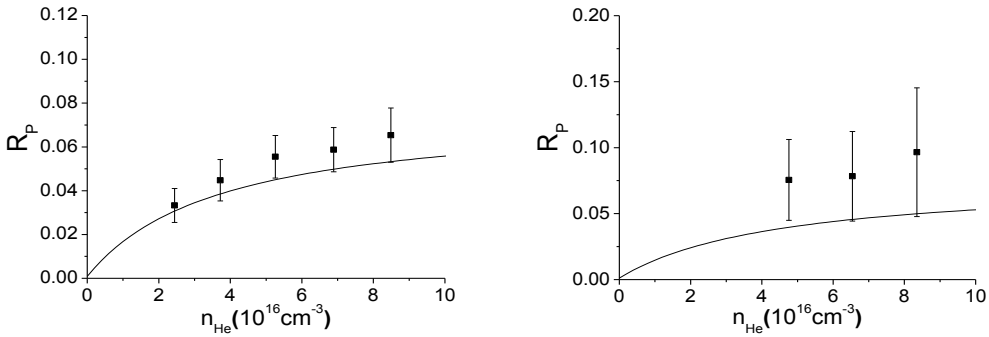

(a) $n_K = 1.80 \times 10^{15}\,\mathrm{cm}^{-3}$

(b) $n_K = 2.92 \times 10^{15}\,\mathrm{cm}^{-3}$

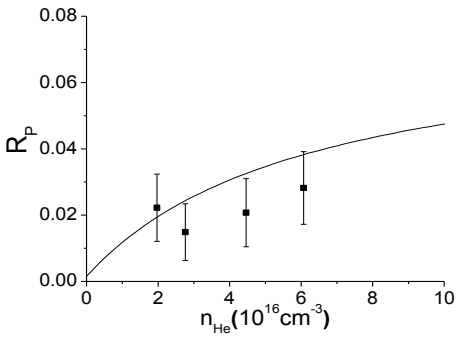

(c) $n_K = 5.37 \times 10^{15}\,\mathrm{cm}^{-3}$

Figure 6.27: Plots of polarization ratio data (R_P) versus helium density for $\Delta J = -2$ collisions of NaK $2(A)^1\Sigma^+(16, 30)$ molecules with helium and potassium perturbers. Each panel represents a fixed potassium density n_K.

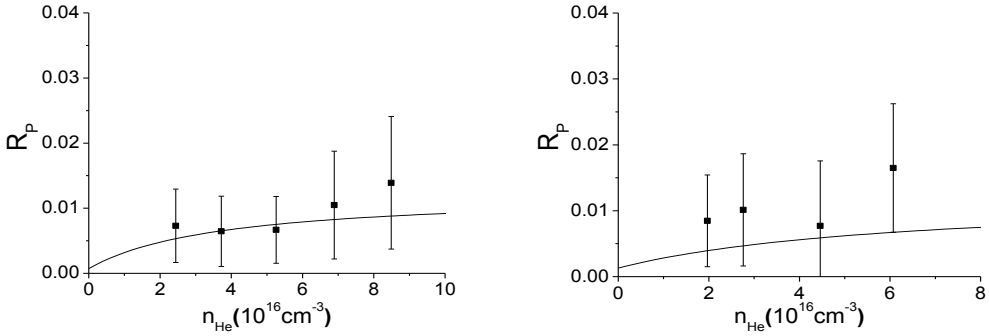

(a) $n_K = 1.80 \times 10^{15}\,\mathrm{cm}^{-3}$ (b) $n_K = 5.37 \times 10^{15}\,\mathrm{cm}^{-3}$

Figure 6.28: Plots of polarization ratio data (R_P) versus helium density for $\Delta J = -3$ collisions of NaK $2(A)^1\Sigma^+(16, 30)$ molecules with helium and potassium perturbers. Each panel represents a fixed potassium density n_K.

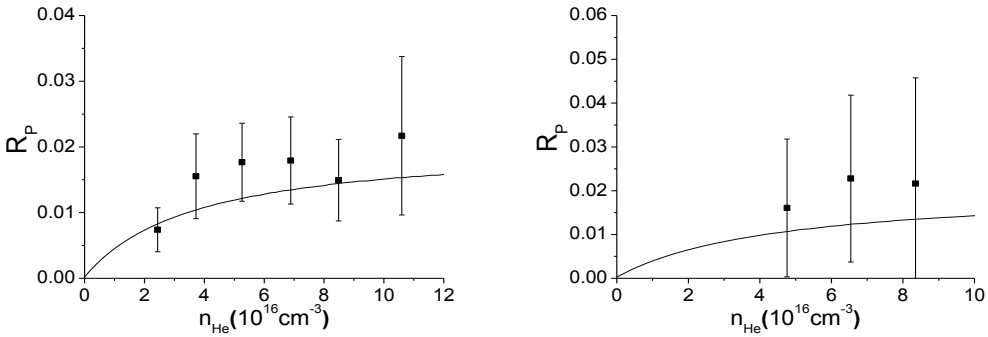

(a) $n_K = 1.80 \times 10^{15}\,\mathrm{cm}^{-3}$

(b) $n_K = 2.92 \times 10^{15}\,\mathrm{cm}^{-3}$

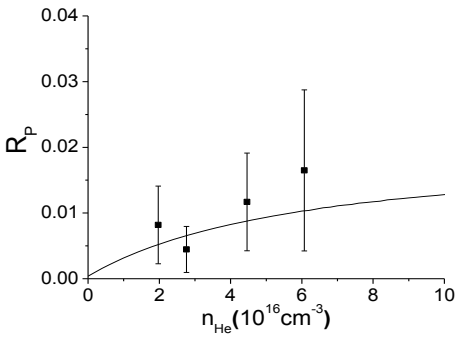

(c) $n_K = 5.37 \times 10^{15}\,\mathrm{cm}^{-3}$

Figure 6.29: Plots of polarization ratio data (R_P) versus helium density for $\Delta J = -4$ collisions of NaK $2(A)^1\Sigma^+(16, 30)$ molecules with helium and potassium perturbers. Each panel represents a fixed potassium density n_K.

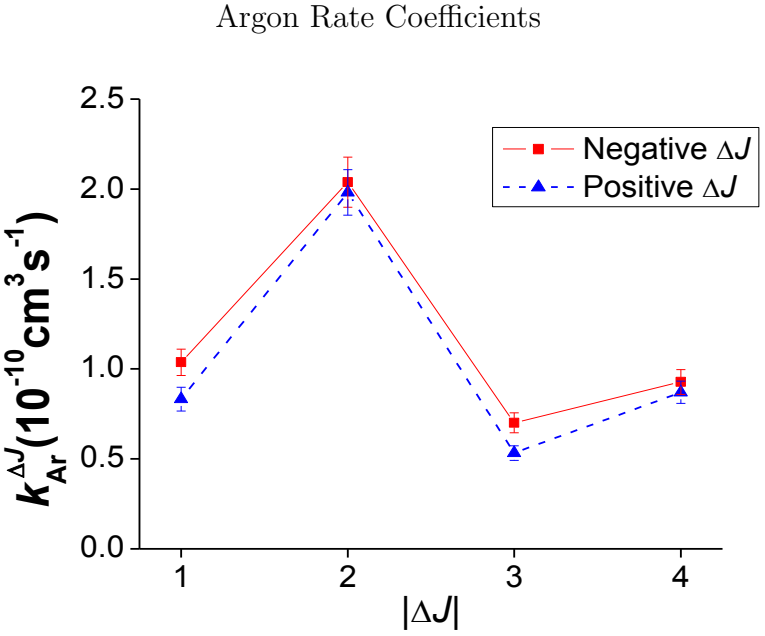

Figure 6.30: Plot of the fitted rate coefficients, $k_{Ar}^{\Delta J}$, for collisions of argon with NaK $2(A)^1\Sigma^+(16, 30)$ using the global fit parameters of the data obtained in this work and in the work of Wolfe *et al.* [30].

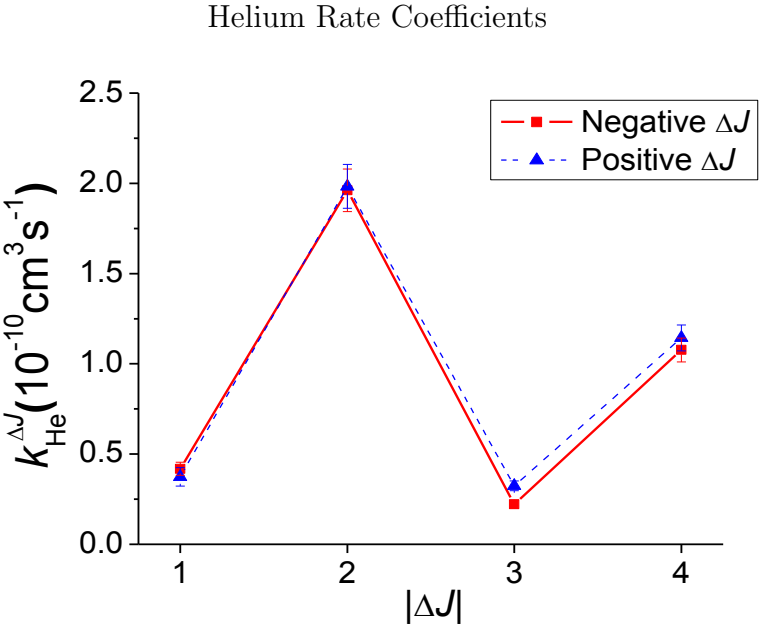

Figure 6.31: Plots of the fitted rate coefficients, $k_{He}^{\Delta J}$, for collisions of helium with NaK $2(A)^1\Sigma^+(16, 30)$ using the global fit parameters of the data obtained in this work.

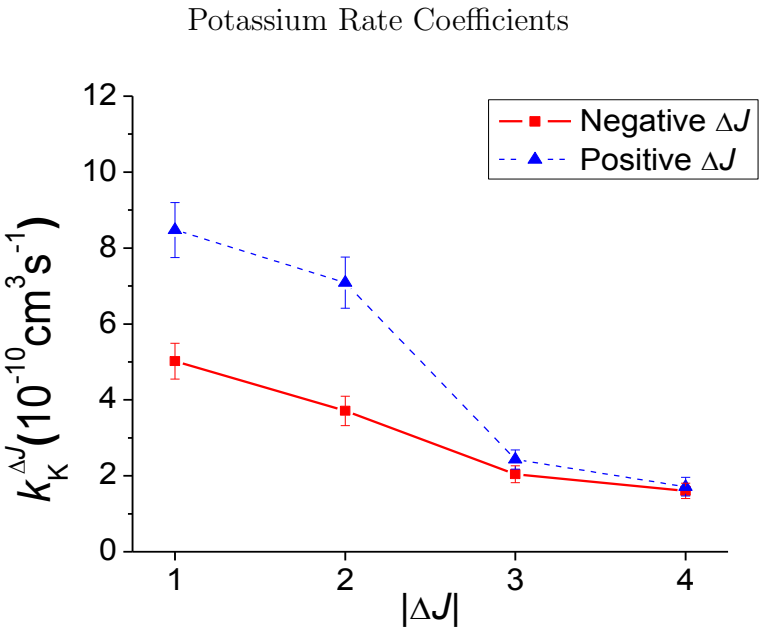

Figure 6.32: Plot of the fitted rate coefficients, $k_K^{\Delta J}$, for collisions of potassium with NaK $2(A)^1\Sigma^+(16, 30)$ using the global fit parameters of the data obtained in this work and in the work of Wolfe *et al.* [30].

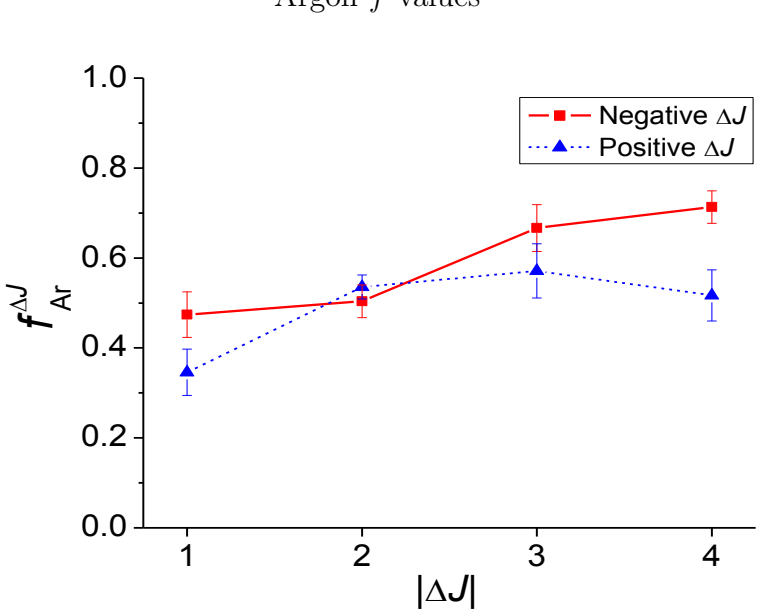

Figure 6.33: Plot of the fitted fraction of orientation destroyed, $f_{Ar}^{\Delta J}$, for rotationally inelastic collisions of argon with NaK $2(A)^1\Sigma^+(16, 30)$ using the global fit parameters of the data obtained in this work and in the work of Wolfe *et al.* [30].

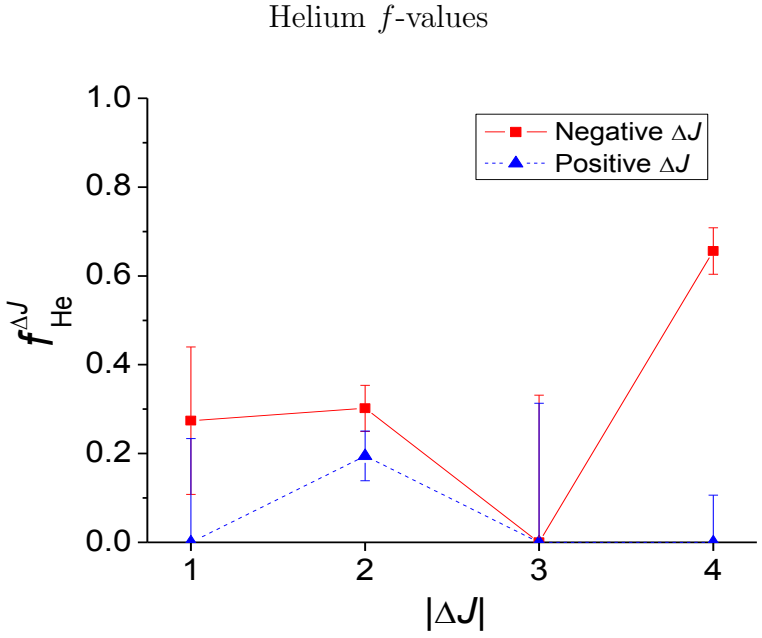

Figure 6.34: Plot of the fitted fraction of orientation destroyed, $f_{He}^{\Delta J}$, for rotationally inelastic collisions of helium with NaK $2(A)^1\Sigma^+(16, 30)$ using the global fit parameters of the data obtained in this work.

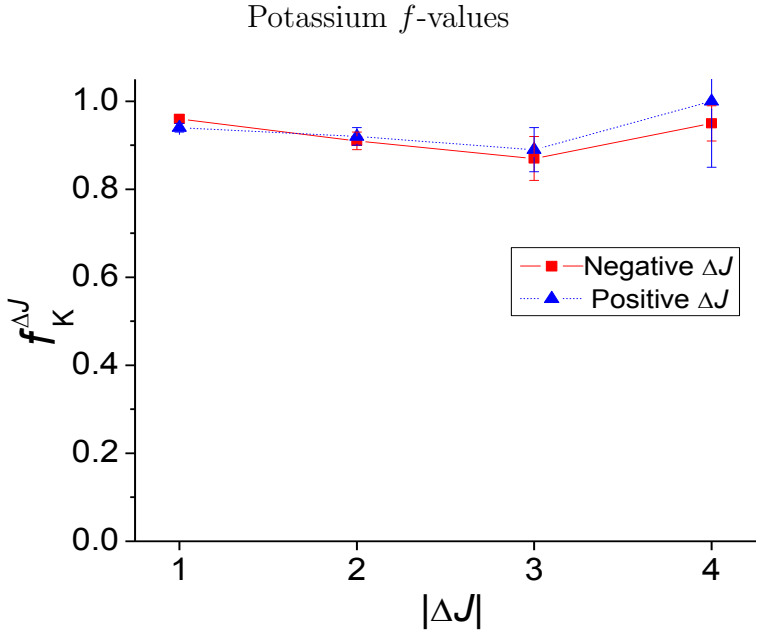

Figure 6.35: Plot of the fitted fraction of orientation destroyed, $f_K^{\Delta J}$, for rotationally inelastic collisions of potassium with NaK $2(A)^1\Sigma^+(16, 30)$ using the global fit parameters of the data obtained in this work and in the work of Wolfe *et al.* [30].

Considering the various ΔJ collisions, the ΔJ = even parameters are the best determined of the helium (and argon) rate coefficients and particularly the f values. The f values for ΔJ = odd collisions have large uncertainties, especially for helium. Since the polarization signal is dependent on the population times orientation [see Eq. (3.37)], a combination of a small collisional rate coefficient for population transfer of NaK-He for ΔJ = odd (i.e., small population in the collisional level) coupled with the fact that potassium, despite a much larger population transfer rate coefficient than the noble gases, destroys essentially all orientation during a collision, results in small polarization signals relative to the noise. This results in large uncertainties in the R_P values, especially for the ΔJ = odd population and orientation parameters.

6.6 NaCs Population Transfer

As a comparison to the NaK rotationally inelastic collisional population transfer studies, we also collected R_F data on collisions of NaCs molecules with argon and helium perturbers. We have carried out a series of fits of the R_F data for the NaCs-Ar collision experiment using all available fluorescence data and we call these "fluorescence fits". The most important result of this experiment is that no ΔJ = even propensity is observed for NaCs-Ar collisions. Additionally, we have taken some preliminary data using helium as a perturber to see if we notice a ΔJ = even propensity for these NaCs-He rotationally inelastic collisions.

We obtained values for the NaCs rate coefficients $k_{Ar}^{\Delta J}$ and $k_{Cs}^{\Delta J}$ for each ΔJ and the quenching rate, k_{Ar}^{Q}, using the measured R_F values and Eq. (3.6). Letting all of the rate coefficient parameters vary in the fit (with the general constraint that all parameters be positive), we obtain unphysical values $k_{Cs}^{\Delta J=+1}/\Gamma = 0$ and $k_{Cs}^{Q}/\Gamma \sim 2 \times 10^{-17}\,\mathrm{cm}^3$. These values are certainly unphysical since this would imply there is zero cross-section for rotationally inelastic collisions for NaCs $2(A)^1\Sigma^+(14, 32)$-Cs that change J by one and that the cross-section for quenching collisions is very much smaller than expected. However, we believe these anomalous

results are due to the fact that we don't have data from a regime where we are most sensitive to measuring cesium collisions (such as data taken in "heat pipe" mode). Thus cesium rate coefficients are difficult to determine from our current data set and have large error bars (i.e., the error bar on the cesium quenching value is $\sim 100\%$).

In light of this fact, we carried out a series of fits with k^Q_{Cs}/Γ fixed to various values over a broad range consistent with our measurement of k^Q_K/Γ. We believe the quenching rate coefficients for potassium in the NaK experiment and for cesium in the NaCs experiment should be comparable in magnitude. With k^Q_{Cs}/Γ fixed to any value between $1.0\times^{-16}$ cm^3 and $1.0\times^{-15}$ cm^3 we find that the fitted value of $k^{\Delta J=+1}_{Cs}$ is non-zero and reasonable. In this test, we determined that fixing k^Q_{Cs}/Γ to almost any reasonable value, and even setting it to zero or letting it vary in the fit has little effect on the argon rate coefficients. Comparisons of these results are presented in Figs. 6.36(a) and 6.36(b) for argon and cesium rate coefficients, respectively. Note that the $k^{\Delta J}_{Cs}$ values essentially scale with k^Q_{Cs}. Therefore the cesium rate coefficients are plotted in 6.36(b) in the form $k^{\Delta J}_{Cs}/k^Q_{Cs}$.

The rate coefficients determined from the various fits with fixed values of k^Q_{Cs}/Γ and also with k^Q_{Cs}/Γ allowed to vary are presented in Tables 6.9 through 6.15. We believe that the most reliable values are obtained with $k^Q_{Cs}/\Gamma = 3.0\times10^{-16}\,\mathrm{cm}^3$ (approximately equal to k^Q_K/Γ). The results of the best fit using $k^Q_{Cs}/\Gamma = 3.0\times10^{-16}\,\mathrm{cm}^3$ are given in Table 6.12, and calculated R_F values obtained with these parameters (solid lines) are plotted against the measured data in Figs. 6.37 to 6.44. Again, it should be noted that the $k^{\Delta J}_{Cs}$ values essentially scale with k^Q_{Cs}. Therefore, if an improved value of k^Q_{Cs} is determined in the future, the values of $k^{\Delta J}_{Cs}/\Gamma$ presented in Table 6.12 should be multiplied by $[k^Q_{Cs}(\mathrm{new})/\Gamma]/3.0\times10^{-16}\,\mathrm{cm}^3$.

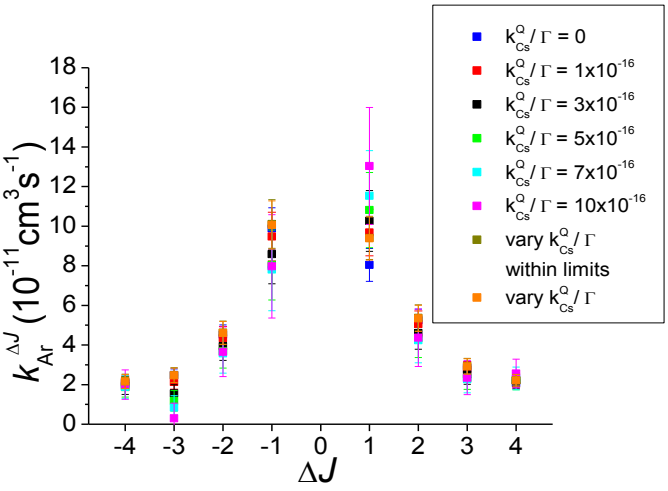

(a) Fitted values of $k^{\Delta J}_{Ar}$ as a function of ΔJ

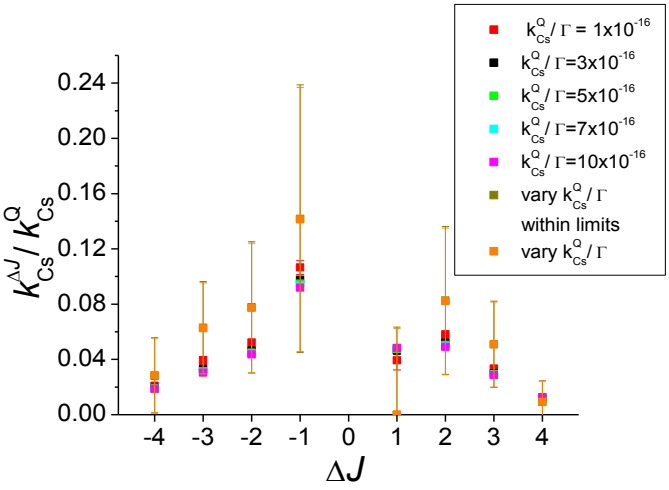

(b) Fitted values of $k^{\Delta J}_{Cs}$ as a function of ΔJ

Figure 6.36: a) Plots of rate coefficients for rotationally inelastic collisions of NaCs $2(A)^1\Sigma^+(14, 32)$ molecules with argon, comparing the results of fits obtained with various fixed values of k^Q_{Cs}/Γ or with k^Q_{Cs}/Γ allowed to vary. b) Same for cesium perturbers except plotted as $k^{\Delta J}_{Cs}/k^Q_{Cs}$ for rotationally inelastic collisions of NaCs $2(A)^1\Sigma^+(14, 32)$, comparing the results of fits obtained with various fixed values of k^Q_{Cs}/Γ or with k^Q_{Cs}/Γ allowed to vary.

Fluorescence Fit, k_{Cs}^{Q}/Γ allowed to vary
Population transfer rate coefficients
NaCs $2(A)^1\Sigma^+(14, 32)$

	Argon	Cesium
ΔJ	$k_{Ar}^{\Delta J}(10^{-11}\,\mathrm{cm^3 s^{-1}})$	$k_{Cs}^{\Delta J}(10^{-11}\,\mathrm{cm^3 s^{-1}})$
-4	2.2 ± 0.4	1.8 ± 1.7
-3	2.5 ± 0.4	3.9 ± 2.1
-2	4.6 ± 0.6	4.9 ± 3.0
-1	10 ± 1	8.9 ± 6.0
+1	9.4 ± 1.1	0 ± 4.0
+2	5.3 ± 0.7	5.2 ± 3.3
+3	2.9 ± 0.4	3.2 ± 1.9
+4	2.2 ± 0.3	0.6 ± 1.0
Quenching	$k_{Ar}^{Q}(10^{-10}\,\mathrm{cm^3 s^{-1}})$	$k_{Cs}^{Q}(10^{-10}\,\mathrm{cm^3 s^{-1}})$
	7.3 ± 1.3	6.3 ± 6.4

Table 6.9: Table of parameters describing rotationally inelastic collisions of NaCs $2(A)^1\Sigma^+(14, 32)$ molecules with argon and cesium perturbers. The parameters were determined from the fluorescence fit of collisional to direct line fluorescence ratios (R_F) for given cesium and argon densities. In this fit, k_{Cs}^{Q}/Γ was allowed to vary. The value $\Gamma = 2.8 \times 10^7 \mathrm{s}^{-1}$ was determined using the computer program LEVEL [40] with the $2(A)^1\Sigma^+$potential of Ref. [13], the $1(X)^1\Sigma^+$potential of Ref. [12], and the transition dipole moment of Ref. [64].

Fluorescence Fit, $k_{Cs}^{Q}/\Gamma = 0\,\mathrm{cm}^3$
Population transfer rate coefficients
NaCs $2(A)^1\Sigma^+(14, 32)$

	Argon	Cesium
ΔJ	$k_{Ar}^{\Delta J}(10^{-11}\,\mathrm{cm}^3\mathrm{s}^{-1})$	$k_{Cs}^{\Delta J}(10^{-11}\,\mathrm{cm}^3\mathrm{s}^{-1})$
-4	2.1 ± 0.3	0.6 ± 1.1
-3	2.5 ± 0.3	1.8 ± 0.6
-2	4.5 ± 0.5	2.0 ± 0.7
-1	9.9 ± 1.0	2.7 ± 1.3
+1	8.0 ± 0.8	0 ± 0.9
+2	5.2 ± 0.6	1.9 ± 0.8
+3	2.8 ± 0.3	1.4 ± 0.5
+4	2.1 ± 0.2	0 ± 0.4
Quenching	$k_{Ar}^{Q}(10^{-10}\,\mathrm{cm}^3\mathrm{s}^{-1})$	$k_{Cs}^{Q}(10^{-9}\,\mathrm{cm}^3\mathrm{s}^{-1})$
	7.0 ± 1.1	0 (fixed)

Table 6.10: Table of parameters describing rotationally inelastic collisions of NaCs $2(A)^1\Sigma^+(14, 32)$ molecules with argon and cesium perturbers. The parameters were determined from the fluorescence fit of collisional to direct line fluorescence ratios (R_F) for given cesium and argon densities. In this fit, k_{Cs}^{Q}/Γ was fixed to zero. The value $\Gamma = 2.8 \times 10^7\mathrm{s}^{-1}$ was determined using the computer program LEVEL [40] with the $2(A)^1\Sigma^+$potential of Ref. [13], the $1(X)^1\Sigma^+$potential of Ref. [12], and the transition dipole moment of Ref. [64].

Fluorescence Fit, $k_{Cs}^{Q}/\Gamma = 1.0 \times 10^{-16}\,\mathrm{cm}^3$
Population transfer rate coefficients
NaCs $2(A)^1\Sigma^+(14, 32)$

	Argon	Cesium
ΔJ	$k_{Ar}^{\Delta J}(10^{-11}\,\mathrm{cm}^3\mathrm{s}^{-1})$	$k_{Cs}^{\Delta J}(10^{-10}\,\mathrm{cm}^3\mathrm{s}^{-1})$
-4	2.1 ± 0.4	0.6 ± 0.1
-3	2.1 ± 0.4	1.1 ± 0.1
-2	4.4 ± 0.6	1.5 ± 0.1
-1	9.5 ± 1.2	3.0 ± 0.1
+1	9.7 ± 1.2	1.1 ± 0.2
+2	5.1 ± 0.7	1.6 ± 0.1
+3	2.8 ± 0.4	0.9 ± 0.1
+4	2.2 ± 0.3	0.4 ± 0.1
Quenching	$k_{Ar}^{Q}(10^{-10}\,\mathrm{cm}^3\mathrm{s}^{-1})$	$k_{Cs}^{Q}(10^{-9}\,\mathrm{cm}^3\mathrm{s}^{-1})$
	6.8 ± 1.3	2.8 (fixed)

Table 6.11: Table of parameters describing rotationally inelastic collisions of NaCs $2(A)^1\Sigma^+(14, 32)$ molecules with argon and cesium perturbers. The parameters were determined from the fluorescence fit of collisional to direct line fluorescence ratios (R_F) for given cesium and argon densities. In this fit, k_{Cs}^{Q}/Γ was fixed to the value $1.0 \times 10^{-16}\,\mathrm{cm}^3$. The value $\Gamma = 2.8 \times 10^7\mathrm{s}^{-1}$ was determined using the computer program LEVEL [40] with the $2(A)^1\Sigma^+$potential of Ref. [13], the $1(X)^1\Sigma^+$potential of Ref. [12], and the transition dipole moment of Ref. [64].

Fluorescence Fit, $k_{Cs}^{Q}/\Gamma = 3.0 \times 10^{-16}\,\mathrm{cm}^3$
Population transfer rate coefficients
NaCs $2(A)^1\Sigma^+(14, 32)$

	Argon	Cesium
ΔJ	$k_{Ar}^{\Delta J}(10^{-11}\,\mathrm{cm}^3\mathrm{s}^{-1})$	$k_{Cs}^{\Delta J}(10^{-10}\,\mathrm{cm}^3\mathrm{s}^{-1})$
-4	1.9 ± 0.4	1.6 ± 0.2
-3	1.6 ± 0.4	2.8 ± 0.1
-2	3.9 ± 0.7	3.9 ± 0.1
-1	8.6 ± 1.5	8.3 ± 0.2
+1	10 ± 2	3.9 ± 0.2
+2	4.6 ± 0.8	4.4 ± 0.1
+3	2.5 ± 0.5	2.5 ± 0.1
+4	2.2 ± 0.4	1.1 ± 0.1
Quenching	$k_{Ar}^{Q}(10^{-10}\,\mathrm{cm}^3\mathrm{s}^{-1})$	$k_{Cs}^{Q}(10^{-9}\,\mathrm{cm}^3\mathrm{s}^{-1})$
	6.2 ± 1.6	8.5 (fixed)

Table 6.12: Table of parameters describing rotationally inelastic collisions of NaCs $2(A)^1\Sigma^+(14, 32)$ molecules with argon and cesium perturbers. The parameters were determined from the fluorescence fit of collisional to direct line fluorescence ratios (R_F) for given cesium and argon densities. In this fit, k_{Cs}^{Q}/Γ was fixed to the value $3.0 \times 10^{-16}\,\mathrm{cm}^3$. The value $\Gamma = 2.8 \times 10^7\mathrm{s}^{-1}$ was determined using the computer program LEVEL [40] with the $2(A)^1\Sigma^+$potential of Ref. [13], the $1(X)^1\Sigma^+$potential of Ref. [12], and the transition dipole moment of Ref. [64].

Fluorescence Fit, $k_{Cs}^{Q}/\Gamma = 5.0 \times 10^{-16}\,\mathrm{cm}^3$
Population transfer rate coefficients
NaCs $2(A)^1\Sigma^+(14, 32)$

	Argon	Cesium
ΔJ	$k_{Ar}^{\Delta J}(10^{-11}\,\mathrm{cm}^3\mathrm{s}^{-1})$	$k_{Cs}^{\Delta J}(10^{-10}\,\mathrm{cm}^3\mathrm{s}^{-1})$
-4	1.9 ± 0.5	2.7 ± 0.2
-3	1.2 ± 0.5	4.4 ± 0.2
-2	3.7 ± 0.8	6.3 ± 0.1
-1	8.0 ± 1.8	13 ± 0.2
+1	11 ± 2	6.7 ± 0.3
+2	4.3 ± 1.0	7.1 ± 0.1
+3	2.3 ± 0.6	4.1 ± 0.1
+4	2.2 ± 0.5	1.8 ± 0.1
Quenching	$k_{Ar}^{Q}(10^{-10}\,\mathrm{cm}^3\mathrm{s}^{-1})$	$k_{Cs}^{Q}(10^{-8}\,\mathrm{cm}^3\mathrm{s}^{-1})$
	5.9 ± 1.9	1.4 (fixed)

Table 6.13: Table of parameters describing rotationally inelastic collisions of NaCs $2(A)^1\Sigma^+(14, 32)$ molecules with argon and cesium perturbers. The parameters were determined from the fluorescence fit of collisional to direct line fluorescence ratios (R_F) for given cesium and argon densities. In this fit, k_{Cs}^{Q}/Γ was fixed to the value $5.0 \times 10^{-16}\,\mathrm{cm}^3$. The value $\Gamma = 2.8 \times 10^7\mathrm{s}^{-1}$ was determined using the computer program LEVEL [40] with the $2(A)^1\Sigma^+$potential of Ref. [13], the $1(X)^1\Sigma^+$potential of Ref. [12], and the transition dipole moment of Ref. [64].

Fluorescence Fit, $k_{Cs}^{Q}/\Gamma = 7.0 \times 10^{-16}\,\mathrm{cm}^3$
Population transfer rate coefficients
NaCs $2(A)^1\Sigma^+(14, 32)$

	Argon	Cesium
ΔJ	$k_{Ar}^{\Delta J}(10^{-11}\,\mathrm{cm}^3\mathrm{s}^{-1})$	$k_{Cs}^{\Delta J}(10^{-10}\,\mathrm{cm}^3\mathrm{s}^{-1})$
-4	1.9 ± 0.6	3.7 ± 0.2
-3	0.8 ± 0.6	6.1 ± 0.2
-2	3.6 ± 1.0	8.7 ± 0.2
-1	7.8 ± 2.1	18 ± 0.2
+1	12 ± 2	9.5 ± 0.4
+2	4.2 ± 1.1	9.8 ± 0.2
+3	2.3 ± 0.7	5.7 ± 0.1
+4	2.3 ± 0.6	2.5 ± 0.2
Quenching	$k_{Ar}^{Q}(10^{-10}\,\mathrm{cm}^3\mathrm{s}^{-1})$	$k_{Cs}^{Q}(10^{-8}\,\mathrm{cm}^3\mathrm{s}^{-1})$
	5.9 ± 2.3	2.0 (fixed)

Table 6.14: Table of parameters describing rotationally inelastic collisions of NaCs $2(A)^1\Sigma^+(14, 32)$ molecules with argon and cesium perturbers. The parameters were determined from the fluorescence fit of collisional to direct line fluorescence ratios (R_F) for given cesium and argon densities. In this fit, k_{Cs}^{Q}/Γ was fixed to the value $7.0 \times 10^{-16}\,\mathrm{cm}^3$. The value $\Gamma = 2.8 \times 10^7\mathrm{s}^{-1}$ was determined using the computer program LEVEL [40] with the $2(A)^1\Sigma^+$potential of Ref. [13], the $1(X)^1\Sigma^+$potential of Ref. [12], and the transition dipole moment of Ref. [64].

Fluorescence Fit, $k_{Cs}^{Q}/\Gamma = 10 \times 10^{-16}\,\mathrm{cm}^3$
Population transfer rate coefficients
NaCs $2(A)^1\Sigma^+(14, 32)$

	Argon	Cesium
ΔJ	$k_{Ar}^{\Delta J}(10^{-11}\,\mathrm{cm}^3\mathrm{s}^{-1})$	$k_{Cs}^{\Delta J}(10^{-10}\,\mathrm{cm}^3\mathrm{s}^{-1})$
-4	2.0 ± 0.7	5.3 ± 0.3
-3	0.3 ± 0.8	8.6 ± 0.3
-2	3.7 ± 1.3	12 ± 0.2
-1	8.0 ± 2.6	26 ± 0.3
+1	13 ± 3	14 ± 0.5
+2	4.4 ± 1.4	14 ± 0.2
+3	2.3 ± 0.9	8.1 ± 0.2
+4	2.6 ± 0.7	3.6 ± 0.2
Quenching	$k_{Ar}^{Q}(10^{-10}\,\mathrm{cm}^3\mathrm{s}^{-1})$	$k_{Cs}^{Q}(10^{-8}\,\mathrm{cm}^3\mathrm{s}^{-1})$
	6.5 ± 2.9	2.8 (fixed)

Table 6.15: Table of parameters describing rotationally inelastic collisions of NaCs $2(A)^1\Sigma^+(14, 32)$ molecules with argon and cesium perturbers. The parameters were determined from the fluorescence fit of collisional to direct line fluorescence ratios (R_F) for given cesium and argon densities. In this fit, k_{Cs}^{Q}/Γ was fixed to the value $10 \times 10^{-16}\,\mathrm{cm}^3$. The value $\Gamma = 2.8 \times 10^7\mathrm{s}^{-1}$ was determined using the computer program LEVEL [40] with the $2(A)^1\Sigma^+$potential of Ref. [13], the $1(X)^1\Sigma^+$potential of Ref. [12], and the transition dipole moment of Ref. [64].

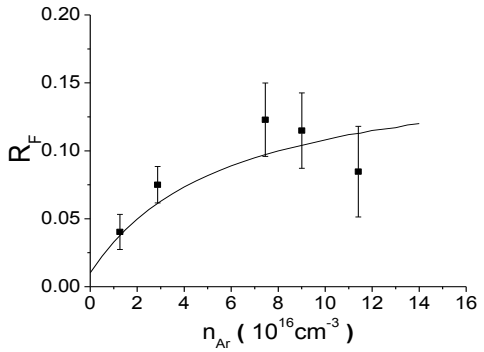

(a) $n_{Cs} = 9.4 \times 10^{14}\,\mathrm{cm}^{-3}$

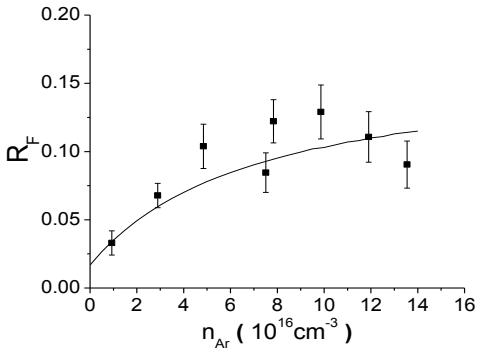

(b) $n_{Cs} = 1.9 \times 10^{15}\,\mathrm{cm}^{-3}$

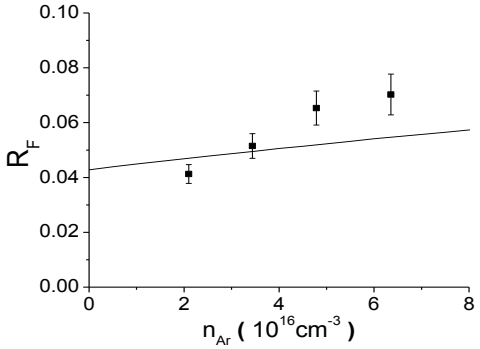

(c) $n_{Cs} = 4.0 \times 10^{16}\,\mathrm{cm}^{-3}$

Figure 6.37: Plots of fluorescence ratio data (R_F) versus argon density for $\Delta J = +1$ collisions of NaCs $2(A)^1\Sigma^+(14, 32)$ molecules with argon perturbers. Each panel represents a different fixed cesium atom density, n_{Cs}. In this, and subsequent plots, the calculated R_F values (solid curves) were obtained using the fit parameters determined with $k_{Cs}^Q/\Gamma = 3.0 \times 10^{-16}\,\mathrm{cm}^3$.

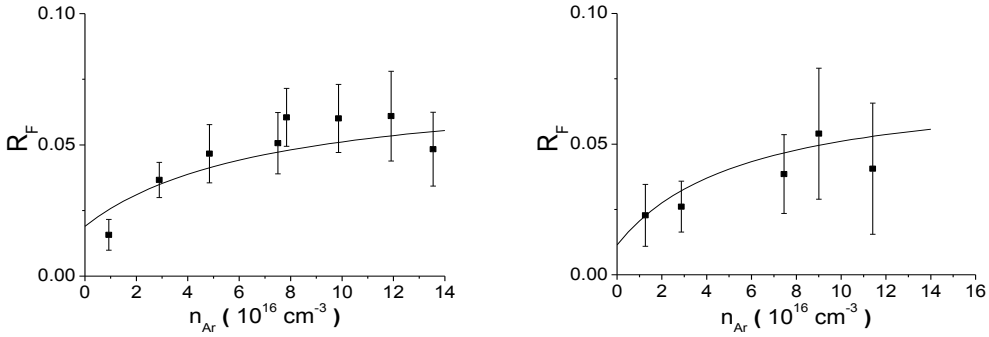

(a) $n_{Cs} = 9.4 \times 10^{14}\,\mathrm{cm}^{-3}$

(b) $n_{Cs} = 1.9 \times 10^{15}\,\mathrm{cm}^{-3}$

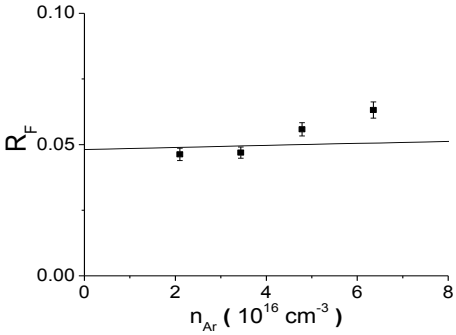

(c) $n_{Cs} = 4.0 \times 10^{16}\,\mathrm{cm}^{-3}$

Figure 6.38: Plots of fluorescence ratio data (R_F) versus argon density for $\Delta J = +2$ collisions of NaCs $2(A)^1\Sigma^+(14, 32)$ molecules with argon perturbers. Each panel represents a different fixed cesium atom density, n_{Cs}.

Unlike NaK-Ar collisions, the NaCs collisional spectra and the fitted parameters show no propensity for $\Delta J =$ even collisions. However, the difference between the cesium rate coefficients for $k_{Cs}^{\Delta J=+1}$ and $k_{Cs}^{\Delta J=-1}$ seems to be a real effect and can be seen directly from the spectra recorded at different cesium densities. As the cesium density is increased and the argon density is decreased, there is a greater difference in the intensities for the $\Delta J = +1$ and $\Delta J = -1$ collisional lines. Figure 6.45 shows an example set of such spectra which demonstrate this effect by showing two collisional progressions obtained with different cesium densities but similar argon

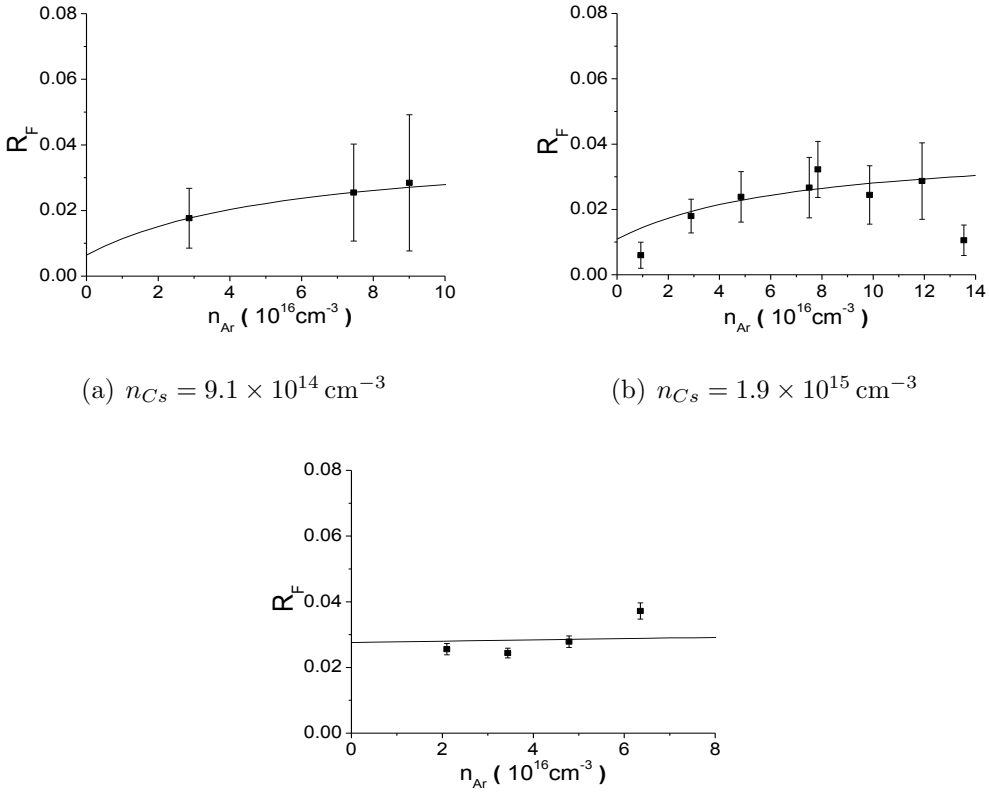

(a) $n_{Cs} = 9.1 \times 10^{14}\,\mathrm{cm}^{-3}$

(b) $n_{Cs} = 1.9 \times 10^{15}\,\mathrm{cm}^{-3}$

(c) $n_{Cs} = 4.0 \times 10^{16}\,\mathrm{cm}^{-3}$

Figure 6.39: Plots of fluorescence ratio data (R_F) versus argon density for $\Delta J = +3$ collisions of NaCs $2(A)^1\Sigma^+(14, 32)$ molecules with argon perturbers. Each panel represents a different fixed cesium atom density, n_{Cs}.

density. The ratio of the $\Delta J = +1$ collisional line intensity to the $\Delta J = -1$ collisional line intensity ($I_{col}^{\Delta J=+1}/I_{col}^{\Delta J=-1}$) is smaller in the case of larger cesium density (using either peak heights or line areas), and this is reflected in the fitted collisional rate coefficients for cesium. When the cesium density is lowered and inelastic collisions are dominated by argon, the ratio of the $\Delta J = +1$ and $\Delta J = -1$ line intensities is much closer to one, and sometimes even larger than one due to a slightly larger argon collision rate coefficient for $\Delta J = +1$ (see Fig. 6.36(a)). Note that this possible propensity for $\Delta J =$ negative in NaCs-Cs collisions is the opposite of what

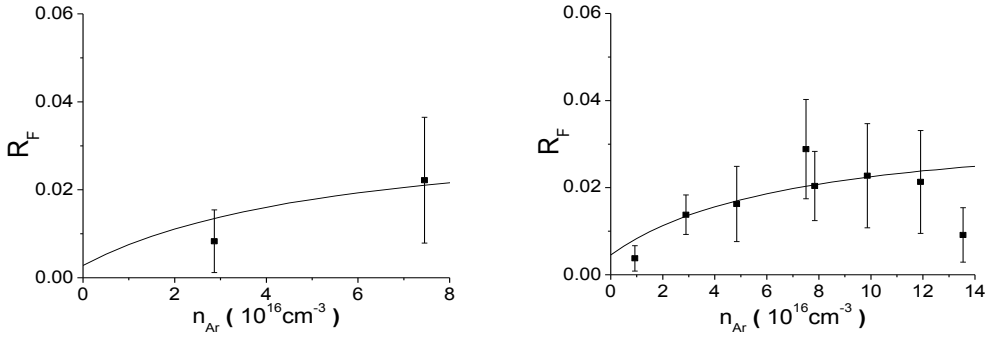

(a) $n_{Cs} = 9.6 \times 10^{14}\,\mathrm{cm}^{-3}$

(b) $n_{Cs} = 1.9 \times 10^{15}\,\mathrm{cm}^{-3}$

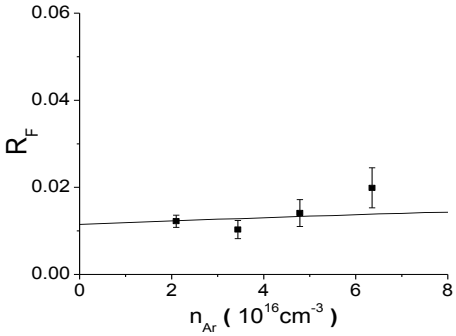

(c) $n_{Cs} = 4.0 \times 10^{16}\,\mathrm{cm}^{-3}$

Figure 6.40: Plots of fluorescence ratio data (R_F) versus argon density for $\Delta J = +4$ collisions of NaCs $2(A)^1\Sigma^+(14, 32)$ molecules with argon perturbers. Each panel represents a different fixed cesium atom density, n_{Cs}.

we observe for NaK-K collisions.

We have taken some preliminary data to study rotationally inelastic collisions of NaCs $2(A)^1\Sigma^+(14, 32)$ molecules with helium perturbers. Due to the larger $\Delta J =$ even propensity observed in NaK-He collisions compared to NaK-Ar collisions, we wondered if such a difference could also be observed in NaCs-He collisions, even though the NaCs is much less symmetric than NaK. It appears, based on the data shown in Fig. 6.46, which were recorded using a low cesium density (hence the

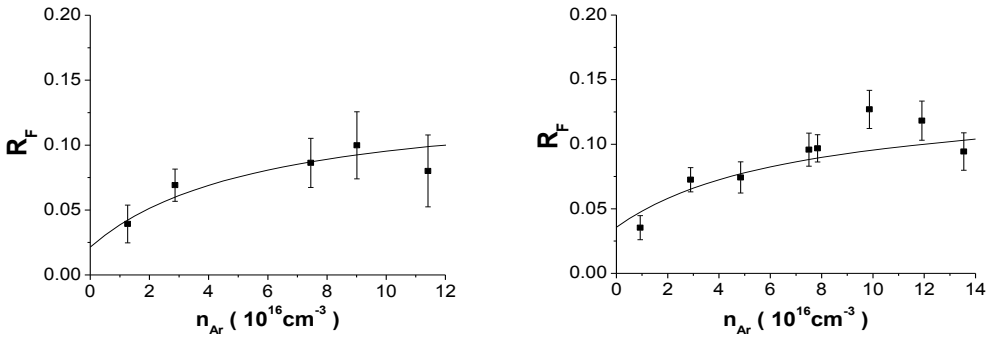

(a) $n_{Cs} = 9.4 \times 10^{14}\,\mathrm{cm}^{-3}$

(b) $n_{Cs} = 1.9 \times 10^{15}\,\mathrm{cm}^{-3}$

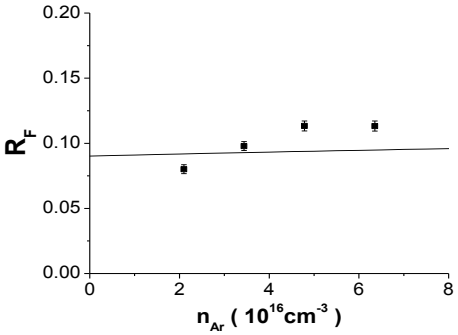

(c) $n_{Cs} = 4.0 \times 10^{16}\,\mathrm{cm}^{-3}$

Figure 6.41: Plots of fluorescence ratio data (R_F) versus argon density for $\Delta J = -1$ collisions of NaCs $2(A)^1\Sigma^+(14, 32)$ molecules with argon perturbers. Each panel represents a different fixed cesium atom density, n_{Cs}.

low signal to noise ratio), that the $\Delta J = \pm 2$ lines are comparable, if not larger than the corresponding $\Delta J = \pm 1$ lines. Thus it appears that the relative number of NaCs $\Delta J =$ even collisions compared to $\Delta J =$ odd collisions is significantly greater for helium than for argon perturbers, even though a $\Delta J =$ even propensity for NaCs-He collisions has not been clearly established.

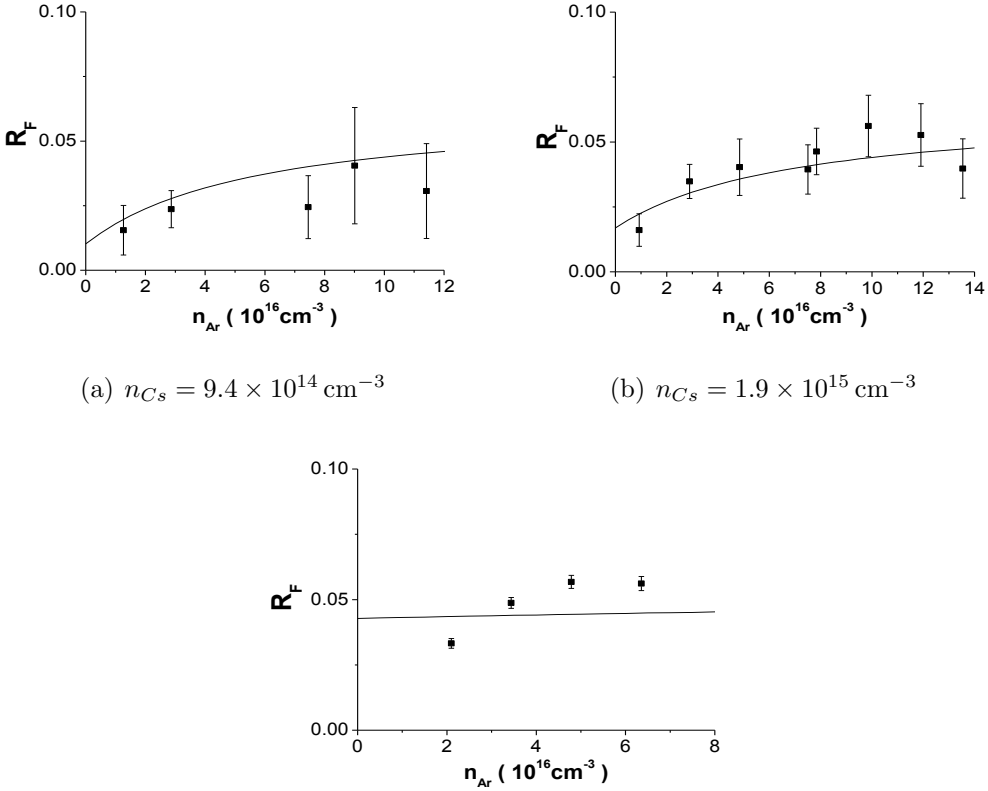

(a) $n_{Cs} = 9.4 \times 10^{14}\,\mathrm{cm}^{-3}$

(b) $n_{Cs} = 1.9 \times 10^{15}\,\mathrm{cm}^{-3}$

(c) $n_{Cs} = 4.0 \times 10^{16}\,\mathrm{cm}^{-3}$

Figure 6.42: Plots of fluorescence ratio data (R_F) versus argon density for $\Delta J = -2$ collisions of NaCs $2(A)^1\Sigma^+(14, 32)$ molecules with argon perturbers. Each panel represents a different fixed cesium atom density, n_{Cs}.

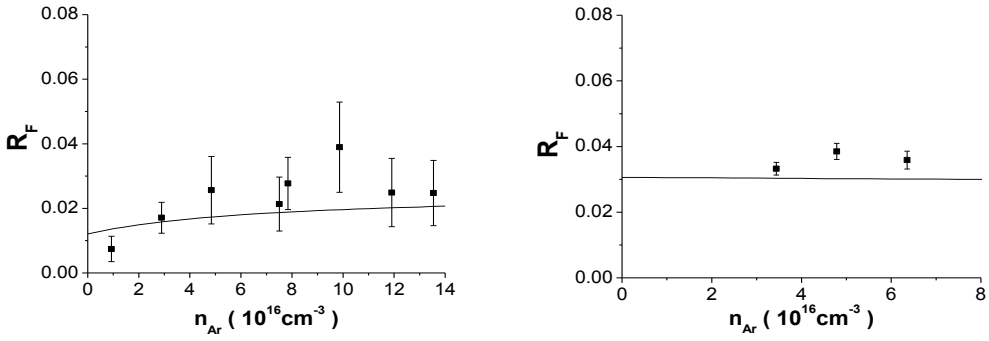

(a) $n_{Cs} = 1.9 \times 10^{15}\,\mathrm{cm}^{-3}$ (b) $n_{Cs} = 4.2 \times 10^{16}\,\mathrm{cm}^{-3}$

Figure 6.43: Plots of fluorescence ratio data (R_F) versus argon density for $\Delta J = -3$ collisions of NaCs $2(A)^1\Sigma^+(14, 32)$ molecules with argon perturbers. Each panel represents a different fixed cesium atom density, n_{Cs}.

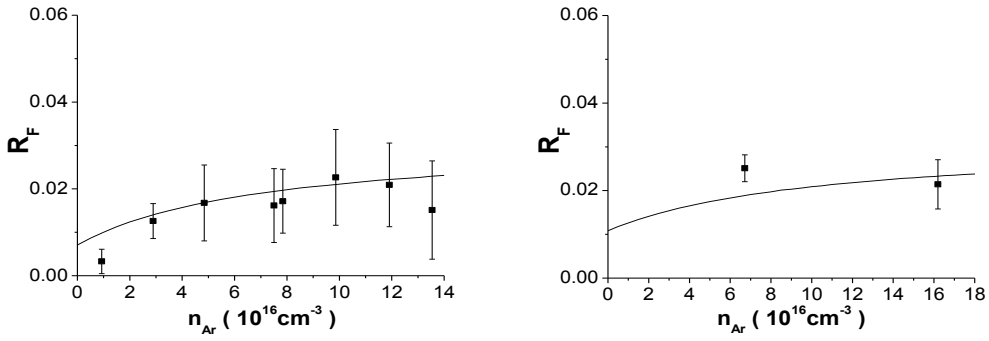

(a) $n_{Cs} = 1.9 \times 10^{15}\,\mathrm{cm}^{-3}$ (b) $n_{Cs} = 4.2 \times 10^{15}\,\mathrm{cm}^{-3}$

Figure 6.44: Plots of fluorescence ratio data (R_F) versus argon density for $\Delta J = -4$ collisions of NaCs $2(A)^1\Sigma^+(14, 32)$ molecules with argon perturbers. Each panel represents a different fixed cesium atom density, n_{Cs}.

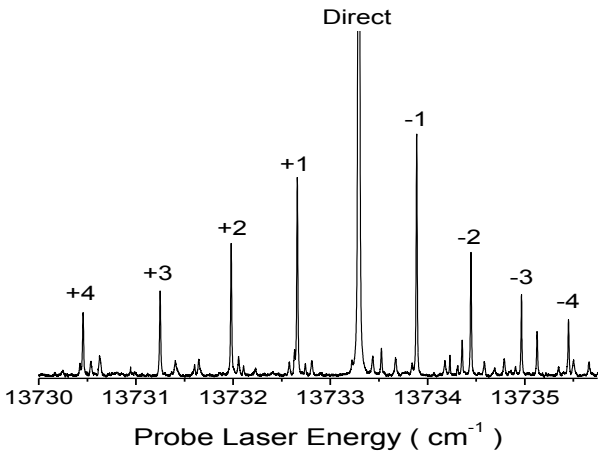

(a) $n_{Cs} = 1.04 \times 10^{16}\,\mathrm{cm}^{-3}$, $I_{col}^{\Delta J=+1}/I_{col}^{\Delta J=-1} = 0.78$

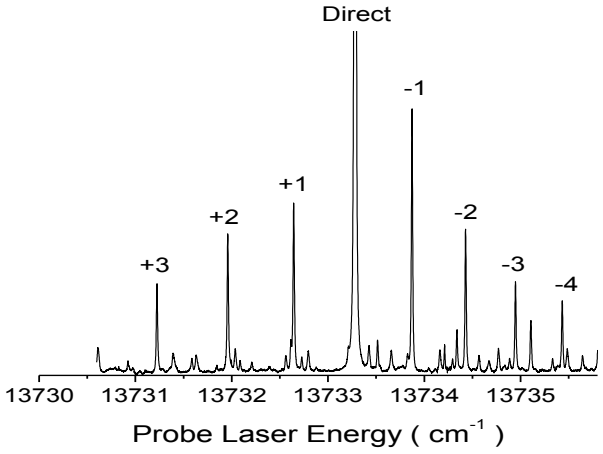

(b) $n_{Cs} = 4.37 \times 10^{16}\,\mathrm{cm}^{-3}$, $I_{col}^{\Delta J=+1}/I_{col}^{\Delta J=-1} = 0.62$

Figure 6.45: Plot of NaCs spectra using two different cesium densities and similar argon densities ($n_{Ar} \sim 6.0 \times 10^{16}\,\mathrm{cm}^{-3}$) comparing the difference in peak intensities for $\Delta J = +1$ and $\Delta J = -1$ collisional lines.

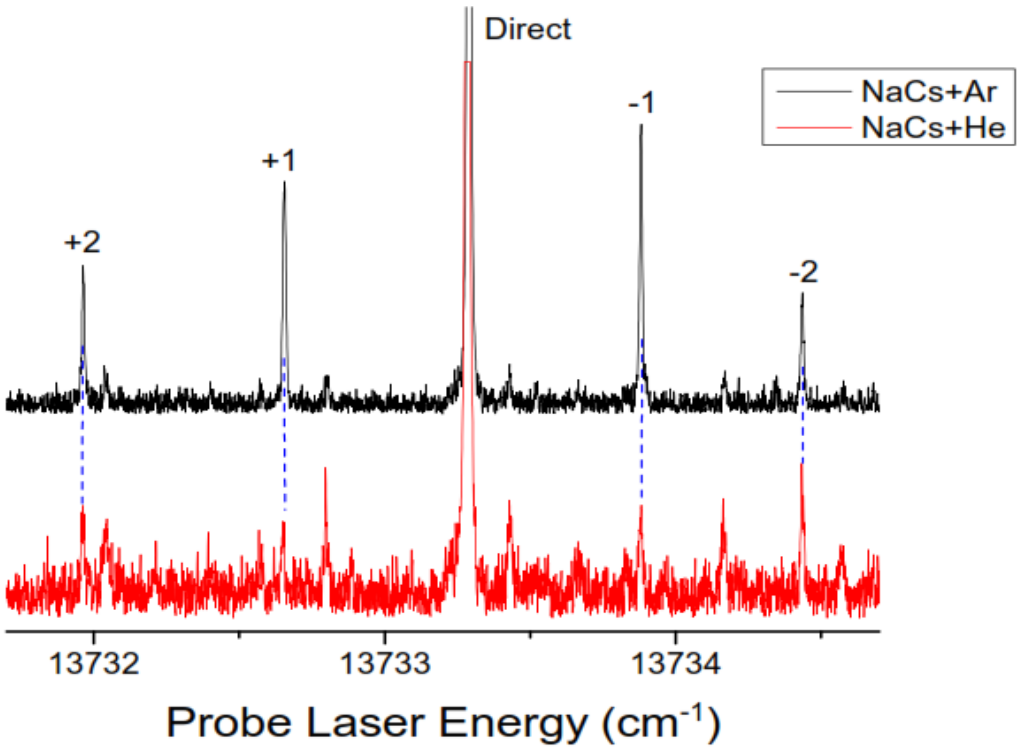

Figure 6.46: Spectra showing rotationally inelastic collisions $\Delta J = \pm 1, \pm 2$ for NaCs $2(A)^1\Sigma^+(14, 32)$ NaCs molecules with argon and helium as the buffer gases. The top trace shows a spectrum obtained using argon as the buffer gas where we see a decrease in the intensity of the collisional peaks with increasing $|\Delta J|$. The bottom trace shows the same collisional transitions for NaCs, except with helium as the buffer gas. The relative number of $\Delta J = \pm 2$ collisions compared to $\Delta J = \pm 1$ collisions appears to be greater for helium than for argon perturbers.

6.7 Vibrationally Inelastic Collisions

Utilizing the polarization spectroscopy method in a V-type pump-probe scheme (see Fig. 1.1), Wolfe [43] observed very weak and noisy spectral lines that he attributed to vibration changing collisions in the NaK ground state. Collisional transfer of population to a nearby vibrational level from the directly pumped level via a vibrationally inelastic collision requires much more energy than a rotationally inelastic collision (but still much less than $k_B T$). We were interested to see whether our OODR fluorescence method could be used to detect v-changing collisions in the excited state ($2(A)^1\Sigma^+$) induced by alkali or noble gas perturbers. Unfortunately, we were unable to observe clean v-changing collision signals in the OODR experiment. Excited-state v-changing collisions are expected to be much more difficult to observe than ground-state v-changing collisions, since in the former case, the collisions compete with radiative decay ($\Gamma \sim 10^7\,\mathrm{s}^{-1}$) whereas in the latter, the collisions compete with the much slower transit relaxation process ($\Gamma \sim 10^5\,\mathrm{s}^{-1}$ at our gas pressures). In addition, the v-changing collision cross-section is significantly smaller (about an order of magnitude) than J-changing collision cross-sections.

We found during our collaboration with Drs. Amanda Ross and Patrick Crozet at Université Lyon that we could observe v changing collisions in the NaK $2(A)^1\Sigma^+$ state using single-step excitation and observing the downward fluorescence with the Fourier transform spectrometer. One advantage of the FTS experiment is that we could record direct line and collisional line data on the same spectrum, even though the direct and collisional lines are far apart in energy. We found the best way to detect these vibrational relaxation lines was to excite a specific J level of a very low lying vibrational level ($v = 0, 1, \mathrm{or}\, 2$) of the $2(A)^1\Sigma^+$state, and then observe collisional lines associated with population transfer to different J levels of a neighboring vibrational state. We were able to observe fluorescence from collisions that changed v and J by using the initial ro-vibrational levels (0, 30), (1, 28), and (2, 33) of the $2(A)^1\Sigma^+$state as shown in Fig. 6.47. The analysis of these spectra will be reported in the PhD dissertation of Kara Richter [65], where the v-changing collision rate coefficients will also be reported.

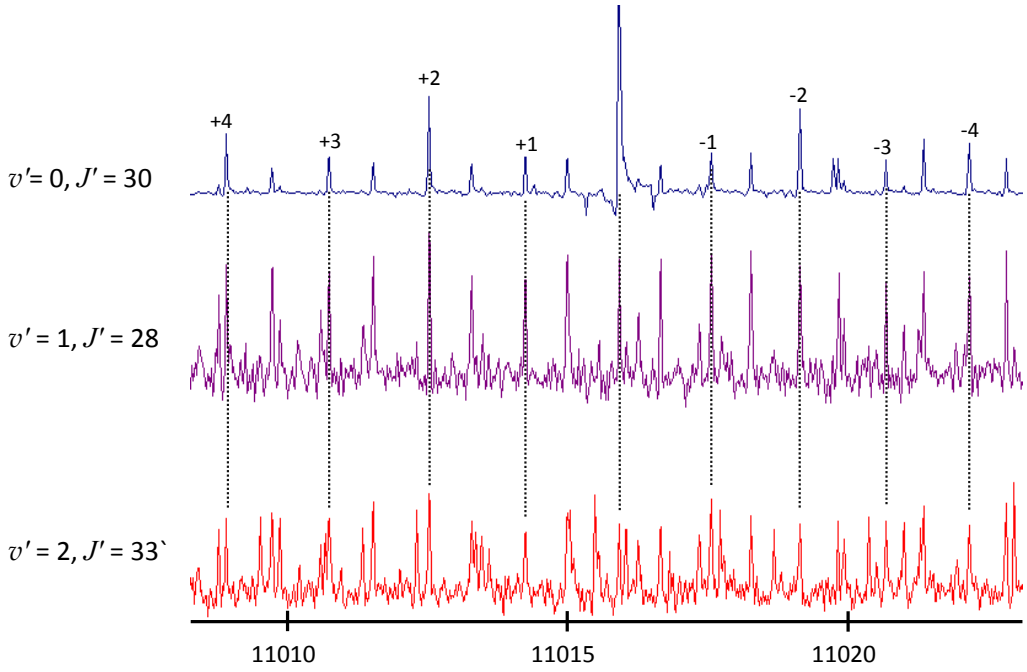

Figure 6.47: Spectra showing fluorescence transitions originating in the NaK $2(A)^1\Sigma^+ v = 0$ level following the excitation of three different initial $2(A)^1\Sigma^+(v', J')$ levels; $(0, 30)$, $(1, 28)$, and $(2, 33)$. The top trace shows a spectrum including the direct line and adjacent rotational collisional satellites. These peaks in the top trace line up with weak peaks in the two lower traces, where different direct lines were excited. From this comaprison, we can identify lines associated with the $v' = 0$ levels when exciting levels of $v' = 1$ or $v' = 2$.

6.8 Line Broadening Analysis

As a by-product of our analysis of spectral line areas, which were used to determine the collisional to direct line intensity ratios for collisional transfer of population, we also obtain direct line and collisional line widths, which increase with buffer gas pressure due to pressure broadening. Recall that the full width at half-maximum of

the Doppler-free, homogeneously broadened spectral line is

$$\Gamma_{tot} = k^{br}_{alk} n_{alk} + k^{br}_{buf} n_{buf} + \Gamma_{nat} + \Gamma_{power} + \dots . \tag{6.11}$$

Thus, if we plot the full width at half-maximum of the direct line versus the buffer gas density, we expect to see a linear relationship. Specifically, a linear fit of these data should yield a slope of k^{br}_{buf} and a y-intercept that is the sum of the remaining homogeneous line broadening mechanisms, $k^{br}_{alk} n_{alk} + \Gamma_{nat} + \Gamma_{power}$. From this analysis of the measured direct line widths, Wolfe *et al.* [30] determined that the NaK $2(A)^1\Sigma^+(16, 30)$ broadening rate coefficient for argon is $k^{br}_{Ar} = (7.2 \pm 0.1) \times 10^{-9}\,\mathrm{cm^3 s^{-1}}$. Performing a similar analysis on our new data for NaK $2(A)^1\Sigma^+(16, 30)$ molecules with helium perturbers (see Fig. 6.48), we obtain a broadening rate coefficient $k^{br}_{He} = (7.0 \pm 0.4) \times 10^{-9}\,\mathrm{cm^3 s^{-1}}$.

We can also get an approximate value for the alkali broadening rate by plotting y-intercept values from the line width versus helium and argon density plots along with "heat pipe" mode data (where the buffer gas is excluded from the central region of the heat pipe oven) versus potassium atom density. A linear fit to these data (see Fig. 6.48(e)) yields the slope that is equal to the potassium broadening rate coefficient, k^{br}_K, and the y-intercept, which corresponds to the remaining terms, $\Gamma_{nat} + \Gamma_{power}$. The resulting potassium broadening rate coefficient is $k^{br}_K = (4.1 \pm 0.3) \times 10^{-8}\,\mathrm{cm^3 s^{-1}}$ which is in agreement with the potassium broadening rate determined by Wolfe *et al.* [30] of $k^{br}_K = (4.5 \pm 0.2) \times 10^{-8}\,\mathrm{cm^3 s^{-1}}$. From the intercept of Fig. 6.48(e), $(4.1 \pm 0.4) \times 10^8\,\mathrm{s^{-1}}$, we obtain the natural linewidth of the direct transition plus additional power broadening that may be present. This does not agree within uncertainties with a value of $(3.2 \pm 0.3) \times 10^8\,\mathrm{s^{-1}}$ from Wolfe *et al.* [30]. However, $\Gamma_{\mathrm{nat}} \sim 4.4 \times 10^7\,\mathrm{s^{-1}}$, so most of this residual linewidth should be attributed to power broadening, and that should clearly depend on laser power. In addition, the uncertainties presented by Wolfe *et al.* and those presented here are statistical errors only.

Using line widths from many data sets taken with argon perturbers (including the data set of Wolfe *et al.* [30]) and with helium perturbers, and using the zero

buffer gas pressure intercepts, our data suggest that our determination of the potassium density is at least self consistent due to how well these data are modeled by a linear fit as shown in Fig. 6.48(e). Such fits do not, however, rule out a consistent systematic error in the potassium density. This systematic uncertainty, which affects k_K^{br} as well as all of the potassium rate coefficients $k_K^{\Delta J}$ and k_K^Q, could be as large as thirty percent from our conservative assignment of uncertainty in the potassium density. However, we also note that such a systematic error would not affect *relative* values of the $k_K^{\Delta J}$'s

Using the same type of analysis as in the NaK case, our studies of rotationally inelastic collisions of NaCs $2(A)^1\Sigma^+(14, 32)$ molecules with argon atoms led us to determine that the argon direct line broadening rate coefficient for NaCs is $k_{Ar}^{br} = (7.8 \pm 0.2) \times 10^{-9}\,\mathrm{cm^3 s^{-1}}$ (see Fig. 6.49(a)-6.49(d)). This broadening rate coefficient is slightly larger than what we have observed for broadening of the NaK $2(A)^1\Sigma^+(16, 30)$ spectral lines by argon. The broadening rate is sensitive to long range interactions, where the polarizability of argon along with the large permanent dipole moment of NaCs, may have an effect. Additionally, with a limited data set, we plot the intercepts of the linear fits to these data to determine the cesium broadening rate coefficient (see Fig. 6.49(d)). From this plot, we have determined that $k_{Cs}^{br} = (1.14 \pm 0.04) \times 10^{-8}\,\mathrm{cm^3 s^{-1}}$. Again, the systematic uncertainty is very much larger, and at least thirty percent.

6.9 Comparison of Experiment and Theory

Early calculations of rotationally inelastic collisions on NaK $2(A)^1\Sigma^+(v = 0,\ J \leq 25)$ molecules with helium perturbers carried out by the Hickman group at Lehigh did not predict a propensity for $\Delta J =$ even collisions, while experimental studies on NaK $2(A)^1\Sigma^+(16, 30)$ with argon did show such a propensity. At that point, it was too early to draw conclusions from those results, since the experiments and theory involved: 1) different perturbers (argon was not studied in the calculations because the larger number of electrons required greater computer resources), 2) different initial vibrational level, and 3) different initial rotational levels. Consequently, the

present experimental work was begun to study the effects of initial v and J on the collisional rate coefficients, to investigate NaK-He collisions, and to begin to study NaCs collisions as a contrast to NaK. Meanwhile, work on the theoretical side was also progressing. Malenda *et al.* [31] used a more robust basis set and were able to demonstrate a strong ΔJ = even propensity in NaK $2(A)^1\Sigma^+(v = 0,\ J \leq 40)$-He collisions. Working with Drs. Ross and Crozet at Université Lyon, we prepared NaK molecules in the $2(A)^1\Sigma^+(0, 14)$ state and observed rotationally inelastic collisions with helium buffer gas atoms. We again observed a propensity for ΔJ = even transitions in this experiment (see Fig. 6.50).

We are currently working to collect and analyze additional data corresponding to our investigation of collisions involving NaK molecules prepared in the $2(A)^1\Sigma^+$ $(16, 14)$ state and the $2(A)^1\Sigma^+(0, 14)$ state. From these data we can make direct comparisons with the calculations of Hickman and coworkers. The current calculations of NaK $2(A)^1\Sigma^+(v = 0, J \leq 45)$ collisions with helium atoms show that for large J most of the orientation is preserved during an inelastic collision ($1 - f \sim 0.9$ at $J = 30$, see Ref. [31]). In the current work we have found that the calculated values of $1 - f$ for NaK $2(A)^1\Sigma^+(v = 0,\ J = 30)$ agree with the experimental results within uncertainties for NaK $2(A)^1\Sigma^+(16, 30)$ collisions with helium. For this initial state, $(16, 30)$, we have measured $1 - f$ to range from approximately 0.7 to 1.0 depending on the value of ΔJ. However, the calculations predict a ΔJ = even propensity for orientation transfer as well as for population transfer and we cannot confirm this result based on the experimental uncertainties. In addition to the orientation transfer, the calculated absolute rate coefficients for collisions of NaK $2(A)^1\Sigma^+(0, 14)$ with helium are of the same order of magnitude as the experimentally determined rate coefficients for collisions of NaK $2(A)^1\Sigma^+(16, 30)$ (see Fig. 6.31 and Ref. [31]).

We are continuing to collect and analyze experimental data for NaK $2(A)^1\Sigma^+(v = 0, 16, J = 14)$ collisions with helium and argon. With these new data, we aim to make direct comparisons of the experimental and theoretical results. Hickman and

coworkers have predicted that there is very little difference in the rotationally inelastic collision cross-sections for different initial vibrational levels of NaK $2(A)^1\Sigma^+$, but that there is a significant dependence on initial rotational level, especially at lower J (see Ref. [31]). Again, we are currently working to determine whether our experiment supports these calculated results for different initial rotational and/or vibrational levels.

Finally, Hickman and coworkers have also begun calculations for population and orientation transfer of the same initial ro-vibrational levels of the $2(A)^1\Sigma^+$state using argon as a collision partner. Specifically, we are interested to see if the calculated results show a more dramatic propensity for ΔJ = even collisions of NaK $2(A)^1\Sigma^+$molecules for helium compared to argon. These new calculations will allow further direct comparisons to current experimental data.

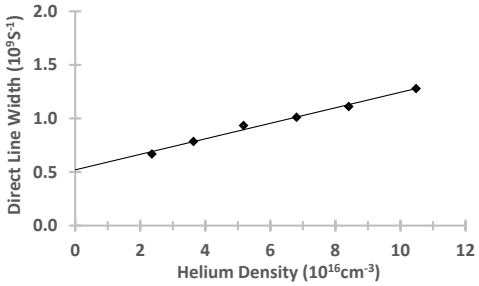

(a) $n_K = 1.80 \times 10^{15}\,\mathrm{cm}^{-3}$

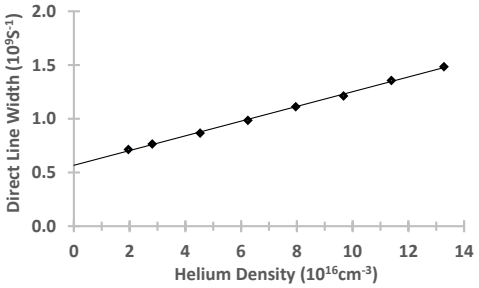

(b) $n_K = 2.75 \times 10^{15}\,\mathrm{cm}^{-3}$

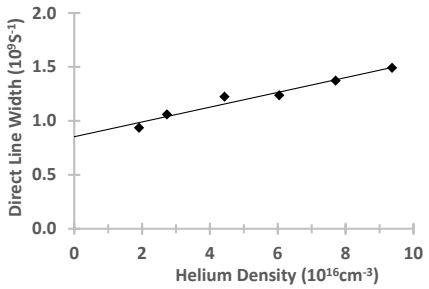

(c) $n_K = 5.44 \times 10^{15}\,\mathrm{cm}^{-3}$

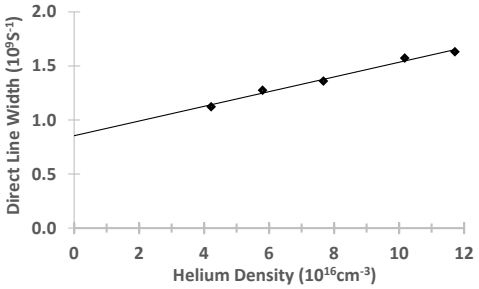

(d) $n_K = 9.20 \times 10^{15}\,\mathrm{cm}^{-3}$

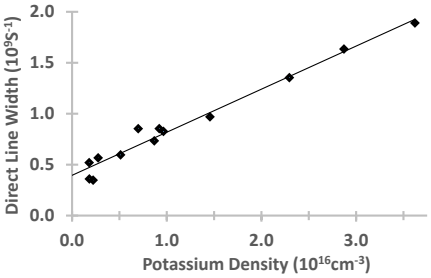

(e) $n_{buf} = 0\,\mathrm{cm}^{-3}$

Figure 6.48: (a)-(d) Plots of direct linewidths as functions of helium density for fixed potassium densities. The potassium density is given for each panel. The slopes of the fitted lines in plots (a) through (d) yield the helium broadening rate coefficient. The intercepts from plots (a) through (d) (and other similar plots) are plotted versus potassium density in (e). The potassium broadening rate coefficient is obtained from the slope of the best linear fit of the data in (e).

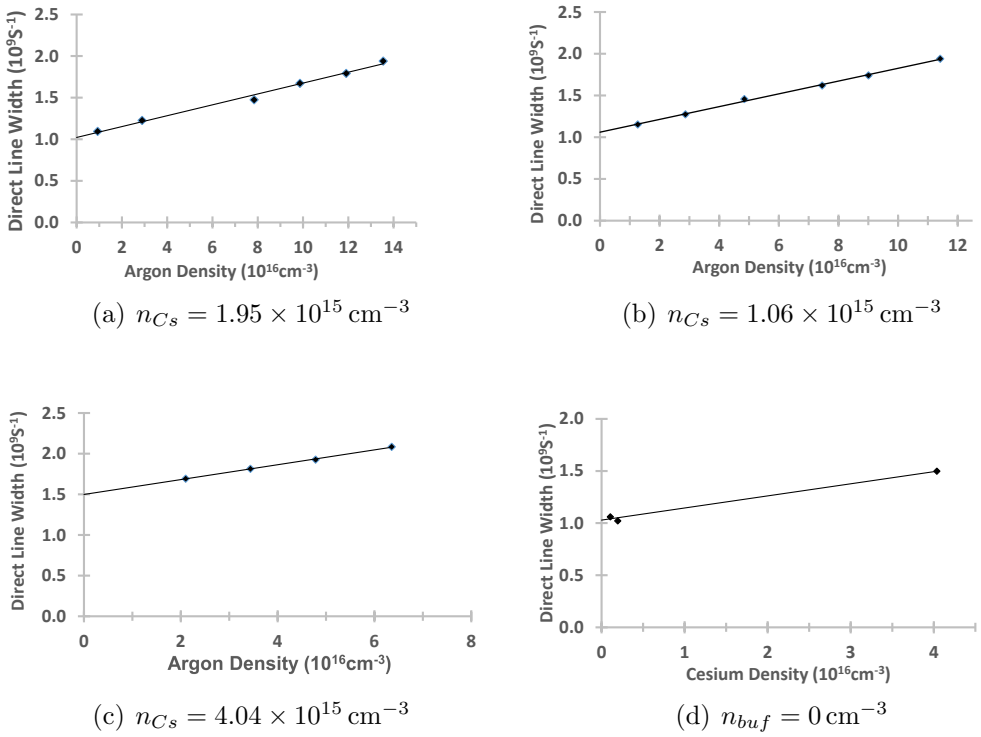

(a) $n_{Cs} = 1.95 \times 10^{15}\,\mathrm{cm}^{-3}$

(b) $n_{Cs} = 1.06 \times 10^{15}\,\mathrm{cm}^{-3}$

(c) $n_{Cs} = 4.04 \times 10^{15}\,\mathrm{cm}^{-3}$

(d) $n_{buf} = 0\,\mathrm{cm}^{-3}$

Figure 6.49: (a)-(c) Plots of NaCs direct linewidths as functions of argon density for fixed cesium densities. The cesium density is given for each panel. The slopes of the fitted lines in plots (a) through (c) yield the argon broadening rate coefficient. The intercepts from plots (a) through (c) are plotted versus cesium density in panel (d). The cesium broadening rate coefficient is obtained from the slope of the best linear fit of the data in plot (d). The number of data sets obtained for NaCs is limited. Better fits can be achieved once more data have been recorded.

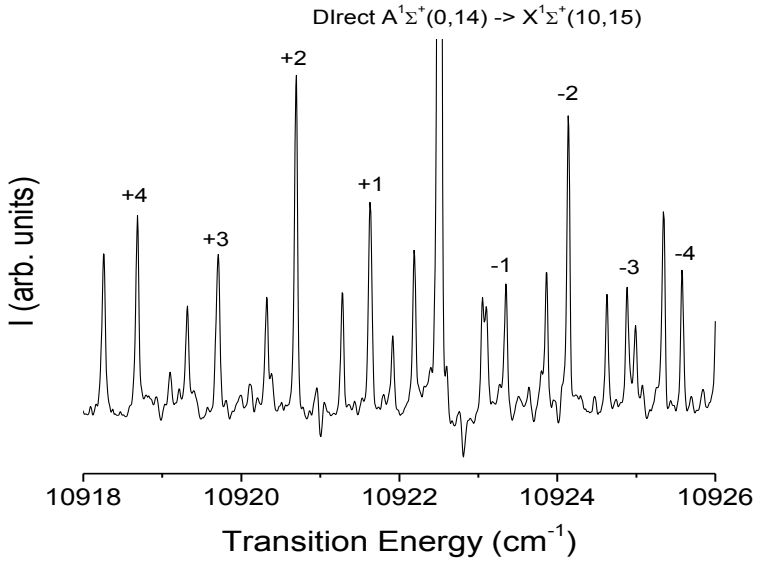

Figure 6.50: Fluorescence spectrum from NaK molecules prepared in the $2(A)^1\Sigma^+(0, 14)$ state showing collisional satellite lines using helium as the buffer gas. From this spectrum, we observe a propensity for ΔJ = even collisions where helium is the dominant collision partner (n_{He} is two orders of magnitude greater than n_K in this case).

Chapter 7

Conclusions and Future Work

7.1 Inelastic Collisions

In this dissertation, I have described our investigations of rotationally inelastic collisions in two separate molecular systems. We have explored rotationally inelastic collisions involving the NaK molecule in greater depth than the earlier study of Wolfe *et al.* [30] in our group by involving another lighter atomic collision partner (He) and by varying the initially prepared ro-vibrational level of the molecule. We have also expanded our collisional studies to involve vibrationally inelastic collisions in the intermediate state. Additionally, we studied a new system, NaCs, which serves as an interesting contrast to NaK.

From the previous work of Wolfe *et al.* [30], we learned that argon is less likely than potassium to destroy orientation during collisions with NaK. From our NaK-Ar and NaK-K collision studies, we believe that the polarizability of the atomic perturber is a more important factor in scrambling orientation than is the mass of the perturber. The masses of potassium and argon are very close, but potassium is much more polarizable than argon. During a collision, the NaK molecule and perturber atom each acquire an induced electric dipole moment and their principal long-range interaction is the dipole-dipole interaction. We believe that potassium is much more effective than argon at scrambling orientation because potassium is

much more polarizable due to its loosely bound single valence electron. Additionally, not only is potassium much more polarizable than the noble gases, but it also has non-zero electronic angular momentum that can be converted to rotational angular momentum in a collision. In fact, we observe that the NaK J-changing collision rate coefficients with potassium perturbers are approximately a factor of ten greater than those of the noble gases.

In the work presented here, we have learned that helium is less effective than argon at transferring population to the ΔJ = odd collisionally populated levels, possibly due to a more symmetric three body interaction of NaK-He compared to NaK-Ar. Helium is also less likely to destroy orientation during a collision than argon. Again, the helium is not very polarizable. Therefore we would expect that these collisions with helium are not as effective as collisions with argon for destroying orientation.

From our earlier investigations of NaK-Ar collisions, we discovered a strong propensity for ΔJ = even transitions. We first naively attributed this to the idea that NaK is "somewhat homonuclear". In the case of a true homonuclear molecule, ΔJ = odd collisions are forbidden by symmetry considerations. Sodium and potassium are closer in size and nuclear charge than sodium and cesium for example, and in fact, we observed no such ΔJ = even propensity for collisions of NaCs with argon. However, the naive argument is untenable because our present studies of NaK-He collisions demonstrate that the propensity for ΔJ=even collisions is much more pronounced than for NaK-Ar collisions. We also find that there is no ΔJ = even propensity for NaK-K collisions. The "homonuclearity" of NaK cannot depend on the collision partner, so these studies reveal that something else is going on. The current data suggest that there is a weak ΔJ = even propensity for NaCs-He collisions.

Prof. A.P. Hickman's group at Lehigh has carried out theoretical calculations of the J-changing and orientation changing collision cross-sections for NaK-He (one of our main motivations for the current experimental study of NaK-He collisions

was to provide a direct test of these calculations). In their calculations, they found that the propensity is very strongly dependent on the long range behavior of the atom-molecule potential. Current theoretical work in Prof. Hickman's group involves extending the calculations to NaK-Ar.

From our inelastic collisions analysis, we obtain peak heights and widths of the direct $3^1\Pi(7,29) \leftarrow 2(A)^1\Sigma^+(16,30)$ line, from which we determined helium line broadening rate coefficients. Combining our data with that of Wolfe *et al.* [30], we were able to also obtain an improved potassium line broadening rate coefficient for the $3^1\Pi(7,29) \leftarrow 2(A)^1\Sigma^+(16, 30)$ direct line. The line broadening rate coefficient for NaK-K turns out to be about six times larger than the rate coefficient for NaK-He. Additionally, from this same method, we obtained cesium and argon line broadening rate coefficients for the NaCs $5^3\Pi_{0^+}(10,31) \leftarrow b^3\Pi_{0^+} \sim 2(A)^1\Sigma^+(14,32)$ direct line. The NaCs-Ar broadening rate coefficient is similar in magnitude to the NaK-Ar broadening rate coefficient. Based on limited data for cesium collisions, we obtained a cesium line broadening rate coefficient that is about four times smaller than that for the NaK-K line broadening rate.

7.2 Future Work

As direct continuation of this work, we aim to collect additional rotationally inelastic collisional data corresponding to the $2(A)^1\Sigma^+(16,14)$ and $2(A)^1\Sigma^+(0,14)$ initial states of NaK with argon and helium. The calculations of cross-sections for these collision processes are extensive, requiring super-computer resources. Performing these calculations with a smaller initial J is computationally more manageable. Dr. Hickman and coworkers have performed calculations for rotationally inelastic collisions of $2(A)^1\Sigma^+(15,14)$ NaK molecules with helium and have begun calculations for rotationally inelastic collisions of $2(A)^1\Sigma^+(16,14)$ NaK molecules with argon. These will be directly comparable to data we are currently collecting.

Since we have studied inelastic collisions of NaK molecules with argon and helium, a follow up to the current work is to study collisions involving heavier, more

polarizable inert gas perturbers. The objective is to learn more about how population and orientation transfer in a rotationally inelastic collision is affected by the mass and polarizability of the inert gas atom. We anticipate that a collision partner with larger polarizability would result in larger f values for destruction of orientation during an inelastic collision, and also have larger rate coefficients for population transfer collisions. It would be interesting to observe if the propensity for ΔJ = even collisions becomes less pronounced with larger, more polarizable inert gas atoms, since this propensity is smaller for NaK-Ar collisions compared to NaK-He collisions.

In addition, Malenda *et al.* [31] have carried out theoretical quantum chemistry calculations of alignment transfer probabilities in NaK-He collisions. Thus, as a project for a future student, an experimental alignment study offers the possibility to test these state-of-the-art calculations. Alignment is defined as [44],

$$\text{Alignment} = \left\langle \frac{3M_J'^2 - J'(J'+1)}{\sqrt{J'(J'+1)\left[J'(J'+1) - \frac{3}{4}\right]}} \right\rangle, \tag{7.1}$$

and is essentially a measure of the second moment of the distribution of population over the M_J levels (i.e., are the high $|M_J|$ or low $|M_J|$ levels more likely to be populated than the statistical average). In the alignment experiment, instead of using a circularly polarized pump beam, which creates an orientation, a linearly polarized pump beam is used polarized at 45 degrees with respect to the vertical polarization of the probe beam. This creates a preferential (but symmetric) distribution in the $|M_J|$ levels, i.e., an alignment. Kara Richter [65] has derived an expression relating the polarization spectroscopy probe signals to the intermediate state alignment as observed in this 45° vertically polarized pump experiment. We have set up such an experiment using this idea to show that we can, indeed, observe direct and collisional lines (see Fig. 7.1).

In collaboration with Drs. Ross and Crozet of Université Lyon 1, we plan to continue to investigate v-changing collisions of NaK with inert gas perturbers. Now that we have observed vibrationally inelastic collisions in the intermediate $2(A)^1\Sigma^+$

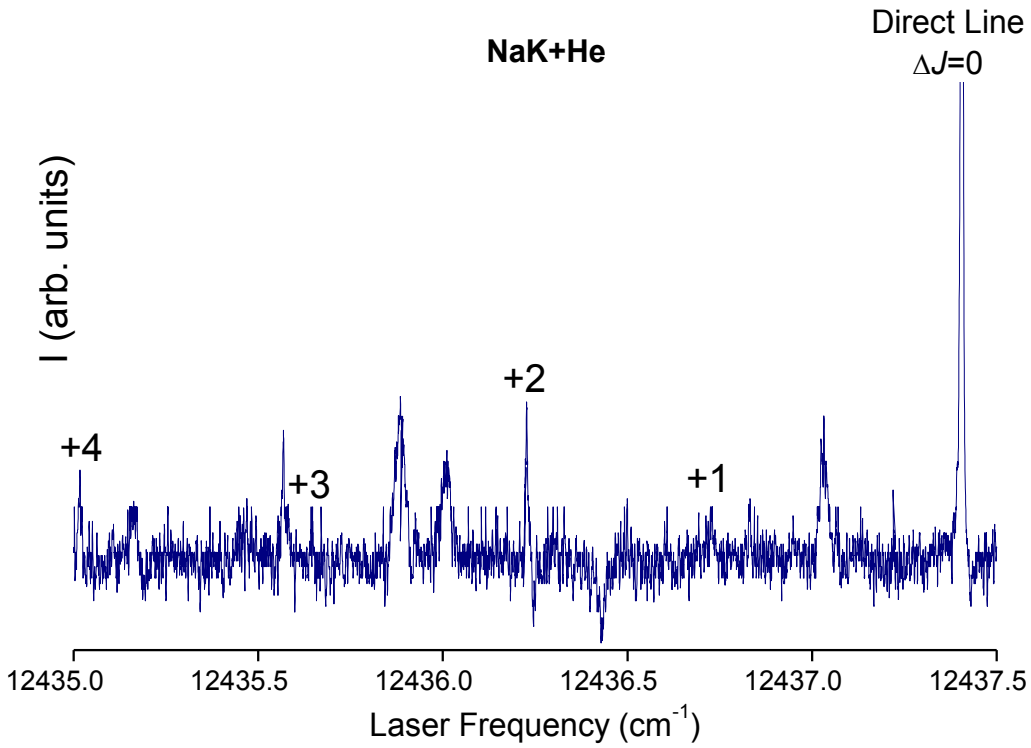

Figure 7.1: An example of collisional relaxation as observed using the alignment polarization technique. This transition is the same as one we used for our orientation studies, $3^1\Pi(7,29) \leftarrow 2(A)^1\Sigma^+(16,\ 30) \leftarrow 1(X)^1\Sigma^+(0,29)$. We have found the signals in this alignment experiment to have more background noise compared to those in the orientation experiment.

state of NaK with helium and argon, a future student could perform a study to determine collision rate coefficients for these types of collisions and for various atomic perturbers. From our preliminary investigation, we have found that the rate coefficient for vibrationally inelastic collisions is about an order of magnitude smaller than that for rotationally inelastic collisions. Thus such v-changing collisions may be neglected in the theoretical calculations of the effects of rotationally inelastic collisions. We plan to determine rate coefficients for v-changing collisions, and the analysis of data already collected is being carried out by Richter [65]. An important

difference between the v-changing and J-changing collision studies is that, in the former case, care must be taken to include the effects of different radiative rates (Γ) for different v levels and the fact that the detector response may vary across different emission wavelength ranges.

In the current work we determined population transfer rate coefficients for NaCs collisions with argon. An interesting follow up on this would be to determine rate coefficients for NaCs-He rotationally inelastic collisions to determine the extent of a propensity for $\Delta J =$ even collisions (to date, we have only one or two scans with NaCs-He which seem to show a slight propensity for $\Delta J =$ even) and to measure the transfer of orientation in NaCs-noble-gas collisions with a polarization spectroscopy experiment. To carry out the NaCs polarization spectroscopy experiment in our lab requires reversing the roles of the dye and Ti:Sapphire lasers (i.e., the Ti:Sapphire beam would be circularly polarized so that it could act as the pump laser, while the dye beam would be linearly polarized so it could serve as the probe) in order the match the energy ranges of the lasers to the corresponding transition energies of the molecules. Alternatively, we have demonstrated that polarization signals can still be observed with the linearly polarized Ti:Sapphire serving as the "probe" even though it is tuned to resonance with the $2(A)^1\Sigma^+(v', J') \leftarrow 1(X)^1\Sigma^+(v'', J'')$ transition, while the circularly polarized dye laser serves as the "pump" laser tuned to the $3^1\Pi(v, J) \leftarrow 2(A)^1\Sigma^+(v', J')$ transition. However, with this latter setup we noticed that the polarization signals are much smaller than we observed in NaK. In this case, the signals associated with the direct lines, are ~ 10 nA in size, compared to ~ 150 nA in the NaK experiment. So far, we have been unable to observe collisional lines, since the stronger collisional line intensities are typically only expected to be $5 - 10\%$ of the direct line signal, and may be smaller depending on the conditions. Presumably, the weak linearly polarized probe beam simply does not excite a sufficient number of NaK molecules to the intermediate state.

Finally, an additional project for a future student, in light of work done by Faust [38] on spin-orbit and non-adiabatic coupling between ro-vibrational levels of the $5^3\Pi_{0^+}$ and $7^1\Sigma^+$ states of NaCs, is rotational energy transfer between nearby coupled

electronic states. In NaCs the spin-orbit coupling of the $2(A)^1\Sigma^+$ and $1(b)^3\Pi_{0^+}$ states is much larger than in NaK, such that almost every ro-vibrational level is a mixture of singlet and triplet, and consequently almost every level is a "window level". The prepared ro-vibrational level of the molecule may have a much different triplet amplitude than that of a nearby collisionally populated ro-vibrational level. In the rate coefficients presented here for NaCs, we have neglected the issue of spin-orbit effects and singlet-triplet (as opposed to singlet-singlet or triplet-triplet) level transfer. In NaK, there are some known "window levels" in the intermediate state which have significant amplitudes of both singlet and triplet character, and these are often exploted for PFOODR spectroscopy. However, the ro-vibrational levels used in the present collision studies on NaK are all of pure singlet character. As an intermediate case, it would be advantageous to start with collisions of atomic perturbers with NaK molecules prepared in a "window level" or of collisions which transfer population to a "window level", since the effects of coupled singlet-triplet ro-vibrational levels are present, but are better better understood and not as extreme as in the case of the NaCs molecule. The singlet and triplet character of levels is almost certainly a factor in the transfer of population thereby affecting the collisional rate coefficients. This effect would need to be taken into account in the R_F equation for coupled ro-vibrational levels in NaCs or NaK.

Bibliography

[1] J. Woerdman, "Doppler-free two-photon transitions of the sodium molecule", Chem. Phys. Lett. **43**, 279–282 (1976).

[2] L. Li and R. W. Field, "Direct observation of high-lying $^3\Pi_g$ states of the sodium molecule by optical-optical double resonance", J. Phys. Chem. **87**, 3020–3022 (1983).

[3] E. Laub, I. Mazsa, S. Webb, J. L. Civita, I. Prodan, Z. Jabbour, R. Namiotka, and J. Huennekens, "Experimental Study of the NaK $3^1\Pi$ State", J. Mol. Spectrosc. **193**, 376–388 (1999), erratum: **221**, 142–144 (2003).

[4] L. Morgus, P. Burns, R. D. Miles, A. D. Wilkins, U. Ogba, A. P. Hickman, and J. Huennekens, "Experimental study of the NaK $3^3\Pi$ double minimum state", J. Chem. Phys. **122**, 144313 (2005).

[5] A. D. Wilkins, L. Morgus, J. Hernandez-Guzman, J. Huennekens, and A. P. Hickman, "The NaK $1^{1,3}\Delta$ states: Theoretical and experimental studies of fine and hyperfine structure of rovibrational levels near the dissociation limit", J. Chem. Phys. **123**, 124306 (2005).

[6] J. Huennekens, I. Prodan, A. Marks, L. Sibbach, E. Galle, T. Morgus, and Li Li, "Experimental studies of the NaK $1^3\Delta$ state", J. Chem. Phys. **113**, 7384–7397 (2000).

[7] R. D. Miles, L. Morgus, D. O. Kashinski, J. Huennekens, and A. P. Hickman, "Nonadiabatic coupling in the $3^3\Pi$ and $4^3\Pi$ states of NaK", J. Chem. Phys. **125**, 154304 (2006).

[8] P. Burns, L. Sibbach-Morgus, A. D. Wilkins, F. Halpern, L. Clarke, R. D. Miles, Li Li, A. P. Hickman, and J. Huennekens, "The $4^3\Sigma^+$ state of NaK: Potential energy curve and hyperfine structure", J. Chem. Phys. **119**, 4743–4754 (2003).

[9] S. Ashman, B. McGeehan, C. M. Wolfe, C. Faust, K. Richter, J. Jones, A. P. Hickman, and J. Huennekens, "Experimental studies of the NaCs $5^3\Pi_0$ and $1(a)^3\Sigma^+$ states", J. Chem. Phys. **136**, 114313 (2012).

[10] I. Russier-Antoine, A. Ross, M. Aubert-Frécon, F. Martin, and P. Crozet, "An improved potential energy curve for the ground state of NaK", J. Phys. B **33**, 2753 (2000).

[11] A. Ross, R. Clements, and R. Barrow, "The $A(2)^1\Sigma^+$ state of NaK", J. Mol. Spectrosc. **127**, 546 – 548 (1988).

[12] O. Docenko, M. Tamanis, R. Ferber, A. Pashov, H. Knöckel, and E. Tiemann, "Spectroscopic studies of NaCs for the ground state asymptote of Na+ Cs pairs", The European Physical Journal D-Atomic, Molecular, Optical and Plasma Physics **31**, 205–211 (2004).

[13] J. Zaharova, M. Tamanis, R. Ferber, A. N. Drozdova, E. A. Pazyuk, and A. V. Stolyarov, "Solution of the fully-mixed-state problem: Direct deperturbation analysis of the $A^1\Sigma^+ - b^3\Pi$ complex in a NaCs dimer", Phys. Rev. A **79**, 012508 (2009).

[14] S. Kasahara, M. Baba, and H. Katô, "High resolution laser spectroscopy up to the dissociation limit of the NaK $B^1\Pi$ state, and predissociation near the dissociation limit", J. Chem. Phys. **94**, 7713–7720 (1991).

[15] A. Pashov, I. Jackowska, W. Jastrzbski, and P. Kowalczyk, "Polarization labeling spectroscopy of the $3^1\Pi$ and $6^1\Sigma^+$ states in NaK", Phys. Rev. A **58**, 1048 (1998).

[16] P. Kowalczyk, W. Jastrzebski, A. Pashov, S. Magnier, and M. Aubert-Frécon, "Potential energies of the $4^1\Pi$ and $5^1\Pi$ states of NaK by polarization labelling

spectroscopy and by *ab initio* calculations", Chem. Phys. Lett. **314**, 47–51 (1999).

[17] A. Grochola, W. Jastrzebski, P. Kortyka, and P. Kowalczyk, "Experimental study of the $6^1\Pi$ and $7^1\Pi$ states of NaK by polarization labeling spectroscopy technique", J. Mol. Spectrosc. **221**, 279–284 (2003).

[18] R. Nadyak, W. Jastrzebski, and P. Kowalczyk, "On the $5^1\Sigma^+$ state of NaK", Chem. Phys. Lett. **353**, 414–417 (2002).

[19] C. Ottinger, R. Velasco, and R. Zare, "Some Propensity Rules in Collision-Induced Rotational Quantum Jumps", J. Chem. Phys. **52**, 1636–1643 (1970).

[20] T. P. Scott, N. Smith, and D. E. Pritchard, "Application of fitting laws to rotationally inelastic rate constants: $Li^*_2(A^1\Sigma)$+Ne, Ar, Xe.", J. Chem. Phys. **80**, 4841–4850 (1984).

[21] P. D. Magill, B. Stewart, N. Smith, and D. Pritchard, "Dynamics of quasiresonant vibration−rotation transfer in atom-diatom scattering", Phys. Rev. Lett. **60**, 1943 (1988).

[22] B. Stewart, P. D. Magill, and D. E. Pritchard, "Quasi-Resonant Vibrational-Rotational Transfer in Inelastic Li^*_2-Ne Collisions", J. Phys. Chem. A **104**, 10565–10575 (2000).

[23] K. Bergmann and W. Demtroder, "Inelastic cross sections of excited molecules. III. Absolute cross sections for rotational and vibrational transitions in the Na_2 ($B^1\Pi_u$) state", Journal of Physics B: Atomic and Molecular Physics **5**, 2098 (1972).

[24] Y. Gao and B. Stewart, "Comparison of experimental and computed vibrationally inelastic rate constants for Li_2 $A^1\Sigma^+_u$−Ne collisions", J. Chem. Phys. **103**, 860–863 (1995).

[25] Y. Gao, P. S. Gorgone, S. Davis, E. K. McCall, and B. Stewart, "Dependence of level-resolved energy transfer on initial vibrational level in Li_2 $(A)^1\Sigma^+_u$-Ne collisions", J. Chem. Phys. **104**, 1415–1426 (1996).

[26] R. Teets, R. Feinberg, T. W. Hänsch, and A. L. Schawlow, "Simplification of Spectra by Polarization Labeling", Phys. Rev. Lett. **37**, 683–686 (1976).

[27] H. Salami, T. Bergeman, B. Beser, J. Bai, E. H. Ahmed, S. Kotochigova, A. M. Lyyra, J. Huennekens, C. Lisdat, A. V. Stolyarov, O. Dulieu, P. Crozet, and A. J. Ross, "Spectroscopic observations, spin-orbit functions, and coupled-channel deperturbation analysis of data on the $A^1\Sigma_u^+$ and $b^3\Pi_u$ states of Rb_2", Phys. Rev. A **80**, 022515 (2009).

[28] A. J. McCaffery, "Quasiresonant vibration-rotation transfer: A kinematic interpretation", J. Chem. Phys. **111**, 7697–7700 (1999).

[29] M. H. Alexander and H. Werner, "Rotationally inelastic collisions of $Li_2(A^1\Sigma_u^+)$ with Ne: Fully ab initio cross sections and comparison with experiment", J. Chem. Phys. **95**, 6524–6535 (1991).

[30] C. M. Wolfe, S. Ashman, J. Bai, B. Beser, E. H. Ahmed, A. M. Lyyra, and J. Huennekens, "Collisional transfer of population and orientation in NaK", J. Chem. Phys. **134**, 174301 (2011).

[31] R. F. Malenda, T. J. Price, J. Stevens, L. Uppalapati, P. Weiser, A. Kuczala, D. Talbi, and A. P. Hickman, "Theoretical Calculations of Rotationally Inelastic Collisions of He with NaK($A^1\Sigma^+$): Transfer of Population, Orientation, and Alignment", Submitted to J. Chem. Phys. (2015).

[32] B. H. Bransden and C. J. Joachain, *Physics of Atoms and Molecules* (Addison Wesley Longman Limited, Essex, 1983).

[33] S. Magnier, M. Aubert-Frecon, and P. Millie, "Potential energies, permanent and transition dipole moments for numerous electronic excited states of NaK", J. Mol. Spectrosc. **200**, 96 (2000).

[34] M. Korek, S. Bleik, and A. R. Allouche, "Theoretical calculation of the low laying electronic states of the molecule NaCs with spin-orbit effect", J. Chem. Phys. **126**, 124313 (2007).

[35] G. Herzberg, *Spectra of Diatomic Molecules* (Van Nostrand Reinhold, New York, 1950).

[36] J. L. Dunham, "The Energy Levels of a Rotating Vibrator", Phys. Rev. **41**, 721–731 (1932).

[37] P. F. Bernath, *Spectra of Atoms and Molecules* (Oxford University Press, New York, 1995).

[38] C. Faust, Ph.D. thesis, Lehigh University, 2014.

[39] I. Kovács, *Rotational Structure in the Spectra of Diatomic Molecules* (American Elsevier Pub. Co., New York, 1969).

[40] R. J. Le Roy, "LEVEL 8.0: A Computer Program for Solving the Radial Schrodinger Equation for Bound and Quasibound Levels", University of Waterloo Physics Research Report CP-663 (2007), see http://leroy.uwaterloo.ca/programs/.

[41] W. Demtröder, *Laser Spectroscopy: Basic Concepts and Instrumentation*, 3rd ed. (Springer-Verlag, Berlin, 2003).

[42] F. C. Spano, "Theory of sub-Doppler AutlerTownes splitting in molecules: Alignment and orientation of the angular momentum in nonpolar molecules", J. Chem. Phys. **114**, 276–288 (2001).

[43] C. Wolfe, Ph.D. thesis, Lehigh University, 2010.

[44] R. Zare, *Angular Momentum: Understanding Spatial Aspects in Chemistry and Physics* (Wiley, New York, 1988).

[45] R. F. Malenda, Ph.D. thesis, Lehigh University, 2012.

[46] C. R. Vidal and J. Cooper, "Heat Pipe Oven: A New, Well-Defined Metal Vapor Device for Spectroscopic Measurements", J. Appl. Phys. **40**, 3370–3374 (1969).

[47] L. Morgus, Ph.D. thesis, Lehigh University, 2005.

[48] *Customer Training Manual: Model 699 Dye Laser*, Coherent, Inc., Palo Alto, CA, 1988.

[49] *Coherent 899-21 Titanium:Sapphire Ring Laser: Operators Manual*, Coherent, Inc., Palo Alto, CA, 1990.

[50] *Optical Configuration for the Bomem DA3 Series - Fourier Transform Spectrophotometer, Training Manual*, Bomem, Inc., Vanier, Québec, CA, 1986.

[51] A. N. Nesmeyanov, *Vapor Pressure of the Chemical Elements* (Elsevier Publishing, New York, 1963).

[52] R. Chang, *General Chemistry* (McGraw-Hill Higher Education, New York, 2000).

[53] A. Corney, *Atomic and laser spectroscopy* (Clarendon Press Oxford, New York, 1978).

[54] E. Lewis, "Collisional relaxation of atomic excited states, line broadening and interatomic interactions", Physics Reports **58**, 1 – 71 (1980).

[55] G. P. M. Poppe and C. M. J. Wijers, "More Efficient Computation of the Complex Error Function", ACM Trans. Math. Softw. **16**, 38–46 (1990).

[56] M. Abramowitz and I. A. Stegun, *Handbook of mathematical functions: with formulas, graphs, and mathematical tables* (U.S. Govt. Print. Off., Washington, DC, USA, 1964).

[57] N. Lwin, D. McCartan, and E. Lewis, "The Determination of Collision Damping Constants", The Astrophysical Journal **213**, 599–606 (1977).

[58] J. Huennekens and A. Gallagher, "Self-broadening of the Sodium Resonance Lines and Excitation Transfer Between the $3P_{\frac{3}{2}}$ and $3P_{\frac{1}{2}}$ Levels", Phys. Rev. A **27**, 1851–1864 (1983).

[59] N. Lwin and D. McCartan, "Collision broadening of the potassium resonance lines by noble gases", Journal of Physics B: Atomic and Molecular Physics **11**, 3841 (1978).

[60] C. Carrington, D. Stacey, and J. Cooper, "Multipole relaxation and transfer rates in the impact approximation: application to the resonance interaction", Journal of Physics B: Atomic and Molecular Physics **6**, 417 (1973).

[61] E. Bernabeu and J. Alvarez, "Shift and broadening of hyperfine components of the first doublet of cesium perturbed by foreign gases", Physical Review A **22**, 2690 (1980).

[62] Z. Jabbour, J. Sagle, R. Namiotka, and J. Huennekens, "Measurement of the self-broadening rate coefficients of the cesium resonance lines", Journal of Quantitative Spectroscopy and Radiative Transfer **54**, 767 – 778 (1995).

[63] Z. J. Jabbour, Ph.D. thesis, Lehigh University, 1994.

[64] M. Aymar and O. Dulieu, "Calculations of transition and permanent dipole moments of heteronuclear alkali dimers NaK, NaRb and NaCs", Molecular Physics **105**, 1733 (2007).

[65] K. Richter, Private communication

Vita

Joshua grew up in rural upstate New York, where he met his wife, Holly. After high school, Joshua began his freshman year at SUNY Institute of Technology with hopes of majoring in Computer Engineering. He kept this goal as he changed schools to Penn State University at Wilkes-Barre. While at Penn State, and with the help of his physics professor, he decided to change his major to physics. Rather than finishing the degree at Penn State's Main Campus, he looked for a new academic home. In visiting a collegiate softball game at Lebanon Valley College, where his wife (then dating) was playing in a tournament, he found the place he was looking for. Joshua graduated Cum Laude with a B.S. in Physics in 2009 and decided to attend Lehigh to pursue a graduate degree in physics.

In August, before the start of the fall semester at Lehigh for Joshua and at De-Sales for Holly, they married. Holly pursued a graduate degree in Clinical Counseling and the Licensed Professional Counselor certification while Joshua received his M.S. in Physics in January of 2011. Professor John Huennekens guided Joshua through the contents of Jackson's Electricity and Magnetism text, atomic and molecular physics research, and the current dissertation work. Joshua and Holly are excited to have baby Maggie join them as they move to Hamilton, NY for Joshua's Post-doctoral Fellowship at Colgate University beginning in January 2015.